Third order Nonlinear properties in WSe_2 thin films

By

KM. SURBHI

PHYS1120170428

National Institute of Science Education and Research

A thesis submitted
to the Board of Studies in
School of Physical Sciences

In partial fulfillment of requirements
For the Degree of

**DOCTOR OF PHILOSOPHY**
of

HOMI BHABHA NATIONAL INSTITUTE

February, 2023

ii

Homi Bhabha National Institute

Recommendations of the Viva Voce Committee

As members of the Viva Voce Committee, we certify that we have read the dissertation prepared by **Km. Surbhi** entitled **"Third order Nonlinear properties in WSe_2 thin films"** and recommend that it may be accepted as fulfilling the thesis requirement for the award of Degree of Doctor of Philosophy.

Chairman - Dr. Bedangadas Mohanty	*Booodhanty*	Date: 09/06/2023
Guide / Convener - Dr. Ritwick Das	*Ritwick Das*	Date: 09/06/23
Co-guide - Dr. Pratap K.Sahoo	*Pratap*	Date: 09/06/2023
Member - Dr. Kartikeswar Senapati	*K.Senapati*	Date: 09/06/2023
Member - Dr. Ashok Mohapatra	*AMohapt*	Date: 09/06/2023
Examiner- Dr. Rajan Jha	*RJ*	Date: 09/6
External Examiner - Prof. Soma Venugopal Rao	*SVenugopalRao*	Date: 09 June 2023.
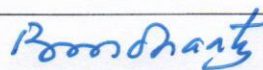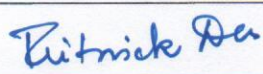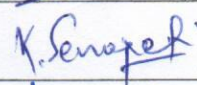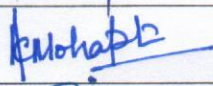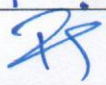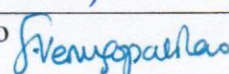
Final approval and acceptance of this thesis is contingent upon the candidate's submission of the final copies of the thesis to HBNI.

I hereby certify that I have read this thesis prepared under my direction and recommend that it may be accepted as fulfilling the thesis requirement.

Date : 08-06-2023
Place : NISER

Pratap   *Ritwick Das*

(Co-guide)   **(Guide)**

iv
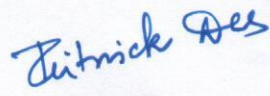
STATEMENT BY THE AUTHOR

This dissertation has been submitted in partial fulfillment of requirements for an advanced degree at Homi Bhabha National Institute (HBNI) and is deposited in the library to be made available to borrowers under rules of the HBNI.

Brief quotations from this dissertation are allowable without special permission, provided that accurate acknowledgement of source is made. Requests for permission for extended quotation from or reproduction of this manuscript in whole or in part may be granted by the Competent Authority of HBNI when in his or her judgment the proposed use of the material is in the interests of scholarship. In all other instances, however, permission must be obtained from the author.

(KM. SURBHI)

DECLARATION

I hereby declare that the investigation presented in the thesis has been carried out by me. The work is original and has not been submitted earlier as a whole or in part for a degree/diploma at this or any other Institution/University.

Surbhi

(KM. SURBHI)

List of Publications arising from the thesis

Journal

Published

1. Km. Surbhi, S. Bhakta, A. Kumari, U. P. Sahoo, P. K. Sahoo, and R. Das. "Impact of pauli-blocking effect on optical limiting properties of WSe_2 thin films." Opt. Mater. 129 (2022): 112479.

2. Km. Surbhi, S. Bhakta, P. K. Sahoo, and R. Das. "Impact of defects on the $\chi^{(3)}$ optical nonlinearity of sputtered WSe_2 thin films in the optical communication band." J. Appl. Phys. 132, no. 24 (2022): 243101.

Accepted

1. Km. Surbhi and Ritwick Das. "Nonlinear optical absorption properties of sputtered WSe_2 thin-films in the near-infrared spectral band ." accepted in IJPAP.

ix

Communicated

1. Km. Surbhi, U. P. Sahoo, P. K. Sahoo, and R. Das. "Impact of annealing on the optical limiting properties of WSe_2 thin films".

Manuscript under preparation

1. "Modification in third order nonlinear properties of WSe_2 thin films due to localized Surface plasmon resonance".

   (Not included in the thesis)

2. "Refractive index sensitivity of WSe_2 film based LSPR sensor".

3. "Tuning of bandgap and saturable absorption behaviour of WSe_2 thin films by Au ion implantation".

Conferences

1. Km. Surbhi, R Das, "Impact of Optical Fluence on Pauli Blocking Effect in WSe_2 Thin Film", Photonic Networks and Devices, 2022.

2. Km. Surbhi and Ritwick Das, "Free-carrier assisted optical nonlinearity in WSe_2 thin films near the optical communication band", Frontiers in Optics, 2022.

3. Km. Surbhi and Ritwick Das, "Third order nonlinearities associated with thermo-optical effects in WSe_2 thin film" COPaQ, 2022, IIT Roorkee.

(KM. SURBHI)

DEDICATED TO

To my parents Mr. Anoop Singh and Mrs. Surekha Devi

&

My brothers Shubham Kumar and Jatin Rana

ACKNOWLEDGEMENTS

Contents

Summary

The primary aim of the present thesis is to explore the possibilities of tailoring the linear and nonlinear optical properties of WSe_2 thin film based architectures. The thesis began with a concise description of underlying analytical and conceptual framework for explaining nonlinear optical response from materials. This also included discussions on factors and mechanisms that facilitate strengthening the NLO response from WSe_2 thin films. Further, the thesis presented discussions on the WSe_2 thin film deposition method and brief descriptions of the employed characterization techniques. In order to investigate the NLO properties of WSe_2 thin films, a detailed discussion on the in-house developed $Z-$scan experimental set-up using an ultrashort-pulsed fiber laser is presented. The chapters 3 and 4 of the thesis carries out detailed investigations on thickness-dependence and wavelength-dependence of NLO response in WSe_2 thin films. The discussions also include the impact of annealing the WSe_2 thin films on the NLO properties. The penultimate chapter presented the details of NLO investigations on heterostructures comprising Au nanoparticles embedded in sub-wavelength WSe_2 thin films.

List of Figures

List of Tables

List of Abbreviations

α Linear absorption coefficient

β Nonlinear absorption coefficient

$\chi^{(1)}$ Linear susceptibility

$\chi^{(2)}$ Second order susceptibility

$\chi^{(3)}$ Third order susceptibility

$\chi_{Im}^{(3)}$ Imaginary part of the complex third-order nonlinear susceptibility

$\chi_{R}^{(3)}$ Real part of the complex third-order nonlinear susceptibility

ΔT Normalized transmittance

$\Delta \phi_0$ Phase change due to nonlinear refraction

$\Delta \Psi_0$ Phase change due to nonlinear absorption

λ Excitation wavelength of laser beam

μ Amplitude of oscillating dipole moment

ν Laser frequency

ρ Charge density

$\vec{B}$ Magnetic flux density

$\vec{D}$ Electric displacement

$\vec{E}$ Electric field

$\vec{H}$ Magnetic field

$\vec{J}$ Current density

$\vec{P}$ Polarization

E_{gi} Energy gap between the ground state and intermediate state

I_0 On-axis peak laser intensity

$LiNbO_3$ Lithium Niobate

$MoSe_2$ Molybdenum selenide

n_2 Nonlinear refractive index

P^L Linear polarization

P^{NL} Nonlinear polarization

t_c Thermal lifetime

w_0 Beam-spot size

WSe_2 Tungsten diselenide

2Γ Full-width at half maximum of the TPA spectrum

2D Two dimensional

ATE Accumulated thermal effect

Au Gold

CA Closed-aperture

CB Conduction Band

c Speed of light in vacuum

DFG Difference frequency generation

DFT Density functional theory

DOS Density of states

D Dislocation density

EDS Energy dispersive X-ray spectroscopy

Eg Bandgap

ESA Excited state absorption

FCA Free carrier absorption

FESEM Field emission scanning electron microscope

FOM Figure of merit

FTL   Fourier-transform limited

GGA   Generalized gradient approximation

HWP   Halfwave plate

k   Propagation constant

LSPR   Localized surface plasmon resonance

L   Lens

MPA   Multiphoton absorption

NIR   Near Infrared

NLA   Nonlinear absorption

NLO   Nonlinear Optical

NLR   Nonlinear refraction

NPs   Nanoparticles

n   Linear refractive index

OA   Open-aperture

PAW   Projector-Augmented Wave

PBE   Perdew, Burke, and Ernzerhof

PBS   Polarising beam splitter

PVD   Physical vapour deposition

RF   Radio-frequency

RSA   Reverse saturable absorption

SA   Saturable absorption

SEM   Scanning electron microscope

Se   Selenium

SFG   Sum frequency generation

SHG   Second Harmonic Generation

S   Sample

TMD   Transition metal dichalcogenide

TPA   Two photon absorption

UV   Ultraviolet

VASP Vienna ab-initio simulation package

VB   Valence band

Vis   Visible

W   Tungsten

XRD   X-ray diffraction

Chapter 1

Introduction

The present thesis begins with the motivation of doing this research work which includes the significance of nonlinear optics and the advantages of using WSe_2. The second section offers the aim and objectives of the research effort. The third section gives an overview of nonlinear optics and a brief introduction to the concepts associated with nonlinear optical phenomena such as nonlinear refraction (NLR) and nonlinear absorption (NLA). In the fourth section of this chapter, we present the thesis outline.

1.1   Motivation

The motivation behind this thesis work is to explore the properties of transition metal dichalcogenide (TMD) material at sub-wavelength scale dimensions for ascertaining their capabilities in nonlinear optical (NLO) applications. For the present thesis work, we choose WSe_2 as a TMD material. A major emphasis of this work is aimed to facilitate the tailoring of linear and nonlinear properties of TMD based configuration for practical applications

such as optical switching, Q-switching, mode-locking, optical sensing and data-storage applications.

1.1.1 Significance of Nonlinear Optics

Nonlinear optics is the study of light-matter interaction in a regime where the optical properties of the material gets modified in presence of intense light [1]. Since, the discovery of the first nonlinear optical (NLO) phenomena which is known as second harmonic generation (SHG), the NLO effects are the topic of intense research due to the broad range of applications [1, 2]. Nonlinear optics has a great value and far-reaching impact on technology, as it is widely employed in so many areas including laser technology, image processing, information technology, light aspects of communication, storage, and optical computing [1, 2]. However, there are various new opportunities for nonlinear optics by virtue of rapid development of nanoscience and nanotechnology. The remarkable nonlinear optical properties exhibited by the sub-wavelength sized materials or alternately, the nanomaterials promotes the design and fabrication of miniaturized and monolithically integrated photonic chips and opto-electronic devices [3].

1.1.2 Advantages of using WSe_2

Over the past few years, a variety of studies on the nonlinear optical properties of the artificially-structured materials have been performed due to the potential of these materials in optical device applications. Moreover, the nanomaterials exhibiting strong NLO properties have the potential to enhance the operational efficiency in the areas of communications, biosensing and imaging. In addition, the ultrafast NLO response of such materials are very promising for applications in optical limiting, laser ablation, pulsed-laser deposition, optical data storage and optical information processing [2, 3]. The nanomaterials with large
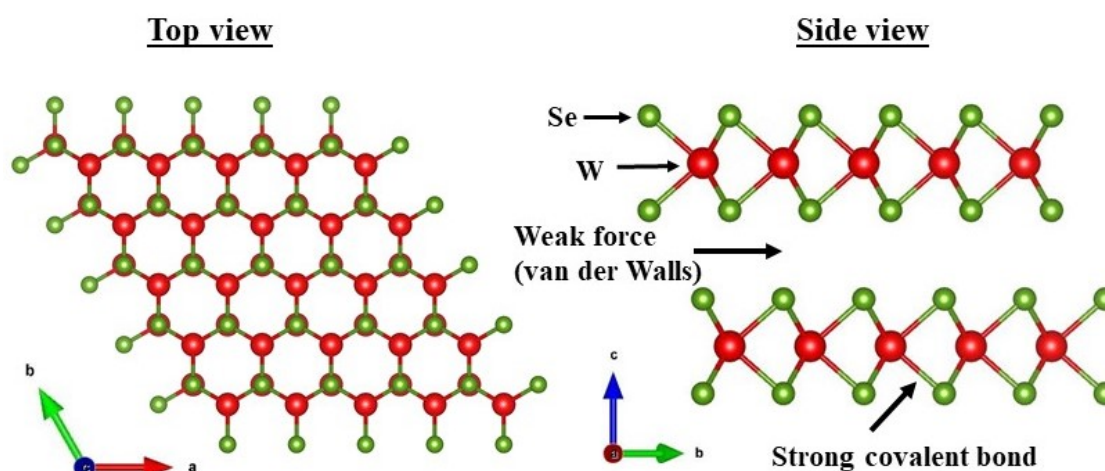
FIGURE 1.1: The schematic representation of the crystal structure of WSe_2. The top and side view are shown. The red and green balls represent W and Se atoms, respectively.

nonlinear optical responses can be utilized as optical limiters, photocatalysis, and contrasting agents in nonlinear optical microscopy [4]. It is worth mentioning that the search for new nanomaterials is one of the prominent attributes of modern science and technology. It has been shown through numerous researches that new nanomaterials can be employed to fabricate many devices such as new optical, magnetic, electrical, chemical, mechanical and biological devices. Consequently, a strong NLO response in nanomaterials provide a route to add functionality to the existing application. In this context, the employment of two dimensional (2D) transition metal dichalcogenides (TMDs) could be beneficial due to their unique and versatile properties such as high in-plane charge carrier mobility, high mechanical strength and weak coupling between the layers [5–9]. TMDs have been investigated for a broad range of applications which includes energy storage, gas sensing, biochemical/biological sensing, transistor development, piezoelectric and electronic devices and devising photo-switches [9–15].

TMDs comprise layered crystal structures, in which a layer of transition metal is encapsulated between two layers of chalcogen atoms as shown in Fig1.1. In the figure, both top

view and side view are represented. The compounds of TMD group can be symbolized by the formula of the type MX_2 (where, M is the transition metal as W, Mo and X is the chalcogenide as S, Se). The metal atom in the X-M-X layer is bonded to its six nearest neighbours (chalcogen atoms). However, the atoms in every layer are strongly bonded by covalent bond, while each layer is attached with the adjacent layer by weak (van der Walls) forces. The monolayer TMD has the direct bandgap. Meanwhile, the recent reports have revealed that the electronic bandstructure of TMDs is strongly dependent on the number of monolayers and undergoes a transition from direct to indirect as a function of increasing thickness [16, 17]. Such a possibility endows tremendous functional flexibility from an application point of view. From the perspective of NLO properties, the possibility of tailoring the bandstructure allows us to control the hyperpolarizability and consequently, one could utilize TMD based architectures to satisfy the constraints associated with an application [4]. By utilizing the idea, TMD-based architectures have been explored for a broad category of photonic applications such as optical switching [1, 2, 18], Q-switching and mode-locking [19–22], data storage [23], optical limiting [24, 25]. Conventionally, a single monolayer TMD or a few monolayer TMD has thickness much smaller than the wavelength of light which is used for probing the optical properties. Therefore, it is expected that the NLO phase-shifts and absorption by a few monolayered TMD-based configuration are relatively weaker. From a practical perspective, TMD thin-films with thicknesses ranging between a hundred nanometer to a few micrometers would be more suitable for photonic applications. The dependence of third-order ($\chi^{(3)}$) NLO properties of a few TMD species have been explored with respect to variation in structural parameters and excitation source [26–32]. However, a comprehensive investigation aimed towards exploring the impact of defects in TMD-based thin-film architectures on $\chi^{(3)}$-associated manifestations are yet to be explored.

1.2 Aim and Objectives

The aim of carrying out the present research is to investigate the third order nonlinearity in WSe_2 thin films and to take up an analysis of the impact by various factors including laser parameters (wavelength, repetition rate, intensity) and material properties (thickness, defects, heterostructures) on the third order NLO properties in RF-sputtered WSe_2 thin films.

1.3 Optical nonlinearities

In this section, we present an introduction to nonlinear optics (NLO) and third order optical nonlinearities as well as a broad variety of underlying phenomenon that affect the NLO response of materials.

We will begin with very basic of linear optics i.e. Maxwell's equations [33]

$$\nabla.\vec{E} = \frac{\rho}{\epsilon_0} \qquad (Gauss's\ law) \qquad (1a)$$

$$\nabla.\vec{B} = 0 \qquad (Gauss's\ law\ for\ magnetism) \qquad (1b)$$

$$\nabla \times \vec{E} = -\frac{\partial \vec{B}}{\partial t} \qquad (Faraday's\ law) \qquad (1c)$$

$$\nabla \times \vec{H} = \vec{J} + \frac{\partial \vec{D}}{\partial t} \qquad (Ampere's\ law) \qquad (1d)$$

where $\vec{E}$ and $\vec{H}$, ρ, $\vec{D}$, $\vec{J}$, $\vec{B}$ are the electric and magnetic field, charge density, electric displacement, current density, magnetic flux density, respectively. When a dielectric material is exposed to an electric field, its atoms respond by forming electric dipoles as shown in Fig.1.2. At low input intensity of an optical system, the properties of the material are not affected by the light beam and hence, the optical response changes linearly with the applied electric field. In order to understand this, let us consider the polarization $\vec{P}$ of the material system is determined by the electric field ($\vec{E}$). The induced polarization in linear
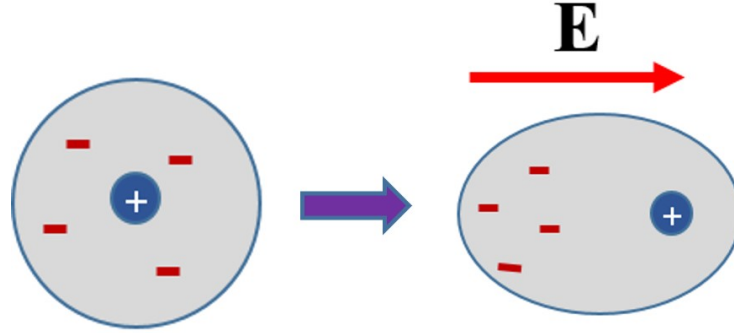
FIGURE 1.2: Mechanism of polarization.

optics is linearly related to the electric field through the relation [1]

$$\vec{P} = \epsilon_0 \chi^{(1)} \vec{E} \tag{1.1}$$

where ϵ_0 is the permittivity of free space, $\chi^{(1)}$ is the linear susceptibility and it is of the order of unity. The real part of $\chi^{(1)}$ is associated with the linear refractive index (n) whereas the imaginary part of $\chi^{(1)}$ is related to the linear absorption (α) [1].

The wave equation, in the case of linear optics could be derived from the Eqs. 1(c) and 1(d) and it has the form

$$\nabla^2 \vec{E} - \mu_0 \frac{\partial^2 \vec{D}}{\partial t^2} = 0 \tag{1.2}$$

whereas $\vec{D}$ and $\vec{E}$ are related with the expression, $\vec{D} = \epsilon_0 \vec{E} + \vec{P}$. Now, the wave equation for the linear optical media could be written as

$$\nabla^2 \vec{E} - \frac{1}{c^2} \frac{\partial^2 \vec{E}}{\partial t^2} = \frac{1}{\epsilon_0 c^2} \frac{\partial^2 \vec{P}}{\partial t^2} \tag{1.3}$$

When $\vec{P}$ and $\vec{E}$ bear a linear relationship, Eq. (1.3) is a homogeneous partial differential equation and could be solved in a variety of situations associated with periodic media, directional couplers, metallo-dielectric heterostructures and many more.

1.3.1 Introduction to Nonlinear optics

Nonlinear optics is the study of light-material interaction, where, the modification in the optical properties of the material with the presence of light is studied. Basically, the nonlinear effects are due to the dependency of material properties on the electric field associated with the light beam. However, the incident light beam should have a high enough intensity to modify the material polarization $\vec{P}$ significantly. In that case, the polarization is expressed through a nonlinear dependence on the electric field of an electromagnetic wave. To modify the optical characteristics of the material, a few milliwatts of moderately focused laser light is sufficient. This modification in the material properties results in the nonlinear optical processes such as harmonic generation, self-focusing, solitons and NLA etc [1]. Therefore, the polarization $\vec{P}$ (in scalar form) of the material system does not change linearly with the electric field ($\vec{E}$) and also, includes contributions from higher powers of $\vec{E}$ (in scalar form) as described below [1],

$$P = \epsilon_0 \chi^{(1)} E + \underbrace{\epsilon_0 \chi^{(2)} E^2 + \epsilon_0 \chi^{(3)} E^3 + ...} \tag{1.4}$$

where $\chi^{(2)}$ is the second order susceptibility and of the order of $\approx 10^{-12} m/V$, $\chi^{(3)}$ is the third order susceptibility and of the order of $\approx 10^{-24} m^2/V^2$.

Therefore, the polarization could be written as

$$P = P^{(L)} + P^{(NL)} \tag{1.5}$$

In this case, the wave equation (in terms of scalar fields) in nonlinear optical media is written as

$$\nabla^2 \vec{E} - \frac{1}{\epsilon_0 c^2} \frac{\partial^2 \vec{D}^{(L)}}{\partial t^2} = \frac{1}{\epsilon_0 c^2} \frac{\partial^2 \vec{P}^{(NL)}}{\partial t^2} \tag{1.6}$$

where, $D^{(L)}$ is expressed as $D^{(L)} = \epsilon_0 E + P^{(L)}$.

$$E = \frac{1}{2}[E_0 e^{i(kz-\omega t)} + c.c]$$
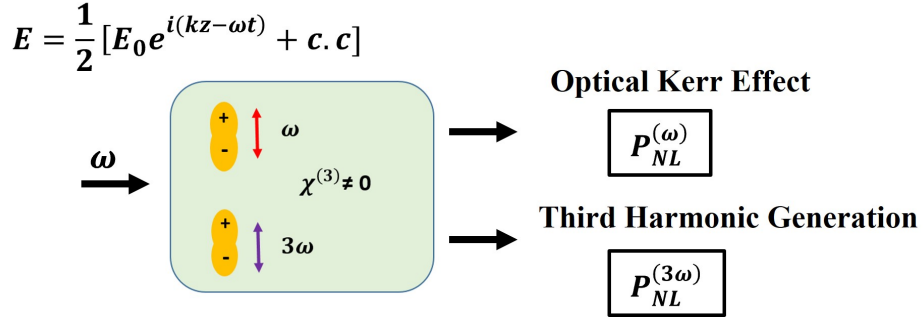
FIGURE 1.3: Schematic representation of optical Kerr effect and third harmonic generation.

1.3.2   Third-order nonlinear optical properties

The (scalar) nonlinear polarization is expressed as

$$P^{(NL)} = \epsilon_0 \chi^{(2)} E^2 + \epsilon_0 \chi^{(3)} E^3 + ... \tag{1.7}$$

which could also be expressed as

$$P^{(NL)} = P^{(2)} + P^{(3)} + ... \tag{1.8}$$

The second-order susceptibility $\chi^{(2)}$ gives rise to phenomena like second-harmonic gener-ation (SHG), sum frequency generation (SFG), optical parametric processes, and difference frequency generation (DFG), while the third-order susceptibility $\chi^{(3)}$ cover a wide field of NLO and is the cause of various phenomena such as, the third harmonic generation (THG), NLA, intensity-dependent refractive index, four-wave mixing etc [1].   For our studies, third-order susceptibility and the phenomena that lead to NLA and NLR are primarily of interest. Although, the magnitude of linear susceptibility $\chi^{(1)}$ is much greater than the magnitude of nonlinear susceptibilities $\chi^{(2)}$ and $\chi^{(3)}$, their responses could only be seen at high input intensities or at long laser-matter interaction length [1].

As we are studying the third-order nonlinear optical properties, we will try to understand

third order polarization that is given as

$$P^{(3)} = \epsilon_0 \chi^{(3)} E^3 \tag{1.9}$$

In case of an incident plane wave at frequency ω ($E = \frac{1}{2}[E_0 e^{i(kz-\omega t)} + c.c.]$), the atoms of the dielectric material for which $\chi^{(3)}$ is nonzero, will vibrate with two frequencies as shown in Fig.1.3 and the expression for $P^{(3)}$ could be expressed as [1]

$$P^{(3)} = \frac{\epsilon_0 \chi^{(3)}}{8} [3E_0|E_0|^2 e^{i(kz-\omega t)} + E_0^3 e^{3i(kz-\omega t)} + c.c] \tag{1.10}$$

The first term describes the nonlinear optical response at the fundamental frequency ω and gives rise to the optical Kerr effect, NLR and NLA [1], while, the second term describes a response at frequency 3ω, which is created by the field at frequency ω. This term signifies that the frequency mixing caused by the interactions of three fields results in the formation of the fourth field and leads to the process of third harmonic generation [1]. In this section, the third-order nonlinear optical manifestations such as the NLA and intensity-dependent refractive index (n_2) associated with $\chi^{(3)}$ are analyzed and discussed. In a general description, the third-order nonlinear susceptibility $\chi^{(3)}$ is a complex quantity and it is tensot of rank 4. In the scalar form, $\chi^{(3)}$ could be expressed as [34]

$$\chi^{(3)} = \chi_R^{(3)} + i\chi_{Im}^{(3)} \tag{1.11}$$

where $\chi_R^{(3)}$ and $\chi_{Im}^{(3)}$ are the real and imaginary components of the complex third-order nonlinear optical susceptibility ($\chi^{(3)}$) which is directly related to n_2 and nonlinear absorption coefficient (β) respectively.

1.3.3 Nonlinear Absorption

In the linear absorption process, a single photon is absorbed by the material to reach in a higher energy state. Meanwhile, NLA entails the absorption of two or more photons

simultaneously to reach the excited energy state [1]. In order to achieve NLA phenomena in a medium, sufficiently intense light needs to be incident. The intensity-dependent NLA could be expressed as

$$\alpha(I) = \alpha + \beta I \qquad (1.12)$$

In the above equation, $\alpha(I)$ includes both linear and nonlinear terms, where, α is the linear absorption coefficient, β is NLA coefficient and I is the laser beam intensity within the medium. The NLA phenomena is associated with the change in the pump beam amplitude during propagation through a medium having a non-zero value for the imaginary component of $\chi^{(3)}$ [35]. It is an intensity-dependent process and reaches its maximum when the medium is at the laser's focal point. The NLA mechanism may result from a number of processes, including saturable absorption (SA), reverse saturable absorption (RSA), multiphoton absorption (MPA), free carrier absorption (FCA) and excited state absorption (ESA) [1, 36, 37]. The aforesaid NLA processes are influenced by the pump intensities, laser frequency (ν), and laser pulse duration. In addition, the inherent material properties are extremely crucial towards the NLA characteristics [37].

Saturable absorption: A quantum mechanical picture

In order to understand the saturable absorption behaviour in WSe_2, we used a schematic diagram as shown in Fig.1.4. In the figure, material bandgap is represented by E_g. When the incoming photon energy ($h\nu$) has an energy greater than E_g then the linear absorption is dominant. In that case, the electrons reside near the bottom of the conduction band (CB) of the medium (Fig. 1.4(b)). However, at very high laser intensities, the CB exhibits saturation in terms of unoccupied states. Consequently, the absorption tends to drop at high laser intensities which is also termed as saturable absorption (see Fi. 1.4(c)).
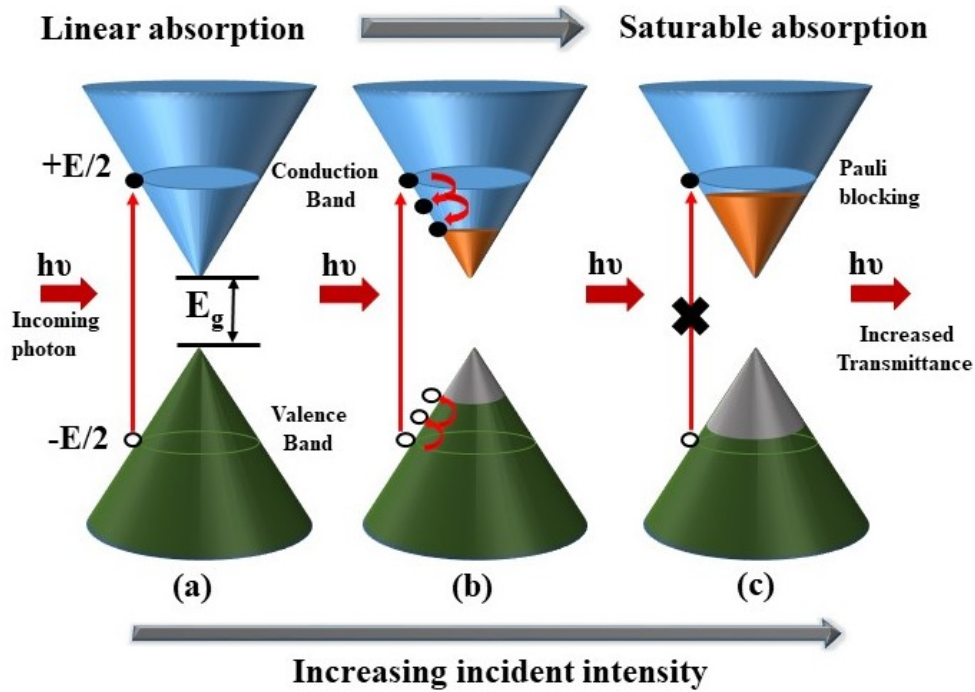
FIGURE 1.4: A schematic to show saturable absorption mechanism of WSe_2 thin films for demonstrating the Pauli-blocking principle. (a) shows the inter-band transition process. (b) shows the process of thermalization of hot electrons and obtaining a thermal equilibrium. (c) shows the filled states near the band edge which restricts the absorption of light.

Reverse saturable absorption

In the case of reverse saturable absorption (RSA), the optical transmission in the medium reduce at high laser intensities which results in a positive value of β. The reverse saturable absorption (RSA) includes various processes such as excited state absorption (ESA), two photon absorption (TPA), and multiphoton absorption (MPA). The two-photon absorption is a process of the simultaneous absorption of two photons for excitation from a ground state to the excited state. An allowed TPA transition in a semiconducting thin film is the one for which the excitation energy of an incident laser beam should be less than the energy bandgap (E_g) and greater than $E_g/2$ for the films [38]. The TPA process would cease to exist for excitation photon energy less than $E_g/2$. In an extreme case of TPA process, the

two-photon transition probability reduces as a result of non-availability of states in the CB which is alternately termed as *Pauli-blocking effect* [39, 40]. This essentially happens at very high laser intensities. The ESA is the process in which, an atom makes the transition from one lower-energy excited state to a higher-energy excited state by absorbing a photon. It is only feasible to absorb an excited state when an electron has previously been stimulated from its ground state to a lower excited state. Therefore, it could alternately be termed as resonant TPA.

1.3.4   Intensity dependent nonlinear refractive index

The spatial variation in the refractive index of the material brought on by the presence of an intense laser beam is referred to as the nonlinear refractive index (n_2). [1, 35]. The high-intensity refractive index change in semiconductors is caused by a variety of physical processes such as electronic contribution, thermal nonlinearity and photorefractive effects [1, 33, 36, 41, 42]. The electronic contribution to the nonlinear refractive index change is related to optical Kerr effect. In order to understand the idea, we refer to the first term in Eq. 1.10 which states that

$$P^{(3)} = \frac{\epsilon_0 \chi^{(3)}}{8} [3E_0 |E_0|^2 e^{i(kz - \omega t)} + c.c]$$ (1.13)

which could be simplified to obtain the total refractive index. This is given by,

$$n(I) = n + n_2 I$$ (1.14)

where, n is the linear refractive index and n_2 is nonlinear refraction coefficient. n_2 contains contribution from a large number of material properties which include electronic, thermal (phonon-mediated), elastic as well as acoustic properties. It is important to note that the nonlinear refractive index is also affected by overall medium absorption which includes the
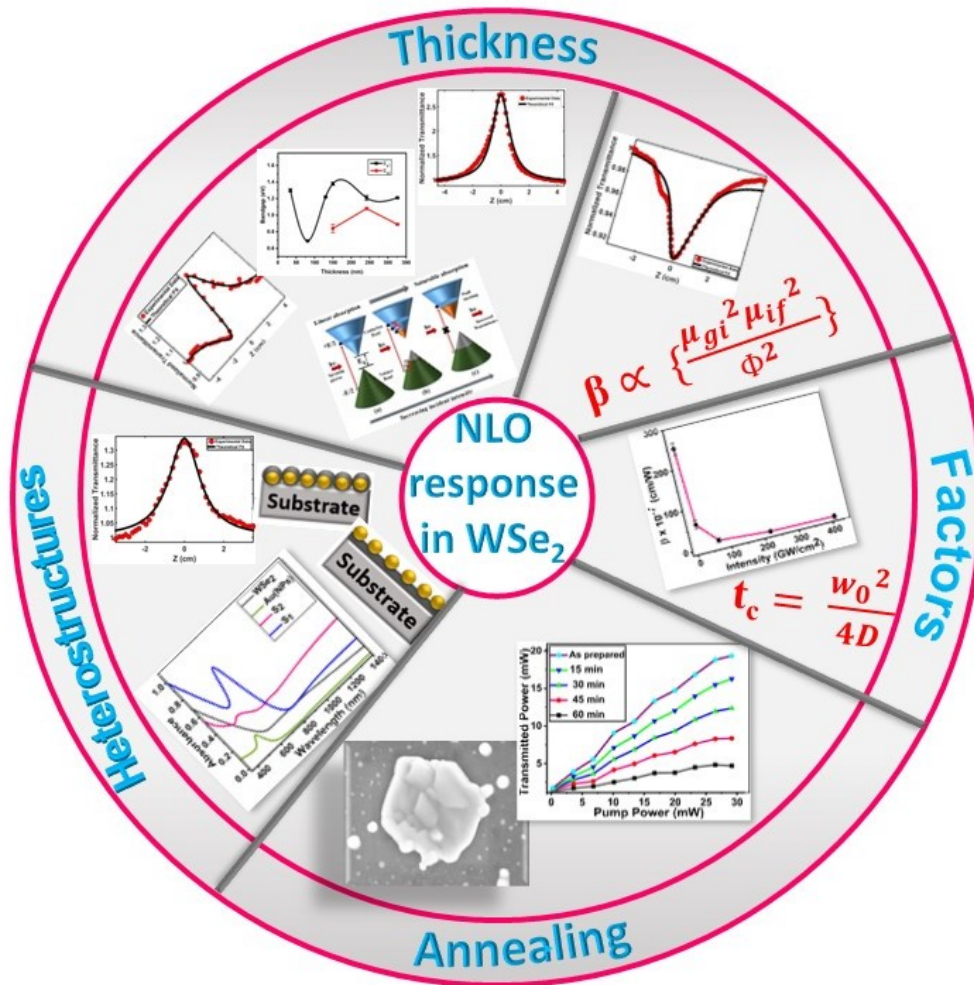
FIGURE 1.5: Graphical representation of the outline of the thesis.

nonlinear absorption mentioned above. In general, the absorption leads to the redistribution of charges and matter density which affect the diffractive as well as dispersive features of the medium through the NLR process. In the case of semiconductors, the impact of photorefractive effects is significant and leads to substantial changes in measured nonlinear refractive index.

1.4   Thesis Outline

In order to carry out the research work, we divided the approach into three different sections- thin-film deposition, characterization and description of theoretical background, investigation of NLO response of the WSe_2 thin films. The graphical representation of the outline of the thesis is shown in Fig.1.5. In the first chapter, we present a brief description of the basic concepts of optical nonlinearity and the factors and mechanisms that determine the NLO response of TMD films [1, 42–44]. The second chapter describes the WSe_2 thin film deposition process and a description of employed characterization techniques [34, 43]. In the third chapter, we have investigated the NLO properties in WSe_2 thin films using the in-house developed experimental set-up pumped by a ultrashort-pulse fiber laser. The thickness dependence of NLO response in WSe_2 films is performed in different spectral bands [45, 46]. We present a detailed analysis and discuss the factors which affect optical nonlinearity [47, 48]. The fourth chapter of the thesis focus on the impact of annealing on the NLO properties of WSe_2 thin films. This work was extended by creating heterostructures comprising the Au nanoparticles embedded in sub-wavelength WSe_2 films, which is the fifth chapter. In the sixth chapter, we present a summary of work and future plans.

Bibliography

[1]   Robert W Boyd. *Nonlinear Optics*. Academic press, 2020.

[2]   Chunfei Li. *Nonlinear Optics: principles and applications*. Springer, 2016.

[3]   Xiaofeng Liu, Qiangbing Guo, and Jianrong Qiu. "Emerging low-dimensional materials for nonlinear optics and ultrafast photonics". *Advanced Materials* 29.14 (2017), p. 1605886.

[4] Anton Autere et al. "Nonlinear Optics: Nonlinear Optics with 2D Layered Materials (Adv. Mater. 24/2018)". *Adv. Mater.* 30.24 (2018), p. 1870172.

[5] Jl A Wilson and AD Yoffe. "The transition metal dichalcogenides discussion and interpretation of the observed optical, electrical and structural properties". *Advances in Physics* 18.73 (1969), pp. 193–335.

[6] Ruben Mas-Balleste et al. "2D materials: to graphene and beyond". *Nanoscale* 3.1 (2011), pp. 20–30.

[7] Qing Hua Wang et al. "Electronics and optoelectronics of two-dimensional transition metal dichalcogenides". *Nature nanotechnology* 7.11 (2012), pp. 699–712.

[8] Sheneve Z Butler et al. "Progress, challenges, and opportunities in two-dimensional materials beyond graphene". *ACS nano* 7.4 (2013), pp. 2898–2926.

[9] Dongzhi Chi, KE Johnson Goh, and Andrew TS Wee. *2D Semiconductor Materials and Devices*. Elsevier, 2019.

[10] Yong-Ping Gao et al. "Two-dimensional transition metal diseleniums for energy storage application: a review of recent developments". *CrystEngComm* 19.3 (2017), pp. 404–418.

[11] Hai Li et al. "Fabrication of single-and multilayer MoS_2 film-based field-effect transistors for sensing NO at room temperature". *Small* 8.1 (2012), pp. 63–67.

[12] Huawen Hu et al. "Recent advances in two-dimensional transition metal dichalcogenides for biological sensing". *Biosens. Bioelectron.* 142 (2019), p. 111573.

[13] Branimir Radisavljevic et al. "Single-layer MoS 2 transistors". *Nature nanotechnology* 6.3 (2011), pp. 147–150.

[14] Jianhui Yang et al. "Coexistence of piezoelectricity and magnetism in two-dimensional vanadium dichalcogenides". *Phys. Chem. Chem. Phys.* 21.1 (2019), pp. 132–136.

[15] Zongyou Yin et al. "Single-layer MoS_2 phototransistors". *ACS Nano* 6.1 (2012), pp. 74–80.

[16] D Voß et al. "Atomic and electronic structure of WSe_2 from ab initio theory: Bulk crystal and thin film systems". *Phys. Rev. B* 60.20 (1999), p. 14311.

[17] Won Seok Yun et al. "Thickness and strain effects on electronic structures of transition metal dichalcogenides: 2H-MX$_2$ semiconductors (M= Mo, W; X= S, Se, Te)". *Physical Review B* 85.3 (2012), p. 033305.

[18] Linnan Jia et al. "Large third-order optical kerr nonlinearity in nanometer-thick PdSe_2 2D dichalcogenide films: implications for nonlinear photonic devices". *ACS Appl. Nano Mater.* 3.7 (2020), pp. 6876–6883.

[19] Bohua Chen et al. "Q-switched fiber laser based on transition metal dichalcogenides MoS$_2$, MoSe$_2$, WS$_2$ and WSe$_2$". *Optics express* 23.20 (2015), pp. 26723–26737.

[20] Dong Mao et al. "WS$_2$ mode-locked ultrafast fiber laser". *Sci. Rep.* 5.1 (2015), pp. 1–7.

[21] Wenjun Liu et al. "Tungsten diselenide for mode-locked erbium-doped fiber lasers with short pulse duration". *Nanotechnology* 29.17 (2018), p. 174002.

[22] Yabin Shao et al. "Wavelength-dependent nonlinear absorption and ultrafast dynamics process of WS$_2$". *OSA Continuum* 2.9 (2019), pp. 2755–2763.

[23] Feichi Zhou et al. "2D materials based optoelectronic memory: convergence of electronic memory and optical sensor". *Research* 2019 (2019).

[24] Kian Ping Loh et al. "Templated deposition of MoS$_2$ nanotubules using single source precursor and studies of their optical limiting properties". *The Journal of Physical Chemistry B* 110.3 (2006), pp. 1235–1239.

[25] Charles W Spangler. "Recent development in the design of organic materials for optical power limiting". *Journal of Materials Chemistry* 9.9 (1999), pp. 2013–2020.

[26] Kangpeng Wang et al. "Broadband ultrafast nonlinear absorption and nonlinear refraction of layered molybdenum dichalcogenide semiconductors". *Nanoscale* 6.18 (2014), pp. 10530–10535.

[27] Kai-Ge Zhou et al. "Size-dependent nonlinear optical properties of atomically thin transition metal dichalcogenide nanosheets". *Small* 11.6 (2015), pp. 694–701.

[28] Saifeng Zhang et al. "Direct observation of degenerate two-photon absorption and its saturation in WS$_2$ and MoS$_2$ monolayer and few-layer films". *ACS Nano* 9.7 (2015), pp. 7142–7150.

[29] Ningning Dong et al. "Dispersion of nonlinear refractive index in layered WS_2 and WSe_2 semiconductor films induced by two-photon absorption". *Opt. Lett.* 41.17 (2016), pp. 3936–3939.

[30] S Bikorimana et al. "Nonlinear optical responses in two-dimensional transition metal dichalcogenide multilayer: WS_2, WSe_2, MoS_2 and $Mo_{0.5}W_{0.5}S_2$". *Opt. Express* 24.18 (2016), pp. 20685–20695.

[31] Gaozhong Wang et al. "Broadband saturable absorption and exciton-exciton annihilation in $MoSe_2$ composite thin films". *Opt. Mater. Express* 9.2 (2019), pp. 483–496.

[32] Mengmeng Yan et al. "Third order nonlinear optical property of WSe_2 nanofilm at 800 nm". *Opt. Mater.* 107 (2020), p. 110040.

[33] eg PA Franken et al. "Generation of optical harmonics". *Physical Review Letters* 7.4 (1961), p. 118.

[34] Mansoor Sheik-Bahae, Ali A Said, and Eric W Van Stryland. "High-sensitivity, single-beam n_2 measurements". *Optics letters* 14.17 (1989), pp. 955–957.

[35] Mansoor Sheik-Bahae and Eric W Van Stryland. *Optical nonlinearities in the transparency region of bulk semiconductors*. Tech. rep. UNIVERSITY OF CENTRAL FLORIDA ORLANDO, 1999.

[36] R Sutherland. "Handbook of nonlinear optics Marcel Dekker Inc". *New York* (1996).

[37] Mariacristina Rumi and Joseph W Perry. "Two-photon absorption: an overview of measurements and principles". *Advances in Optics and Photonics* 2.4 (2010), pp. 451–518.

[38] Eric W Van Stryland et al. "Two photon absorption, nonlinear refraction, and optical limiting in semiconductors". *Optical Engineering* 24.4 (1985), p. 244613.

[39] Jia Guo et al. "Two-dimensional tellurium–polymer membrane for ultrafast photonics". *Nanoscale* 11.13 (2019), pp. 6235–6242.

[40] Nannan Xu et al. "Palladium diselenide as a direct absorption saturable absorber for ultrafast mode-locked operations: from all anomalous dispersion to all normal dispersion". *Nanophotonics* 9.14 (2020), pp. 4295–4306.

[41]   Paul N Butcher and David Cotter. *The elements of nonlinear optics*. Cambridge university press, 1990.

[42]   Demetrios N Christodoulides et al. "Nonlinear refraction and absorption: mechanisms and magnitudes". *Advances in Optics and Photonics* 2.1 (2010), pp. 60–200.

[43]   Mansoor Sheik-Bahae et al. "Sensitive measurement of optical nonlinearities using a single beam". *IEEE journal of quantum electronics* 26.4 (1990), pp. 760–769.

[44]   Mansoor Sheik-Bahae and Michael P Hasselbeck. "Third-order optical nonlinearities". *Handbook of Optics* 4 (2000), pp. 16–1.

[45]   Km. Surbhi et al. "Impact of pauli-blocking effect on optical limiting properties of WSe$_2$ thin films". *Optical Materials* 129 (2022), p. 112479. ISSN: 0925-3467.

[46]   Km Surbhi et al. "Impact of defects on the $\chi^{(3)}$ optical nonlinearity of sputtered WSe_2 thin films in the optical communication band". *Journal of Applied Physics* 132.24 (2022), p. 243101.

[47]   Km Surbhi and Ritwick Das. "Impact of Optical Fluence on Pauli Blocking Effect in WSe_2 Thin Film". In: *Photonic Networks and Devices*. Optica Publishing Group. 2022, JW3A–39.

[48]   Km Surbhi and Ritwick Das. "Free-carrier assisted optical nonlinearity in WSe_2 thin films near the optical communication band". In: *Laser Science*. Optica Publishing Group. 2022, JW4A–88.

Chapter 2

WSe_2 thin film preparation and characterization techniques

This chapter contains an overview of the experimental techniques and analytical framework employed in this thesis. The WSe_2 thin films studied in this work were deposited using a radio-frequency (RF) magnetron sputtering system. The characterization of RF-sputtered WSe_2 thin film was being carried out using a field-emission scanning electron microscope (FESEM), X-ray diffractometer (XRD), and Raman spectroscopy. The linear absorption spectrum of the WSe_2 thin film was carried out using a absorption spectrometer containing a ultra-violet (UV) and visible light source. The nonlinear optical measurements of the WSe_2 thin films were performed using the single-beam Z-scan technique. The detailed explanation about the Z-scan technique is given in section 2.6.

2.1   Radio Frequency (RF)-sputtering Method

Sputtering is a physical vapour deposition (PVD) process in which the bombardment of energetic particles causes the atoms to be expelled from a solid target material [1, 2]. The schematic of sputtering process is given in fig.2.1. The Ar ions, that are formed by the interaction of Ar gas with the free electrons, are typically utilised for bombardment. This process involves the acceleration of positively charged ions from the plasma of gas species towards the target, a negatively charged electrode. When the incident ions collide with the target, they impart their momentum to the target atoms, causing atoms to be ejected from the target material. A magnetic field is typically applied close to the target in a magnetron sputtering technique to trap the ions, increasing the effectiveness of the initial ionisation process. The expelled atoms condense on the surfaces of the substrates.
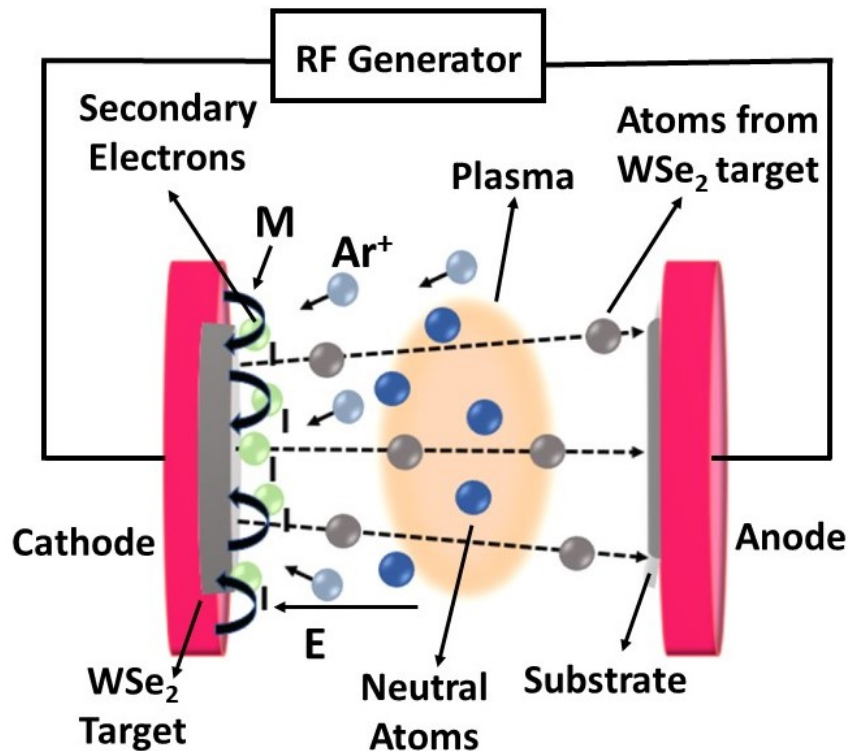
FIGURE 2.1: Schematic of RF magnetron sputtering

For this thesis, the WSe_2 thin films were prepared using a RF magnetron sputtering system with a WSe_2 (99.9% pure) target in an argon environment at room temperature. WSe_2 thin films with a desired thickness were sputtered onto a $1\ cm \times 1\ cm\ SiO_2/Si$ and glass substrate. Prior to the deposition, the chamber was evacuated by a turbomolecular pump to a vacuum of 3.1×10^{-6} mbar. Throughout the deposition process, the Ar gas concentration was maintained at 15 $sccm$, and the power was fixed at 60 W. The depositions were performed at a pressure of 1×10^{-2} mbar.

2.2 Field Emission Scanning Microscopy (FESEM)

The scanning electron microscope (SEM) is a tool that is extensively used to study the surface morphology of microstructures [3–8]. In a typical SEM, a powerful electron beam interacts with the material and transfers its kinetic energy to the electrons already present in the sample, resulting in secondary electron emission due to inelastic scattering and back-scattered electron emission due to elastic scattering with electromagnetic radiation. The emitted electrons are captured by the detectors that are part of the system, and then their intensity for each pixel is converted on a computer to produce the morphology of the sample. In a conventional SEM, a small energy dispersion electron gun is used to provide a steady electron beam with a high current and a tiny spot size. The filament of a thermionic electron gun is heated electrically, which causes the filament to emit electrons. These electron sources have a number of drawbacks, including the need for high temperatures, brightness, and limited spatial resolution. However, in a typical field emission electron gun, an electrostatic field is applied to induce electron emission. Field emission electron guns are frequently employed in modern scanning electron microscopes, which provide improved spatial resolution with strong contrast, reduced electrostatic distortion, small spot diameter,
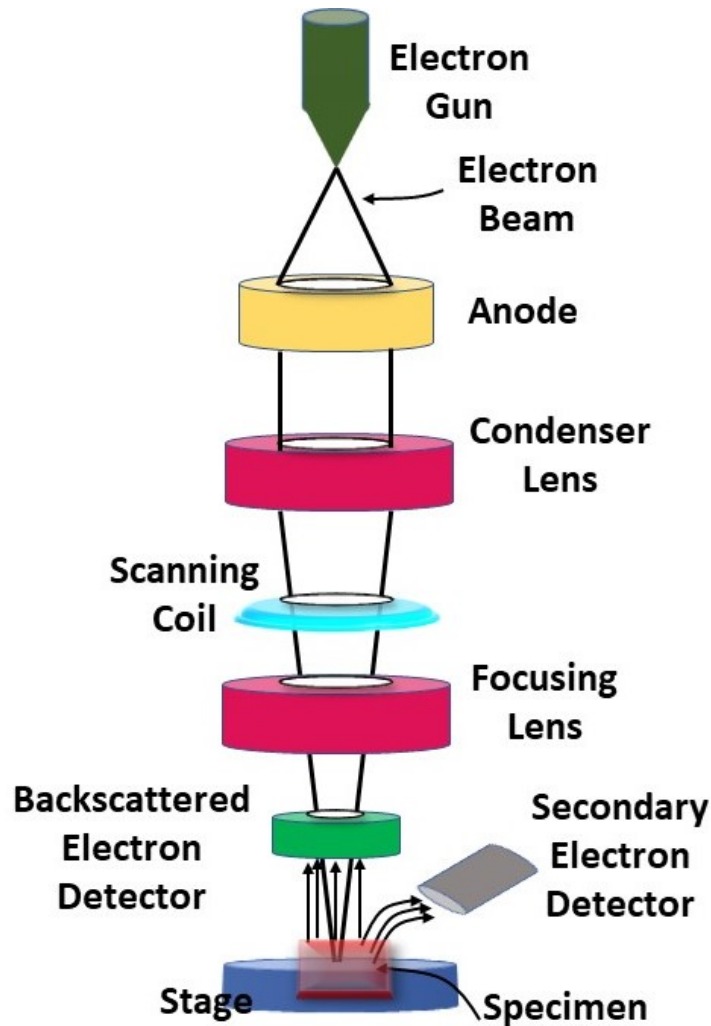
FIGURE 2.2: A schematic of typical field emission scanning electron microscope (FESEM).

and coherent emission. In the current thesis, the morphology and interface structure of WSe_2 thin films were examined using a (Carl-Zeiss, Sigma model) field emission scanning electron microscope (FESEM). Fig.2.2 depicts the schematic ray diagram of a typical FESEM system, where a field emission electron gun is employed as an electron source. The anode receives an extraction voltage to accelerate the electrons. Although the maximum extraction voltage for this FESEM model is 30 kV, all of the images provided in this thesis were taken at a 5 kV extracting voltage. The gun chamber was always kept at a base pressure

of about 3×10^{-9} mbar, while the column chamber was kept at a vacuum $\approx 2 \times 10^{-5}$ mbar for imaging. In the Figure, the focusing lens is used to align the beam on the specimen, while the electromagnetic lens designated as the condenser lens is utilized to convert the divergent beam into a converging/parallel beam.

2.3   X-ray Diffraction (XRD)

X-ray diffraction (XRD) utilizes the wave/particle duality of X-rays to collect information about the crystalline structure of the materials [9–11]. This approach is mostly used to identify the crystallographic phases of elements or composite materials based on their diffraction pattern. XRD is an effective analytical tool to determine grain size, lattice constants, the composition of solid solution, and degree of crystallinity in a mixture of crystalline and amorphous materials. This method is frequently used to analyze the crystal structures, crystallite sizes, atomic spacings, lattice parameters, stress analysis, and quantitative phase analysis.

XRD is based on constructive interference of monochromatic X-rays that diffracted from crystallographic planes of the sample. A cathode ray tube produces the X-rays, which are then filtered to generate monochromatic radiation, focused by collimation, and pointed towards the sample. The incident X-rays interact with the sample and constructive interference (and a diffracted ray) produces only when the conditions satisfy Bragg's Law [9]

$$n\lambda = 2d \sin\theta \tag{2.1}$$

as shown in Fig.2.3., where n is any integer, λ is the wavelength of the beam, d is the spacing between diffracting planes, and θ is the incident angle. Then, these diffracted X-rays are detected, examined, and quantified. All prospective diffraction directions of
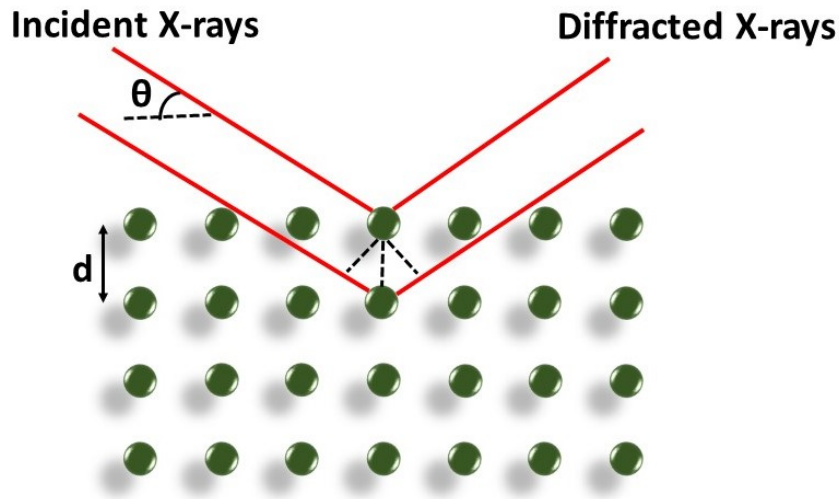
FIGURE 2.3: Typical ray-diagram of X-ray diffraction from a periodic chain of atoms.

the lattice ought to be obtained by scanning the sample over a range of 2θ angles. Since each material has a specific set of d-spacings, the conversion of the diffraction peaks to d-spacings enables the recognition of the material. XRD can measure the diffraction of the beam from different sections of the compound. In this thesis, the XRD patterns of the WSe_2 thin films were captured using a Rigaku Smartlab X-ray diffractometer with Cu Kα (λ = 1.5418 Å).

2.4 Raman Spectroscopy

Raman spectroscopy is the technique often used to identify vibrational modes of the molecules. It is named after the Indian physicist C. V. Raman. Raman spectroscopy relies upon inelastic scattering of photons, which is sensitive to the vibrational and rotational modes of atomic and molecule species [12–15]. A source of monochromatic light, usually from a laser in the ultraviolet, visible or near infrared range is used. The interaction of laser light with the phonons, molecular vibrations or other excitations in the system will be either in the ground vibrational/rotational states or in the excited vibrational/rotational
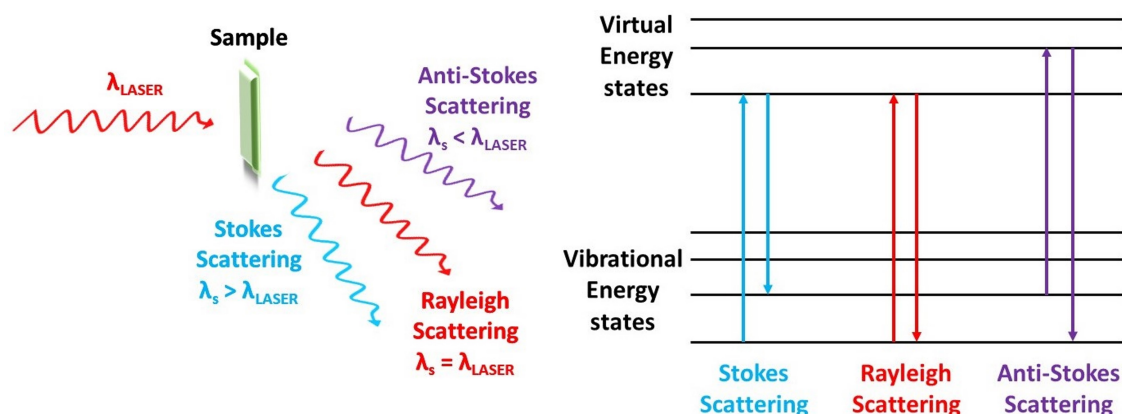
FIGURE 2.4: Principle of Raman scattering: Types of scattering processes that can take place when light interacts with the material. The energy level diagram of Raman scattering and Rayleigh scattering process. λ_s : scattering wavelength.

states depending on the energy of incident radiation. When the molecules are excited, a change in polarizability takes place, creating a dipole moment that causes inelastic scattering of photons (Stokes or anti-Stokes lines). The frequency of emitted photons shifts away from the excitation frequency due to the energy difference between the initial vibrational/rotational state and the end vibrational/rotational state. Fig.2.4 shows the principle of Raman scattering, in which, the types of scattering processes that can take place when light interacts with the material and the energy level diagram of Raman scattering and Rayleigh scattering process has been explained. the energy level diagram of Raman scattering process. The frequencies of the in-plane optical and out of plane optical phonon modes close to the Brillouin zone centre are revealed by Raman scattering. Raman spectroscopy is a useful method for characterising the materials since it is non-destructive and contactless. In this thesis, we employed a Horiba Jobin Yvon LabRam HR Evolution system and the back-scattering geometry for the Raman measurements. The measurements has been taken from the excitation source of a green diode laser operating at 532 nm.
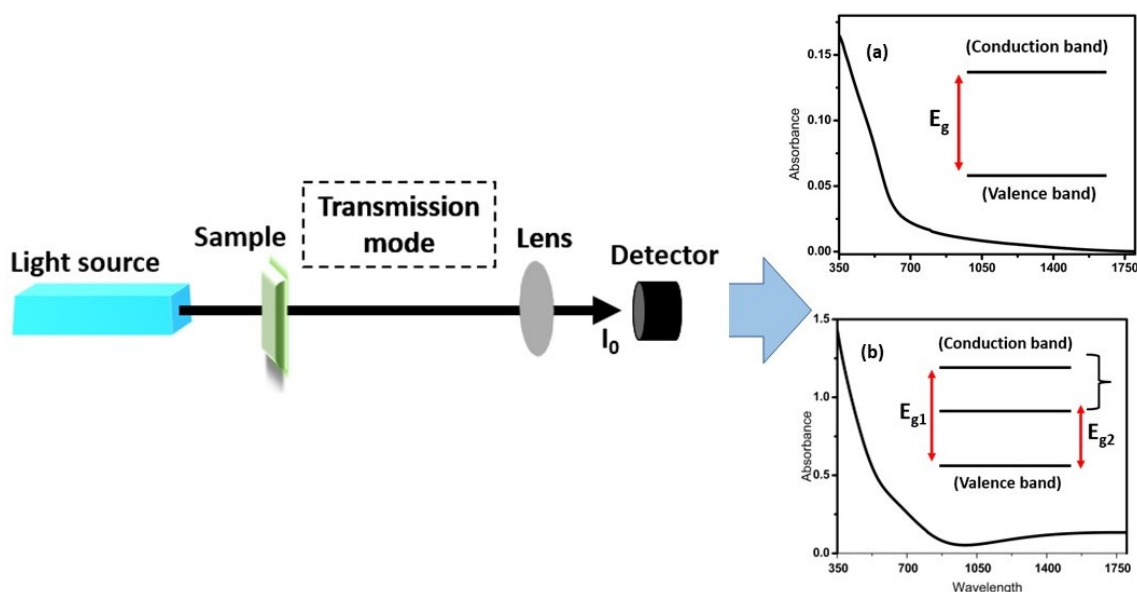
FIGURE 2.5: Schematic of uv-vis spectrometer. (a) Absorbance of the WSe_2 sample and corresponding single bandgap. (b) Absorbance of the WSe_2 sample which leads to the dual bandgap.

2.5 Absorption Spectroscopy

Ultraviolet-visible-near infrared spectroscopy (UV-Vis-NIR) is a powerful analytical tool for determining the optical characteristics (transmittance, absorbance and reflectance) of solids and liquids [16–20]. It can be utilized to analyze semiconductor materials, glass, coatings and a variety of other research and production materials. UV-VIS-NIR is operated in the optical regime between 175 nm to 3300 nm. The absorption spectroscopy is supplementary to fluorescence spectroscopy as, the fluorescence is associated with the transitions between the excited and ground states, whereas, the ground state to excited state transition is measured via absorption. The bonding and non-bonding electrons in the molecules can be stimulated to the excited states by absorbing the energy in the form of light (ultraviolet or visible). The electrons are excited more readily, if the energy gap between ground state and the excited state is lower and consequently, the longer wavelength of light can be

absorbed. Spectra can be collected from the smaller samples as well. In this work, the linear absorption measurements are performed using an Agilent Carry-5000 UV/VIS/NIR spectrometer. The measurements has been performed in transmission mode as the samples are transparent. The schematic of the uv-vis spectrometer is shown in Fig.2.5. In our work, the linear absorption spectra for the WSe_2 thin film was measured using *UV-visible* spectroscopy. The bandgap has been calculated using uv-vis data from Tauc plot. The Tauc fitting expression given by [21, 22],

$$\alpha h\nu = A(h\nu - E_g)^n \tag{2.2}$$

where α, hν, A and E_g are the linear absorption coefficient, photon energy, a constant and the bandgap respectively. n stands for the nature of transmission, n=2 for direct bandgap materials, while n=1/2 for indirect bandgap materials. We obtain the bandgap of WSe_2 films by extrapolating the linear part of the plot between $(\alpha h\nu)^{1/2}$ and $h\nu$. If the WSe_2 samples show the linear absorpton as in Fig.2.5(a), the bandstructure looks as in inset i.e. sample shows single bandgap. If the WSe_2 samples show the linear absorpton as in Fig.2.5(b), the sample shows dual bandgap, that will be discussed in section.3.3.

2.6 Nonlinear Optical Spectroscopy

The third-order ($\chi^{(3)}$) optical nonlinearities can be measured using a variety of characterisation techniques. These include third harmonic generation, optical Kerr-effect based measurements, time-resolved pump-probe technique, interferometric techniques, degenerate four-wave mixing, ellipse rotation, beam self-bending and two-beam coupling [23–29]. The above methods are reasonably sensitive techniques but they require a highly complex experimental arrangement. Among the methods available, *Z*-scan is the most straightforward and sensitive method for detecting third order optical nonlinearity. *Z*-scan is the
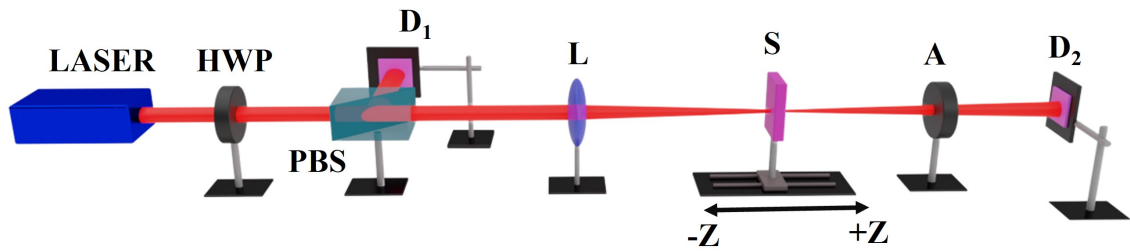
FIGURE 2.6: Schematic of Z-scan setup. HWP; Half-wave plate, PBS; Polarizing beamsplitter, L; Lens, S; Sample, A; Aperture, D_1 and D_2; Photo Detectors.

primary method used to characterise third-order optical nonlinearity in a variety of materials, including dyes, glass, crystals, polymers, metals, and semiconductors [30–36]. It also enables one to ascertain the contributions of nonlinear refraction and nonlinear absorption in the same set-up. As a result, in the current work, the single beam Z-scan approach was used to assess the third-order optical nonlinearity.

2.6.1 Z-scan Technique

The Z-scan method is based on the principle of spatial beam distortion. It is a straightforward method for determining the phase change in laser beam as it travels through a nonlinear material. In the Z-scan technique, the sample is moved along the direction of the laser beam, in order to measure the transmittance. It gives both the sign and magnitude of nonlinear absorption (β) and nonlinear index of refraction (n_2). A schematic of experimental Z-scan setup is shown in Fig.2.6. The source laser is fiber laser generating ultrashort pulsed delivering pulses at 1 KHz and 1 MHz repetition rate with a pulse-width of about 400 fs. The incident power of laser beam is controlled using a half wave plate (HWP) and a polarising beam splitter (PBS). Subsequently, the laser beam was focused using a lens (L). The reference and transmitted beam intensities were recorded using photodetectors D_1 and D_2 respectively. The position of the samples were perpendicular to beam axis and is

placed on a translation stage which translates from $-z$ to $+z$ through the focused Gaussian beam. When the sample passed through the focus of lens, it changed its transmittance and optical nonlinearity in the sample is manifested. An aperture is placed in the beam path just before the detector D_2 to enable two measurement techniques. In open aperture (OA) Z- scan measurement, the aperture was completely kept open to measure the nonlinear absorption of the sample under test. For the closed aperture (CA) Z-scan, the aperture is partially closed and the transmitted laser beam is collected by detector D_2 for ascertaining the nonlinear refractive index. The OA Z-scan transmission provide information about the nonlinear absorption coefficient of the sample but in CA Z-scan, the measured transmission is the combination of nonlinear refraction and nonlinear absorption. In order to obtain the contribution of pure nonlinear refraction in the CA Z-scan measurement, the measured CA Z-scan transmission is normalized with respect to the OA Z-scan transmission. When the OA transmittance is characterized by a peak at the focus ($z = 0$), β is negative and if the OA transmittance exhibits a valley at $z = 0$ (focus), β is positive. Similarly, if the CA Z-scan transmittance exhibits a valley to peak variation, n_2 is positive. On the other hand, if the variation is peak-to-valley then n_2 is a negative quantity.

2.6.2 Open Aperture Z-scan

The optical properties of a nonlinear material are significantly altered in presence of intense Gaussian laser beam. The nonlinear absorption contributes to absorption only at high laser intensities. The schematic representation of OA Z-scan is shown in Fig.2.7 which depicts maximum intensity at the laser focus ($z = 0$). The sample is translated through the focus as it moves from one end of the far-field to the other end. The far-field is dictated by the Rayleigh length of the laser and the distance between beam focus ($z = 0$) and the detector
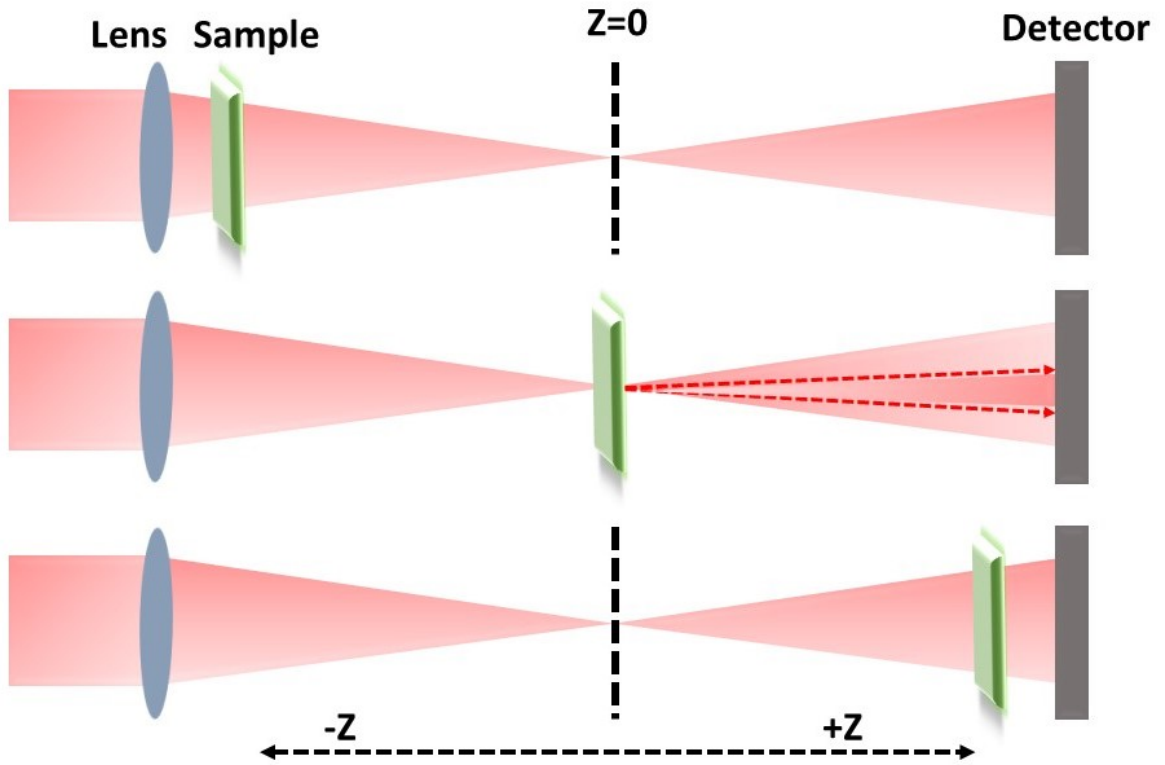
FIGURE 2.7: A schematic representation of OA Z-scan method

(aperture) should be more than 10 times of the Rayleigh length. Since the intensity is low in the far-field, only linear absorption contributes to the total absorption. As the beam comes closer to the focus (where the laser intensity is maximum), the absorption tends to change and Fig. 2.8 shows a typical OA Z-scan trace. The measured transmittance in the detector either decreases or increases as the sample gets closer to the focus, creating a valley or peak. The case, in which the measured OA transmittance produces a peak at the focus, is known as saturable absorption (SA) and the corresponding β is negative. On the other hand, the reverse saturable absorption (RSA) leads to a valley at the focus and the corresponding value of β is positive. In order to quantitatively estimate the value of
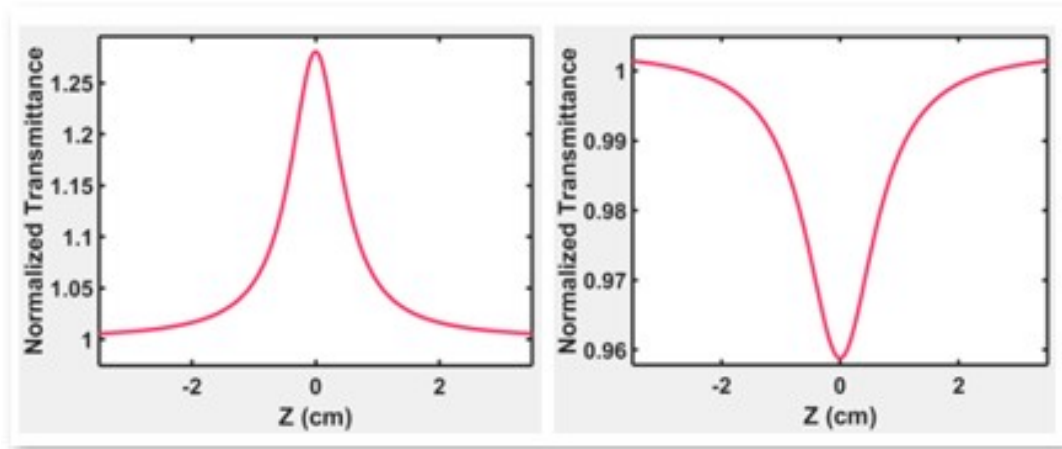
FIGURE 2.8: Schematic of OA Z-scan signal.

nonlinear absorption coefficient β, the measured OA normalized transmittance was fitted using the expression [37–42]

$$\Delta T = 1 - \frac{\beta I_0 L_{eff}}{2^{3/2}(x^2 + 1)} \tag{2.3}$$

β is the nonlinear absorption coefficient, I_0 is the laser intensity at the focal plane, L_{eff} is the effective length of the sample thickness; $L_{eff} = (1 - e^{-\alpha L})/\alpha$, L is the sample length, α is the linear absorption coefficient, $x = z/z_0$, z is the sample position, $z_0 = \pi \omega_0^2/\lambda$ is the Rayleigh length of the laser beam, ω_0 is the beam waist of focused Gaussian beam and λ is the laser wavelength. The imaginary part of the complex third-order nonlinear susceptibility ($\chi_{Im}^{(3)}$) is related to β and was obtained using the relation [43]

$$\chi_{Im}^{(3)} = \left[\frac{10^{-7} c n^2 \lambda}{96 \pi^2} \right] \beta \tag{2.4}$$

where c is the speed of light in vacuum, n is the linear index of refraction and λ is the excitation wavelength of laser beam. In order to eliminate the impact of linear absorption (α) on the nonlinear absorption (β), we define a figure of merit (FOM) as $FOM = |\chi_{Im}^{(3)}/\alpha|$ which provides a relative estimate of β.
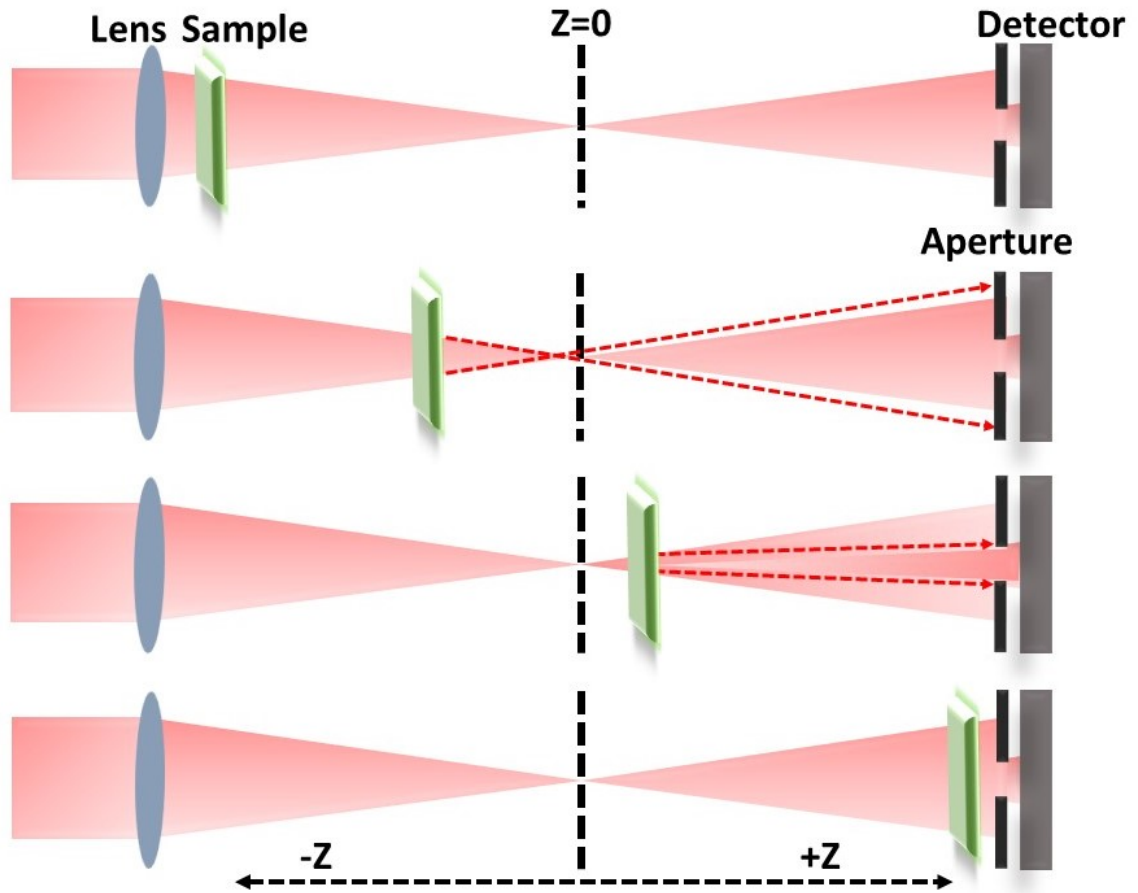
FIGURE 2.9: A schematic representation of CA Z-scan method

2.6.3 Closed aperture Z-scan

The CA Z-scan experiment is carried out for the purpose of determining the nonlinear index of refraction n_2. In the CA Z-scan, an aperture is placed in front of the photodetector, in order to monitor the sample transmittance in the far-field and consequnetly, only a small amount of light can enter the photodetector.

Figure 2.9 shows the schematic of a CA Z-scan signal for the positive n_2 values. The material behaves like an intensity dependent lens when a Gaussian laser beam passes through it. The change in input intensity causes a change in the effective focal length of
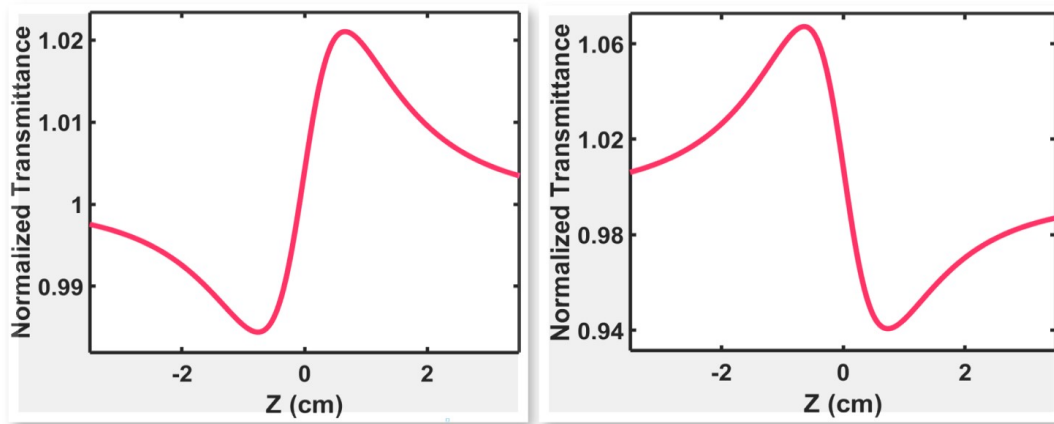
FIGURE 2.10: Schematic of CA Z-scan signal.

the medium along the beam path. This results in variable intensity distribution on the aperture. The sample position along the Z-axis determines the optical power transmitted through the aperture. Let us consider a sample having a positive nonlinear refractive index and the thickness less than the Rayleigh length. Since, the intensity of the beam is small in the far-field and the measured power on the detector stays nearly unchanged baring any scattering due to surface roughness. When the sample comes near the focal plane, the laser light tends to diverge more at the aperture plane owing to the self-focusing effect. This also means that the laser light gets focused much before the actual focal point. The detector power decreases as a result of this divergence which leads to the formation of a valley in the Z-scan transmittance. When the sample moves away from the focal point, the sample tends to collimate the beams and more light is transmitted through the aperture which results in a peak. Again, in regions far away from the focus, the intensity is low and consequently, the transmission through aperture does not change as a function of sample translation. Therefore, a material with a positive nonlinear refractive ($n_2 > 0$) index will exhibit the transmittance behaviour of a prefocal transmittance minimum (valley) followed

by a postfocal transmittance maximum (peak) (as shown in Fig.2.10). Similarly, a peak in the pre-focal point and a valley in the post-focal plane is the characteristic of a negative nonlinear refractive index ($n_2 < 0$).

In order to quantitatively estimate the value of nonlinear refractive index n_2, the measured CA normalized transmittance was fitted using the expression [24, 37, 39, 44]

$$\Delta T = 1 - \frac{4x\Delta\phi_0}{(x^2+9)(x^2+1)} - \frac{2(x^2+3)\Delta\Psi_0}{(x^2+1)(x^2+9)} \tag{2.5}$$

where $\Delta\phi_0 = kn_2 I_0 L_{eff}$ is the phase change due to nonlinear refraction at the focus, $k = 2\pi/\lambda$ is propagation constant and $\Delta\Psi_0 = \beta I_0 L_{eff}/2$ is the contribution of CA transmittance due to nonlinear absorption. The real part of complex third order nonlinear susceptibility ($\chi^{(3)}$) is related to n_2 and was obtained using a relation given by [43]

$$\chi_R^{(3)} = \left[\frac{n^2 c}{12\pi^2}\right] n_2 \tag{2.6}$$

Bibliography

[1] Ajit Behera, Shampa Aich, and T Theivasanthi. "Magnetron sputtering for development of nanostructured materials". In: *Design, Fabrication, and Characterization of Multifunctional Nanomaterials*. Elsevier, 2022, pp. 177–199.

[2] Ioan Valentin Tudose et al. "Chemical and physical methods for multifunctional nanostructured interface fabrication". *Functional Nanostructured Interfaces for Environmental and Biomedical Applications* (2019), pp. 15–26.

[3] Joseph I Goldstein et al. *Scanning electron microscopy and X-ray microanalysis*. Springer, 2017.

[4] Patrick Echlin et al. *Advanced scanning electron microscopy and X-ray microanalysis*. Springer Science & Business Media, 2013.

[5] John J Bozzola and Lonnie Dee Russell. *Electron microscopy: principles and techniques for biologists*. Jones & Bartlett Learning, 1999.

[6]   Ludwig Reimer. "Scanning electron microscopy: physics of image formation and microanalysis". *Measurement Science and Technology* 11.12 (2000), pp. 1826–1826.

[7]   Nicolas Brodusch et al. "Developments in field emission gun technologies and advanced detection systems". *Field Emission Scanning Electron Microscopy: New Perspectives for Materials Characterization* (2018), pp. 5–12.

[8]   Nicolas Brodusch et al. "Low Voltage SEM". *Field Emission Scanning Electron Microscopy: New Perspectives for Materials Characterization* (2018), pp. 37–46.

[9]   William Henry Bragg and William Lawrence Bragg. "The reflection of X-rays by crystals". *Proceedings of the Royal Society of London. Series A, Containing Papers of a Mathematical and Physical Character* 88.605 (1913), pp. 428–438.

[10]   WL Bragg and JJ Thomson. "Mr Bragg, Diffraction of Short Electromagnetic Waves, etc. 43". In: *Proceedings of the Cambridge Philosophical Society: Mathematical and physical sciences*. Vol. 17. Cambridge Philosophical Society. 1914, p. 43.

[11]   Bernard Dennis Cullity. *Elements of X-ray Diffraction*. Addison-Wesley Publishing, 1956.

[12]   PRGDJ Graves and D Gardiner. "Practical raman spectroscopy". *Springer* 10 (1989), pp. 978–3.

[13]   Derek Albert Long and DA Long. *The Raman effect: a unified treatment of the theory of Raman scattering by molecules*. Vol. 8. Wiley Chichester, 2002.

[14]   Wolfgang Kiefer. "The Raman effect? a unified treatment of the theory of Raman scattering by molecules. Derek A. Long, John Wiley & Sons, Ltd., 2002, Pp 597. ISBN 0-471-49028-8". *Journal of Raman Spectroscopy* 34.2 (2003), pp. 180–180.

[15]   Richard L McCreery. *Raman spectroscopy for chemical analysis*. John Wiley & Sons, 2005.

[16]   Douglas A Skoog, F James Holler, and Stanley R Crouch. *Principles of instrumental analysis*. Cengage learning, 2017.

[17]   Russell S Drago. *Physical methods for chemists*. 1992.

[18]   Douglas A Skoog, F James Holler, and Stanley R Crouch. *Instrumental analysis*. Vol. 47. Brooks/Cole, Cengage Learning Belmont, 2007.

[19]   Akul Metha. "Derivation of Beer-Lambert Law". *PharmaXChange. info* (2012).

[20]   Prabhakar Misra and Mark A Dubinskii. *Ultraviolet spectroscopy and UV lasers*. CRC Press, 2002.

[21]   J Tauc, Radu Grigorovici, and Anina Vancu. "Optical properties and electronic structure of amorphous germanium". *physica status solidi (b)* 15.2 (1966), pp. 627–637.

[22]   Sehun Seo et al. "Direct in situ growth of centimeter-scale multi-heterojunction MoS_2/WS_2/WSe_2/ thin-film catalyst for photo-electrochemical hydrogen evolution". *Adv. Sci.* 6.13 (2019), p. 1900301.

[23]   Mansoor Sheik-Bahae and Michael P Hasselbeck. "Third-order optical nonlinearities". *Handbook of Optics* 4 (2000), pp. 16–1.

[24]   Mansoor Sheik-Bahae, Ali A Said, and Eric W Van Stryland. "High-sensitivity, single-beam n_2 measurements". *Optics letters* 14.17 (1989), pp. 955–957.

[25]   R Sutherland. "Handbook of nonlinear optics Marcel Dekker Inc". *New York* (1996).

[26]   M Moran, Chiao-Yao She, and R Carman. "Interferometric measurements of the nonlinear refractive-index coefficient relative to CS 2 in laser-system-related materials". *IEEE Journal of Quantum Electronics* 11.6 (1975), pp. 259–263.

[27]   STEPHENR Friberg and PETERW Smith. "Nonlinear optical glasses for ultrafast optical switches". *IEEE journal of quantum electronics* 23.12 (1987), pp. 2089–2094.

[28]   Adelbert Owyoung. "Ellipse rotation studies in laser host materials". *IEEE Journal of Quantum Electronics* 9.11 (1973), pp. 1064–1069.

[29]   S Zongo et al. "Nonlinear optical properties of poly (methyl methacrylate) thin films doped with Bixa Orellana dye". *Applied Surface Science* 340 (2015), pp. 72–77.

[30]   S Zongo et al. "Linear and nonlinear optical absorption characterization of natural laccaic acid dye". *Applied Physics B* 120 (2015), pp. 389–396.

[31]   S Zongo et al. "Nonlinear optical properties of natural laccaic acid dye studied using Z-scan technique". *Optical Materials* 46 (2015), pp. 270–275.

[32] Carlos Jacinto et al. "Thermal lens and Z-scan measurements: Thermal and optical properties of laser glasses–A review". *Journal of Non-Crystalline Solids* 352.32-35 (2006), pp. 3582–3597.

[33] HP Li et al. "Femtosecond Z-scan measurements of nonlinear refraction in nonlinear optical crystals". *Optical materials* 15.4 (2001), pp. 237–242.

[34] David D Smith et al. "Z-scan measurement of the nonlinear absorption of a thin gold film". *Journal of applied physics* 86.11 (1999), pp. 6200–6205.

[35] Marek Samoc et al. "Third-order optical nonlinearities of oligomers, dendrimers and polymers derived from solution Z-scan studies". *Optical materials* 21.1-3 (2003), pp. 485–488.

[36] M Yin et al. "Determination of nonlinear absorption and refraction by single Z-scan method". *Applied Physics B* 70 (2000), pp. 587–591.

[37] Mansoor Sheik-Bahae et al. "Sensitive measurement of optical nonlinearities using a single beam". *IEEE journal of quantum electronics* 26.4 (1990), pp. 760–769.

[38] S Bikorimana et al. "Nonlinear optical responses in two-dimensional transition metal dichalcogenide multilayer: WS_2, WSe_2, MoS_2 and $Mo_{0.5}W_{0.5}S_2$". *Opt. Express* 24.18 (2016), pp. 20685–20695.

[39] Km. Surbhi et al. "Impact of pauli-blocking effect on optical limiting properties of WSe_2 thin films". *Optical Materials* 129 (2022), p. 112479. ISSN: 0925-3467.

[40] Km Surbhi and Ritwick Das. "Impact of Optical Fluence on Pauli Blocking Effect in WSe_2 Thin Film". In: *Photonic Networks and Devices*. Optica Publishing Group. 2022, JW3A–39.

[41] Km Surbhi et al. "Impact of defects on the $\chi^{(3)}$ optical nonlinearity of sputtered WSe_2 thin films in the optical communication band". *Journal of Applied Physics* 132.24 (2022), p. 243101.

[42] Km Surbhi and Ritwick Das. "Free-carrier assisted optical nonlinearity in WSe_2 thin films near the optical communication band". In: *Laser Science*. Optica Publishing Group. 2022, JW4A–88.

[43] Kangpeng Wang et al. "Broadband ultrafast nonlinear absorption and nonlinear refraction of layered molybdenum dichalcogenide semiconductors". *Nanoscale* 6.18 (2014), pp. 10530–10535.

[44] Samir Kumar et al. "Phase-dependent ultrafast third-order optical nonlinearities in metallophthalocyanine thin films". *J. Appl. Phys.* 120.12 (2016), p. 123104.

Chapter 3

Nonlinear optical response of as-prepared WSe_2 thin films

In this chapter, we present the nonlinear optical (NLO) characteristics of the RF-sputtered WSe_2 thin films in the visible and near-infrared (NIR) spectrum. Moreover, the impact of laser parameters (such as repetition rate and laser intensity) and film thickness on the third order NLO properties in WSe_2 thin films is also explored. The chapter has been arranged in the following way : the WSe_2 thin-film preparation and characterization are discussed in section 3.2. The impact of film thickness on the structural and optical properties is explained in section.3.3. This is followed by the measurement of nonlinear optical response of the WSe_2 thin films in the visible spectrum which includes the impact of repetition rate and film thickness given in section 3.4. The nonlinear optical response of the WSe_2 thin films in NIR spectrum which includes the impact of film thickness and laser intensity, is discussed in section 3.5.

3.1   Introduction

The layered transition metal dichalcogenides (TMDs) have received significant attention in the precedent few years due to their distinctive physical, optical and electronic properties [1–5]. Despite being studied for decades, current developments in these materials characterization and device manufacturing have opened up new potential for 2D layers of thin TMDs. The electronic bandstructure of TMDs is greatly influenced by the number of monolayers and changes as the thickness increases from direct to indirect [6, 7]. The potential of customising the bandstructure (or bandgap) allows the regulation of hyperpolarizability from the standpoint of nonlinear optical (NLO) properties, and as a result, one might restrict the thickness of TMDs to suit a particular application [8–18]. In our work, we have shown the impact of film thickness in visible as well as NIR spectral band and it has been observed that samples are showing different behaviour in different wavelength regime which is basically due to the dependency on the bandstructure of the WSe_2 films.

3.2   Thin film preparation and characterization

The WSe_2 thin films were prepared using a RF magnetron sputtering system with a WSe_2 (99.9% pure) target in an argon environment at room temperature. WSe_2 thin films with a desired thickness were sputtered onto a $1\ cm \times 1\ cm\ SiO_2/Si$ and glass substrate. Prior to the deposition, the chamber was evacuated by a turbomolecular pump to a vacuum of 3.1×10^{-6} mbar. Throughout the deposition process, the Ar gas concentration was maintained at 15 $sccm$, and the power was fixed at 60 W. The depositions were performed at a pressure of 1×10^{-2} mbar. The number of samples are prepared by varying the time for which deposition takes place which essentially results in a thicker thin film.

The morphological features of the RF-sputtered WSe_2 thin-films is investigated through

field-emission scanning electron microscope (FESEM). The crystal structure and phase analysis is carried out using X-ray diffraction spectrum (X-ray diffractometer, Rigaku Smartlab) with Cu Kα (λ = 1.5418 Å). The Raman spectrum were measured using a Raman spectrometer (Jobin Yvon LabRam HREvolution, Horiba) with an excitation at 532 *nm* wavelength. The linear absorption spectrum of the WSe_2 thin films were carried out using a UV-VIS-NIR spectrometer (Agilent carry 5000 UV-Vis-NIR). The nonlinear optical absorption measurements of the WSe_2 thin film were performed using the single-beam open-aperture (OA) and closed-aperture (CA) Z-scan technique discussed in chapter 2.

3.3 Impact of film thickness on the structural and optical properties

For the measurements, we have prepared a set of six WSe_2 thin films using RF-sputtering system under the conditions described in section 3.2. The homogeneity of structure and thickness of the samples is estimated from FESEM images. The cross-sectional FESEM is performed to obtain the thickness of the deposited thin films. The thicknesses were measured to be 34 nm, 81 nm, 130 nm, 150 nm, 242 nm and 326 nm. In Fig. 3.1, representative top-view images of WSe_2 thin films of all the thicknesses respectively are shown. All the figures except Fig. 3.1(e) appears to exhibit a smooth surface. The insets represent the respective cross-sectional images. The study of crystal structure, crystallite sizes, strain, dislocation density and quantitative phase analysis is carried out using X-ray diffraction (XRD) spectrum of the WSe_2 thin films. The XRD peaks for all the thin films could be seen in Fig.3.2(a). The measured XRD peaks of WSe_2 films match reasonably well with JCPDS data card no 71-0600. One peak was consistently obtained at an angle
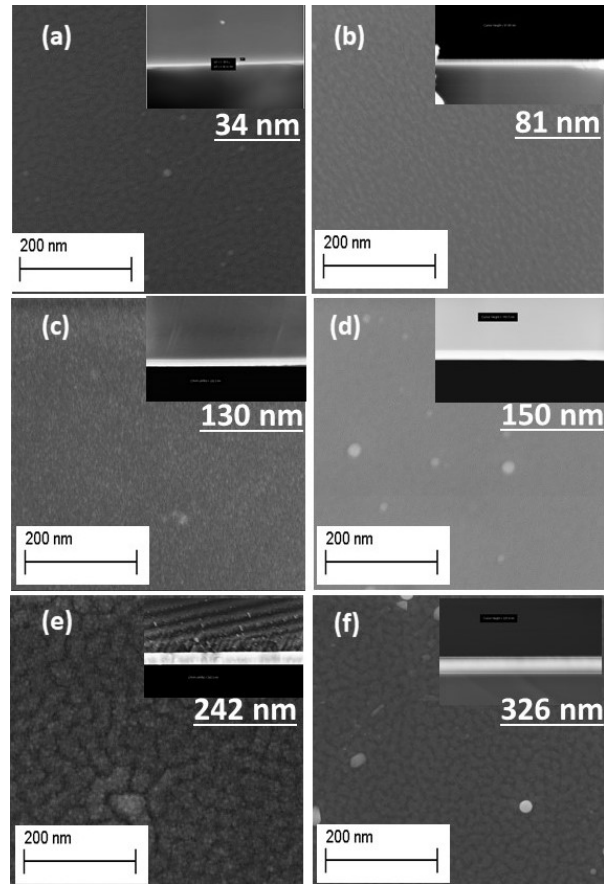
FIGURE 3.1: Field Emission Scanning Electron Microscopy (FESEM). (a)-(f) shows top surface images of WSe_2 thin films having thickness of 34 nm, 81 nm, 130 nm, 150 nm, 242 nm and 326 nm respectively. Insets show cross-sectional FESEM images for determining thickness.

27.5∘ which is a consequence of (004) plane. The crystallite sizes were estimated through the Debye- Scherrer formula while strain and dislocation density is calculated using the recipe prescribed in the Ref.[19]. Fig.3.2(b) shows the variation of strain and dislocation density as a function of WSe_2 film thickness. The variation of dislocation density and strain exhibit a similar trend and maximize for the film of thickness 326 nm. This XRD spectrum distinctly depicts the presence of defects for thicker thin-films which would be investigated later in detail. Raman spectroscopy was employed to ascertain the vibrational
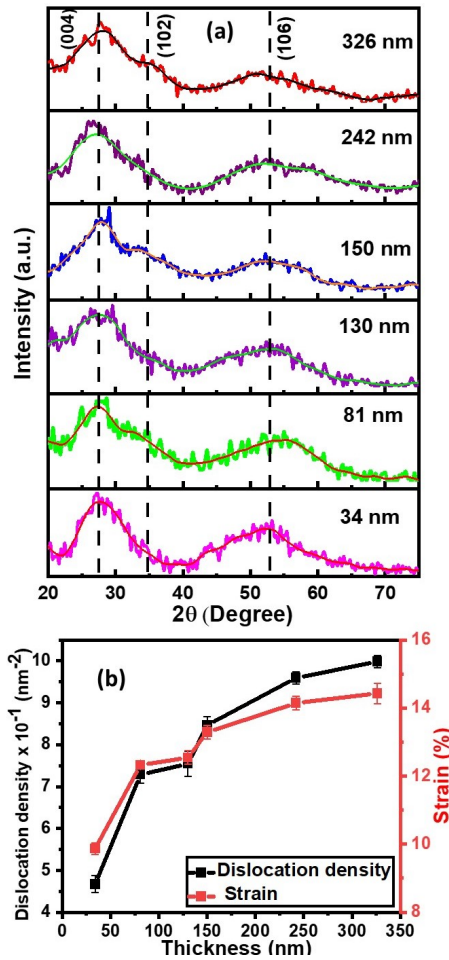
FIGURE 3.2: (a) X-ray diffraction spectrum of RF-sputtered WSe_2 thin films. (b) Variation of strain and dislocation density (D) in WSe_2 thin films as a function of thickness.

modes of the deposited thin WSe_2 films. Fig 3.3(a) shows the Raman spectrum for all the WSe_2 thin-films. The spectrum for all the films exhibit the three characteristic phonon modes. The peak corresponding to E_{2g}^1 mode is associated with in-plane vibration of W and Se atoms. The sharp peak corresponds to A_{1g} is related to out-of-plane vibration of Se atoms. The peak corresponding to B_{2g}^1 mode is essentially due to the vibration of W and Se atoms owing to the interlayer interactions [20–23]. All the peak intensities and shifts were calculated by deconvoluting the measured Raman spectra with multiple peaks. A representative plot showing the deconvoluted spectrum is shown in Fig.3.3(b) (for 34
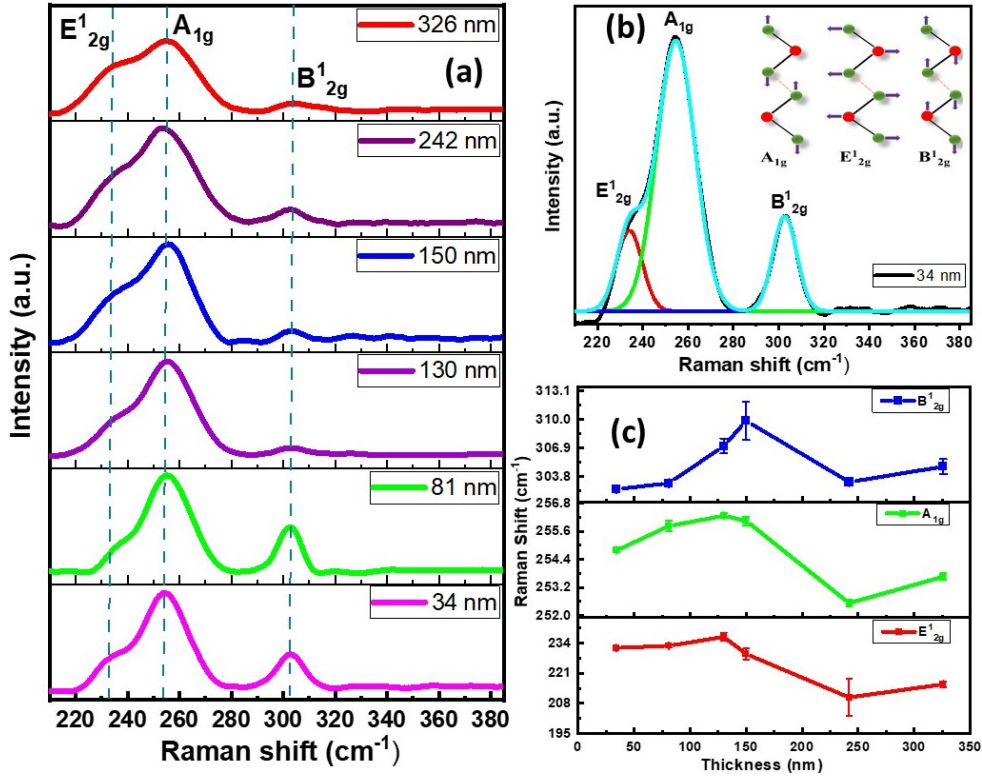
FIGURE 3.3: (a) Raman spectrum of WSe_2 thin films. (b) Variation of Raman modes of film as a function of film thickness. (c) The multiple-peak fit for 34 nm film. Insets show the schematic of possible vibrational modes.

nm thick WSe_2 film). The inset shows the schematic of displacement of W and Se atoms representing the plane of vibration in Raman active modes. For bulk WSe_2 crystal, E_{2g}^1 and A_{1g} modes are degenerate, yielding single peak as compared to other TMDs materials. Sahin *et al.* [24] have demonstrated that a small crystal symmetry-breaking by virtue of uniaxial strain leads to lifting off the degeneracy between two peaks. We observed that nearly $9 - 10\%$ of strain exist for 34 nm film and increases with thicker WSe_2 films due to large number of dislocations. This could be estimated from the XRD pattern and it is presented in Fig 3.2(b). Such strains are obvious at room temperature sputtered thin films. This is also the reason behind observing two distinct E_{2g}^1 and A_{1g} phonon modes in all the WSe_2 films. The variation of Raman-active modes as a function of WSe_2 film thickness is
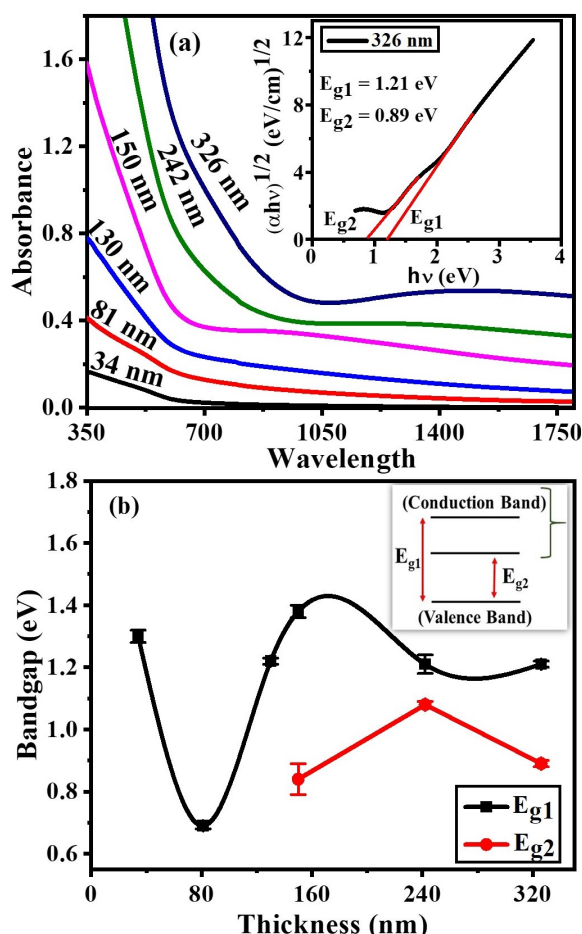
FIGURE 3.4: (a) Absorption spectrum of WSe_2 thin films. Inset shows the Tauc plot for estimating the bandgap. (b) Variation of bandgap as a function of WSe_2 fim thickness. Inset: a schematic diagram to represent E_{g1} and E_{g2} in the present context.

shown in Fig.3.3(c). It has been observed that the Raman shift for all the vibrational modes reduces for the film of thickness 242 nm, which can be attributed to the surface defects and that could be corroborated with the increased surface roughness observed in the FESEM image of Fig.3.1(e). The small change in the Raman shift for the film thickness of 326 nm arises because the better surface uniformity. The linear absorption spectrum for all the WSe_2 thin films are measured using UV-visible spectroscopy which is shown in Fig 3.4(a). The absorbance tends to reduce at longer wavelengths for all the samples. However, a small

increase in absorbance for WSe_2 films with thicknesses $\geq$ 150 nm, depicts the presence of two bandgaps. The variation of bandgap(s) as a function of WSe_2 film thickness is shown in Fig 3.4(b) which distinctly depicts the existence of two separate bandgap arising as a consequence of the presence of defects in the films. From one perspective, the appearance of mid-gap states (or bands) is attributed to the Se (lighter atom) deficiency in the thin-films grown using RF-sputtering technique. In other words, the deposition method introduces stoichiometric defects (absence of Se atoms) which is distributed randomly throughout the thin-film architecture.

In order to gain a deeper insight, we simulated the electronic bandstructure for a WSe_2 crystal using density functional theory (DFT) which utilizes the Vienna ab-initio simulation package (VASP) code [25]. The interaction between electrons and ions is introduced by using Projector-Augmented Wave (PAW) method [26]. In these calculations, the structural relaxation is accomplished by deploying generalized gradient approximation (GGA) scheme for adopting the exchange–correlation potential with the Perdew, Burke, and Ernzerhof (PBE) functional [27]. A cut-off energy of 350 eV is fixed for plane-wave basis set for all the calculations. The Monkhorst–Pack method [28] are redacted to generate the $5 \times 5 \times 5$ k-point meshes for achieving the required convergence within 10^{-6} eV per atom. When the forces reached smaller than the value of 0.01 $eV/$ for each atom, the relaxation is assumed to be completed. The band structure and density of states (DOS) estimations are obtained by considering the geometry which results in most stable configuration and we obtain desirable convergence using the linear tetrahedron method with Bloch corrections [29]. Fig. 3.5(a) shows the simulated bandstructure for WSe_2 which distinctly depicts a bandgap of 1.4 eV at the high-symmetry K-point in the Brilliouin zone. Also, it is worth mentioning that the energy difference between the conduction band (yellow solid curve) and the valence band (blue solid curve) at other high symmetry points (Γ and M) are greater than that at the
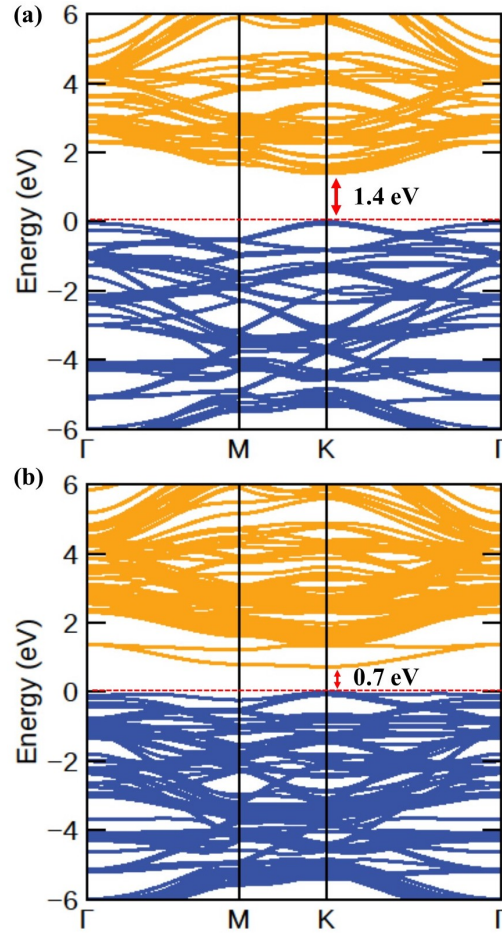
FIGURE 3.5: Simulated bandstructure of (a) pure WSe_2 crystal (b) WSe_2 crystal in presence of a defect induced by Se deficiency.

K-point which is expected for a hexagonal lattice. At this point, we introduce a Se defect (absence) from a supercell comprising of 16 W atoms. This results in a bandstructure shown in Fig. 3.5(b) where the defect band is separated from the valence band by about 0.7 eV at the K-point. Also, it is apparent that the mid-gap defect band is degenerate at the Γ-point ($\approx$ 1.4 eV) and varies between 0.7 eV to 0.8 eV between M-point and K-point in the Brilliouin zone. It is worth recalling that the bandgap estimation of WSe_2 films using the UV-visible absorption spectrum in Fig. 3.4(b) which shows the existence of a defect band and it varies between $0.8 - 1.0$ eV for film thicknesses $\geq$ 150 nm. In order to
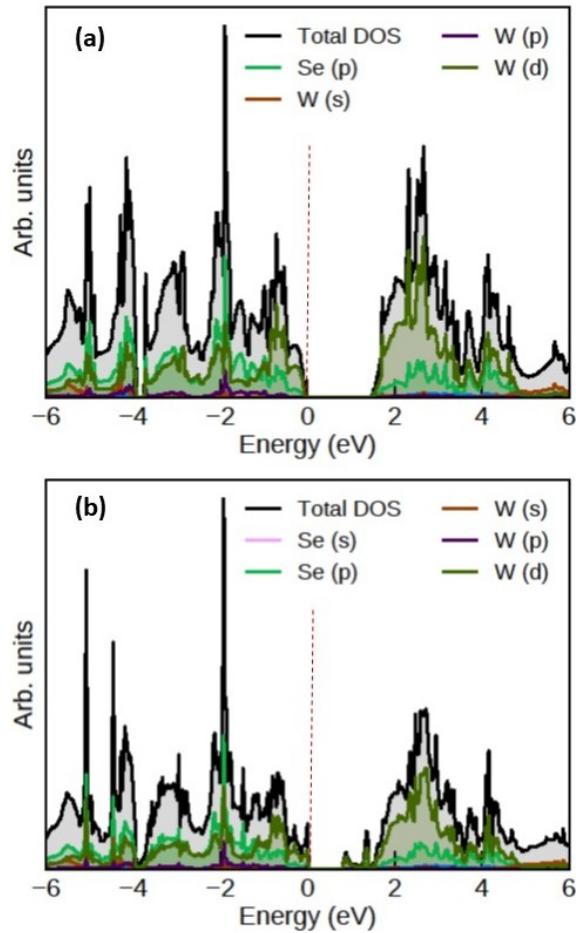
FIGURE 3.6: DOS of (a) pure WSe_2 crystal (b) WSe_2 crystal in presence of a defect induced by Se deficiency.

observe a manifestation of this, we calculated the total density of states (DOS) as shown in Fig 3.6. Fig.3.6(a) shows the actual DOS of a pure WSe_2 crystal where the valence band is comprised of W-p,W-d and Se-p orbital. The conduction band, on the other hand, essentially involves W-d and Se-p orbital. Fig.3.6(b) represents the DOS in presence of defects (Se-deficiency) in the WSe_2 matrix. It could be observed from Fig.3.6(b) that the new localized DOS appear in the $0 - 2\ eV$ region (bandgap in pure WSe_2) which primarily involves transitions from d-orbital of Tungsten (W) atom. The energy spectrum for such states originating from the d-orbital for W are situated within the intrinsic bandgap of

WSe_2 and the impact is more in thin-films of greater thickness. It is worth noting that the measured absorption spectrum correlates reasonably well with the theoretical simulations which allows us to conclude that the creation of defect band is primarily associated with *Se*-deficiency. Within the computational limitation of exactly positioning and identifying the defect sites, the numerically simulated bandstructure provides a plausible explanation for the absorption characteristics and existence of dual bandgap in WSe_2 thin films. The presence of the defect states have a direct and significant impact on the NLO properties of as-prepared WSe_2 thin-films which is discussed later.

3.4   Nonlinear optical properties in visible spectral band

The impact of film thickness on the structural and optical properties has been studied in section.3.3. It has been observed that with the increase in thickness, surface morphology has changed, the strain and dislocation density is increased, and a change in Raman shift is observed. From the bandgap estimation, it is also inferred that the thicker films show dual bandgap, which is further confirmed through DFT simulations. In order to observe the impact of the thickness on the NLO properties, we have performed Z-scan measurements.

Impact of film thickness on the nonlinear optical properties

Our work essentially focus on investigating spectral dependence of $\chi^{(3)}$ NLO properties of tungsten-selenide (WSe_2) thin-films which have been grown using RF sputtering technique. The NLO investigations, which were carried out using single-beam Z-scan technique.
We measured the Z-scan OA transmission of WSe_2 thin films at an excitation wavelength of 515 *nm* and a peak on-axis intensity of $I_0 \approx 3.20 \times 10^{11}$ W/cm^2 at the focal point. The OA normalized transmittance is shown in Figs 3.7(a)-3.7(f) respectively. It could be observed from the figures that the OA normalized transmittance exhibited a maxima at
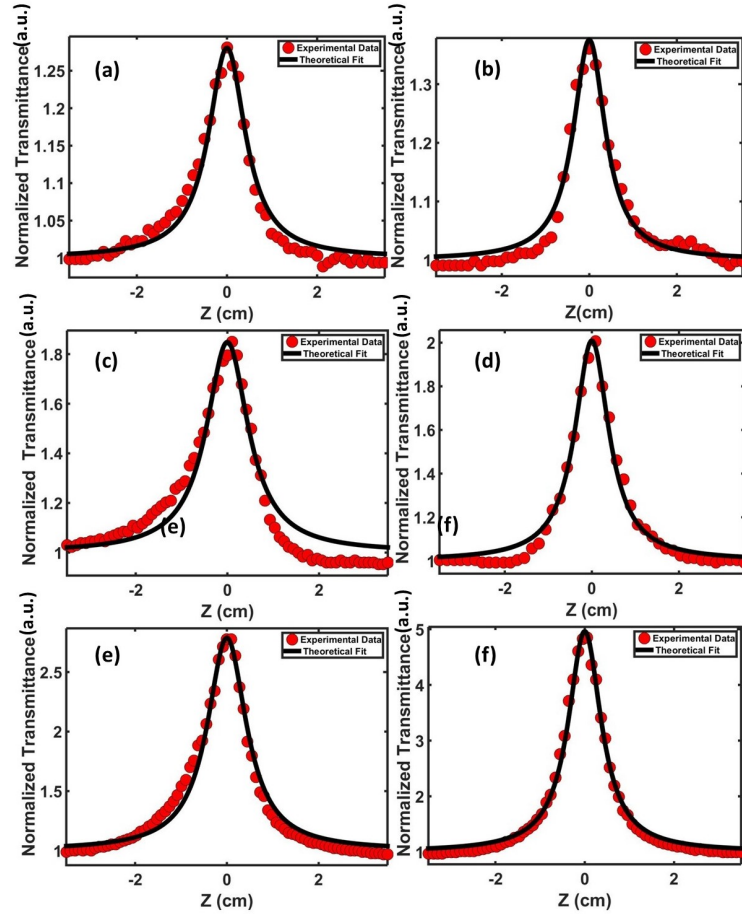
FIGURE 3.7: Open aperture (OA) Z-scan normalized transmittance for WSe_2 thin films of thicknesses 34 *nm* (a), 81 *nm* (b), 130 *nm* (c), 150 *nm* (d), 242 *nm* (e) and 326 *nm* (f). Red dots represent the experimentally measured values and black solid curve represent the theoretical fitting (solid lines).

the focal point of the lens ($z = 0$) where the laser intensity is maximum. This is distinct signature of saturable absorption (SA) behaviour. As expected, it could be noted that the linear absorption monotonically increases from 4.25 cm^{-1} to 19.07 cm^{-1} as a function of increasing WSe_2 film thickness. Also, β exhibits an approximately 25-fold increase when film thickness increases from 34 *nm* to 326 *nm*. Except a small irregular behaviour for 130 *nm* thin-film, the FOM also exhibits an increasing trend with the film thickness. Consequent upon this observation, it could be safely inferred that the WSe_2 thin-films

TABLE 3.1: Estimated values of nonlinear absorption, nonlinear refraction coefficients, real and imaginary part of $\chi^{(3)}$ of the WSe_2 sample at 515 nm excitation wavelength.

Sample (nm)	T_0 (%)	$\alpha \times 10^4$ (cm^{-1})	$\beta \times 10^{-7}$ (cm/W)	$n_2 \times 10^{-12}$ (cm^2/W)	$\chi_{Im}^{(3)} \times 10^{-10}$ (esu)	$\chi_R^{(3)} \times 10^{-13}$ (esu)	FOM$\times 10^{-14}$ (esu cm)
34	65.40	12.24	−4.23	3.16	−1.96	2.27	0.16
81	57.76	6.87	−6.49	4.51	−2.73	4.85	0.40
130	43.65	6.53	−8.87	8.28	−5.41	5.76	0.83
150	36.70	6.12	−9.77	11.76	−7.49	11.42	1.22
242	28.27	5.22	−11.59	13.89	−14.20	14.43	2.72
326	14.84	5.85	−23.39	28.94	−27.36	33.07	4.68

exhibit a SA behaviour at an excitation wavelength of 515 *nm* which tends to increase with film thickness. Although not shown here, the OA Z-scan measurements show a similar SA behaviour for all excitation wavelengths in the visible band of the electromagnetic spectrum.

In order to get a deeper insight into the SA characteristics exhibited by WSe_2 thin-films, we note that the primary bandgap (E_g) for most of the WSe_2 films are in $1.2 - 1.4$ *eV* range (see Fig.3.4(b)). Therefore, one-photon absorption is expected to be the most dominant absorption process for 515 *nm* wavelength excitation [30]. In case of WSe_2 thin-films, the OA Z-scan transmission peak at focus ($z = 0$) is higher for thicker films and therefore, it could be inferred that the Pauli-blocking effect [31, 32] is more dominant in thicker films. Further, the bandstructure in Fig. 3.5(a) depicts that the Pauli-blocking effect is expected to weaken when the *one-photon* (or linear) absorption is small. At this point, it would be interesting to observe that the dependence of nonlinear absorption coefficient (β) on WSe_2 film thickness at 515 *nm* excitation wavelength. This is shown in Fig. 3.8 which depicts an enhanced saturable absorption characteristics as a function of thin-film thickness. We note that β exhibits an inverse dependence with bandgap (E_g) of the films under investigation. Also, a thicker WSe_2 film (closer to bulk crystal) is expected to have a higher carrier density

owing to denser stacking of WSe_2 monolayers. This essentially leads to high occupation of states around the band-edges at high laser intensity (high photon flux), thereby creating a situation for dominant impact of Pauli-blocking. This also manifests into an weaker absorption at high photon-flux (high intensity) which leads to a higher transmission peak at $z = 0$ in Fig. 3.7 for thicker WSe_2 films. Alternately, this results in stronger SA features in thicker WSe_2 films as depicted in Fig. 3.8. It could also be observed that the enhancement in SA behaviour increases significantly for WSe_2 film thickness $\geq 150\ nm$. A natural consequence of dense stacking of WSe_2 monolayers manifests in the form of defects whose impact was discussed in the context of dual-bandgap in Fig.3.4(b). At 515 nm excitation wavelength, the defect states provide a more favorable situation for charge carrier accumulation near the band edges, thereby fostering the possibility of an stronger impact of Pauli-blocking effect and improved SA characteristics which is depicted in Fig.3.8. Therefore, it could be concluded that the presence of defects in WSe_2 thin-films provides a platform for enhancing the SA efficiency through a dominant Pauli-blocking effect.

The present investigation also includes the measurements on nonlinear refractive index (n_2) using CA Z-scan transmittance. The measured CA normalized transmittance for all the WSe_2 thin films at 515 nm excitation wavelength is shown in Figs.3.9(a)-(f) (red dots). The CA transmittance exhibits a pre-focal minima which is followed by a post-focal maxima which is a distinct signature of positive n_2 values for all the WSe_2 thin-films [10]. However, the asymmetry in the peak-to-valley transmittance is essentially brought about by strong saturable absorption exhibited by all the thin-films at 515 nm excitation wavelength. The values of n_2 and $\chi_R^{(3)}$ are estimated by fitting (solid black curve in Fig.3.10) the experimental measurements using Eq. (2.5) and (2.6), represented in Table-3.2. In case of thinnest film (34 nm) thickness, n_2 was estimated to be 2.81×10^{-16} cm^2/W whereas the thickest film
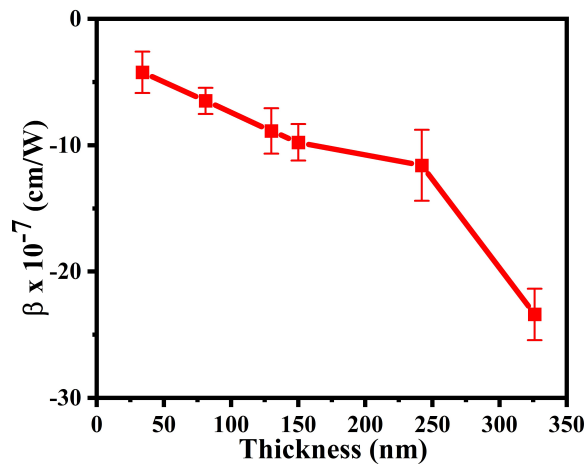
FIGURE 3.8: Variation of nonlinear absorption (saturable absorption) coefficient β (at 515 nm excitation wavelength) as a function of thickness.

(326 *nm* thickness) had $n_2 = 59.92 \times 10^{-16}$ cm^2/W which is approximately a 21-fold increase.

It is important from the application point of view to know the factors that can affect the optical nonlinearity and hence, their impact on device performance could be ascertained. There are a few laser parameters through which the NLO response could be modified or controlled. We will discuss about the two laser parameters i.e. pulse repetition rate and laser intensity [33, 34]. The impact of repetition rate is discussed in this section while, laser intensity will be discussed in the next section.

Impact of the repetition rate on the nonlinear optical properties

From the application viewpoint, it is important to study the impact of thermal effects on NLO response. At high repetition rate, thermal diffusion effects come into play [35], which can substantially alter the nonlinear optical behaviour of the medium. Therefore, we study the impact of high repetition rate on the third order NLO properties in WSe_2 thin films at 515 nm excitation wavelength. In order to perform this study, we carried out the Z-scan
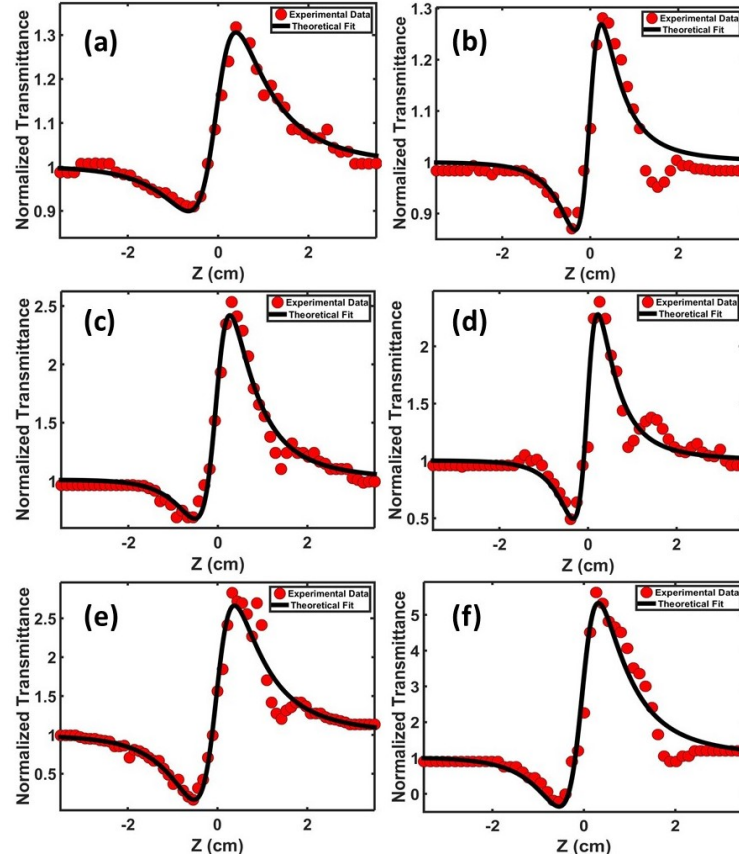
FIGURE 3.9: Closed aperture (CA) Z-scan normalized transmittance for WSe_2 thin films of thicknesses 34 *nm* (a), 81 *nm* (b), 130 *nm* (c), 150 *nm* (d), 242 *nm* (e) and 326 *nm* (f). Red dots represent the experimentally measured values and black solid curve represent the theoretical fitting (solid lines).

measurements at *1 kHz* and *100 kHz* repetition rate and estimated the parameters. The calculated nonlinear optical parameters for WSe_2 thin-film are tabulated in Table.3.1. As we have discussed earlier that the thermal effects can alter the nonlinear optical response of the material. The thermal diffusion effects comes into play when time-difference between the incidence of two adjacent pulses is shorter than the thermal lifetime ($t_c = w_0^2/4D$) for the medium where w_0 is beam-spot size and D is thermal diffusion coefficient for the thin-film. In case of WSe_2 thin-films, $D \sim 1 \times 10^{-3} \, cm^2/sec$ which results in $t_c \approx 1.4 \, ms$. This implies that the NLO measurements using ultrashort pulsed lasers with $R \gg 1 kHz$ are

TABLE 3.2: Nonlinear absorption and nonlinear refraction coefficients of the WSe_2 thin film sample at 515 nm excitation wavelength.

Repetitin rate	$I_0(W/cm^2)$	$\beta(cm/W)$	$n_2(cm^2/W)$
1 kHz	6.4×10^{12}	-1.74×10^{-8}	-1.15×10^{-13}
100 kHz	3.16×10^{10}	-1.15×10^{-6}	-3.53×10^{-11}

inevitably accompanied by thermal effect induced manifestations. In other words, the WSe_2 film does not return to the equilibrium state (or temperature) within the time-period between the incidence of two pulses at *100 kHz* repetition rate. This results in the onset of diffusion induced accumulated thermal effect (ATE). The contribution of ATE is apparent from the values of n_2 and β in Table-1 which shows about two-orders of magnitude enhancement for 100 *kHz* repetition rate. This investigation suggests that the electronic contribution to NLO properties maximizes at low pulse repetition rates, preferably at time-scales lesser than the thermal lifetime. The NLO coeffcents tends to increase at high repetition rate owing to the thermal diffusion effect. The investigation provides a basis for the choice of WSe_2 thin-films in Q-switching, mode-locking and optical switching applications.

In the visible domain Pauli-blocking induced strong saturable absorption characteristics in WSe_2 films allow a deep signal modulation which facilitate desirable shaping of optical pulses. In fact, the depth of modulation for pulse generation as well as shaping is directly proportional to $|\beta|$ [36] and consequently, WSe_2 thin-films exhibiting strong Pauli-blocking induced SA behaviour would serve the purpose very efficiently. It has been demonstrated that stable high-energy nanosecond pulses could be generated by employing a few layer WSe_2 sheets (acting as saturable absorber) through passive Q-switching in Pr^{3+}-doped ZBLAN fiber laser emitting at 635 *nm* wavelength [37]. In a similar investigation, B. Chen *et al*. have employed an arbitrarily thick WSe_2 film as a saturable absorber for generating Q-switched nanosecond pulses in erbium doped fiber laser [38]. This idea has been extended

for generating ultrashort pulses through passive mode-locking technique as well [39]. In a recent investigation, a few layer alternating $MoSe_2$ and WSe_2 nano-sheets have shown generation of stable ultrashort pulses of a few picoseconds in the NIR band [40]. In fact, the broadband SA characteristics exhibited by WSe_2 films give rise to the possibility of developing highly-efficient wavelength-tunable pulse-shaping components in the visible as well as NIR spectrum [14, 41]. In order to compress pulses to very low time-scales (say $\leq 100\ fs$), it is essential to proportionally scale-up the nonlinear absorption (β) of WSe_2 sheets. This flexibility, in general, is limited in all the aforementioned illustrations which is primarily due to the presence of a few monolayers of WSe_2. The RF-sputtered thin-films, which are experimentally simpler to fabricate, provide a plausible route to tailor β. As shown here, thicker films exhibit larger $|\beta|$ and consequently, they could be employed in situations requiring greater depth of modulation.

3.5 Nonlinear optical properties in near-infrared (NIR) spectrum

Passive optical power limiters have been widely employed in optical communications and military applications such as to provide frequency-agile protection by limiting the influx of hazardous radiation. The potential advantage is derived from the possibility of inherent and automated control due to the fact that the optical limiting properties originate from the intrinsic properties of the material. From an application viewpoint, the third-order optical nonlinearity which includes the nonlinear absorption (NLA) is becoming a crucial property to explore. In addition, the materials exhibiting high optical nonlinearity induced absorption has found applications in a wider spectrum including optical switch designing, optical routing in monolithically-integrated optical circuitry and optical channel blocking as well

as limiting. From a material perspective, two-dimensional (2D) sub-wavelength materials form an emergent and promising platform for photonic and opto-electronic applications. Such a feature is essentially brought about by strong intra-layer covalent bond and weak inter-layer vander Waals forces which also permits TMDs to be fabricated into compact, efficient and flexible optical devices. In addition, the impact of high optical fluence on the TMD films is extremely crucial from the application point of view. At high optical intensities, TMD thin films are expected to exhibit *free-charge carrier* induced modifications in electron transport properties which could affect the device performance during operation. Therefore, the possible modifications in the NLO behaviour of TMD films at high optical intensities in the desirable spectral band require further investigation.

In this work, we present a detailed investigation of nonlinear optical properties of WSe_2 thin film using single-beam Z-scan technique [42]. Bikorimana *et al.* investigated that the WSe_2 multilayers exhibit two photon absorption (TPA) effect at 1064 nm excitation wavelength [43]. At an excitation wavelength of 1040 nm, Dong *et al.* also observed a TPA behaviour in WSe_2 few monolayer films [44]. However, the NLO behaviour of TMD thin films for excitation wavelengths in the communication band (1520 − 1570 nm) is an extremely important feature from the perspective of designing Q-switching and mode-locking architectures for devising monolithically-integrated near-infrared laser diode modules. We present a comprehensive investigation on the NLO absorption in RF-sputtered WSe_2 thin-films at 1510 − 1530 nm (near-infrared) spectral using an ultrashort pulse centered at 1520 nm wavelength with an emphasis on the impact of Se-deficiency induced defect states (or bands).

TABLE 3.3: Estimated electronic bandgap for WSe_2 thin-films using Tauc plot.

Sample (nm)	$E_{g1}(eV)$	$E_{g2}(eV)$
130	1.21	–
157	1.21	0.84
242	1.21	1.08
326	1.21	0.89

Impact of film thickness on the nonlinear optical properties

It is well-known that crystalline WSe_2 exhibits indirect electronic bandgap and therefore, the WSe_2 thin films were estimated from the Tauc plot obtained using UV-visible absorption spectrum as shown in Fig.3.4(b). For the convenience, the estimated values are tabulated in Table-3.3. It could be observed that the WSe_2-films thicker than 130 *nm* exhibit two distinct electronic bandgaps which are separated from each other by a defect band. E_{gf} is the intrinsic bandgap for WSe_2 film and E_{gi} is the bandgap originating due to the presence of disorders/defects in the WSe_2 thin-films which is discussed below.

In the NIR spectral region around the communication band (photon energy $\leq$ 0.9 eV), the NLO absorption is expected to exhibit a two-photon absorption (TPA) character. In order to explore this aspect, we measured the OA single-beam Z-scan transmission for obtaining the TPA coefficient (β). The Z-scan experiment used Fourier-transform limited (FTL) ultrashort pulses of temporal width of $\approx$ 140 fs at 1520 *nm* central wavelength. The near-infrared pulses were generated using single-pass optical parametric generation in an periodically-poled $LiNbO_3$ crystal of optimum length [45]. The near-infrared (NIR) pulses were incident on the WSe_2 thin-films at a repetition rate of 514 kHz. The NIR ultrashort pulses were focused onto the thin-films using a lens of focal length 150 *mm* which resulted in a beam waist (w_0) of $\approx$ 60 μm and the Rayleigh length was $\approx$ 7.7 *mm*. All the measurements were carried out at a fixed on-axis peak laser intensity (I_0) of
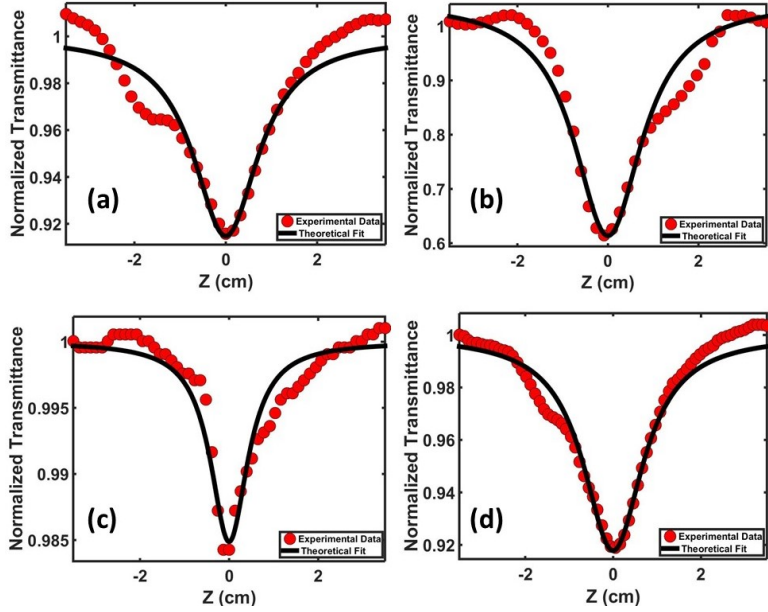
FIGURE 3.10: A representative measured open-aperture Z-scan normalized transmission for WSe_2 thin-films of thickness (a) 130 *nm* (b) 157 *nm* (c) 242 *nm* (d) 326 *nm* for on-axis peak laser intensity of $I_0 = 1.82$ *GW/cm*^{2} (dotted-red curve). The black-solid lines are theoretical fits using Eq. (1).

1.82 *GW/cm*^{2}. Figure 3.10(a)-(d) show the measured OA normalized transmission (dotted curve) for the WSe_2 thin-films having thickness 130 *nm*, 157 *nm*, 242 *nm* and 326 *nm*, respectively. The transmittance curves are characterised by a transmission minima at the focal plane *i.e.* $z = 0$, which is a signature of reverse saturable absorption (RSA). From the electronic bandstructure simulations and linear absorption spectrum, it would be unambiguous to infer that a two-photon absorption (TPA) has a dominant contribution to the RSA characteristics at the 1520 *nm* ($\approx$ 0.8 *eV*) excitation wavelength. This is consistent with fact that an allowed TPA transition in semiconducting thin-film is the one for which the excitation energy of incident laser beam should be less than the energy bandgap (E_g) and greater than $E_g/2$ for the films [30]. The TPA process would cease to exist for excitation photon energy less than $E_g/2$. Therefore, a TPA process could be observed in WSe_2 films when the excitation wavelength is 1520 *nm*. It is also worth noting that the depth

TABLE 3.4: Estimated values of TPA coefficient, imaginary part of $\chi^{(3)}$ and figure of merit (FOM) for all the WSe_2 thin films.

Film thickness (nm)	T_0 (%)	$\alpha \times 10^4$ (cm^{-1})	$I_0 \times 10^9$ (W/cm^2)	$\beta \times 10^{-5}$ (cm/W)	$\chi_{Im}^{(3)} \times 10^{-8}$ (esu)	FOM$\times 10^{-9}$ (esu cm)
130	72.32	2.49	0.31	14.55	26.63	10.7
			0.85	4.37	7.99	3.21
			1.82	1.64	3.06	1.23
			2.78	1.03	1.87	0.75
157	65.34	2.96	0.31	75.27	199.22	67.3
			0.85	25.18	67.83	22.92
			1.82	8.36	24.39	8.24
			2.78	5.98	15.92	5.38
242	65.91	1.72	0.31	3.61	11.41	6.63
			0.85	0.68	0.89	0.52
			1.82	0.29	0.38	0.22
			2.78	0.17	0.21	0.12
326	68.93	1.58	0.31	8.36	8.55	5.41
			0.85	3.26	3.34	2.11
			1.82	1.53	1.56	0.98
			2.78	0.92	0.93	0.59

of normalized transmittance at $z = 0$ in Fig.3.14(a)-(d) is a measure of β *i.e.* a greater β would essentially result in a smaller value of normalized transmittance at $z = 0$ for a fixed I_0. It is apparent from Fig. 3.10(a)-(d) that the WSe_2 film of thickness 157 *nm* exhibits strongest TPA behaviour amongst all the films.

In order to quantitatively estimate β, the measured OA normalized transmittance were fitted using the Eq (2.3), then $\chi_{Im}^{(3)}$ is calculated using Eq. (2.4). The calculated values of β and other related quantities are tabulated in Table 3.4. In order to gain a deeper insight of the variation in β, we carried out the OA Z-scan measurements at different laser intensities. The estimated values of β as a function of WSe_2 film thickness at different laser intensities is shown in Fig. 3.11. All the measurements were made using identical ultrashort pulses centered at 1520 *nm* wavelength and 514 *kHz* repetition rate. In table-3.4, the values of
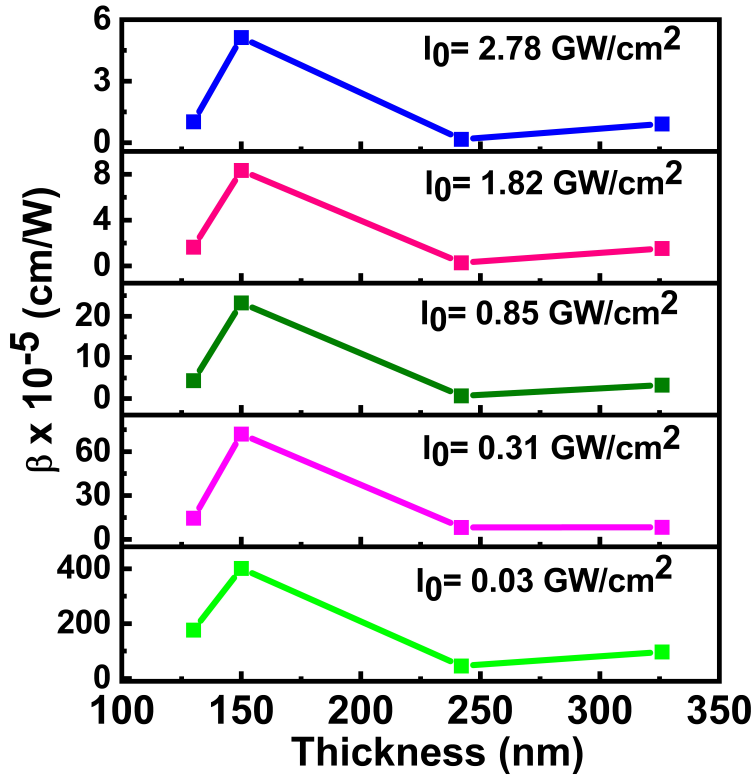
FIGURE 3.11: Variation in TPA coefficient β as a function of WSe_2 thin-film thickness for different on-axis peak laser intensities.

α, β and FOM (for a range of I_0) for all the WSe_2 films has been tabulated. The variation in α for all the WSe_2 films conforms to the variation in *density of defect states* at the excitation wavelength of 1520 nm (or 0.81 eV). It could be ascertained that β (as well as FOM) exhibits an irregular variation with increasing film thickness. From Table-3.4, it is apparent that the TPA coefficient (as well as FOM) maximizes for the 157 nm thick WSe_2 film and β tends to reduce at higher laser intensities for all the films. It is important to note that the TPA coefficient (β) exhibits a dependence on the bandstructure through a relation described by [46],

$$\beta \propto \frac{(N\nu D^4)}{n^2\Gamma} \left[\sum_{i \neq f,g} \frac{(\mu_{gi}^2 \mu_{if}^2)}{(E_{gi} - h\nu)^2} \right] \tag{3.1}$$
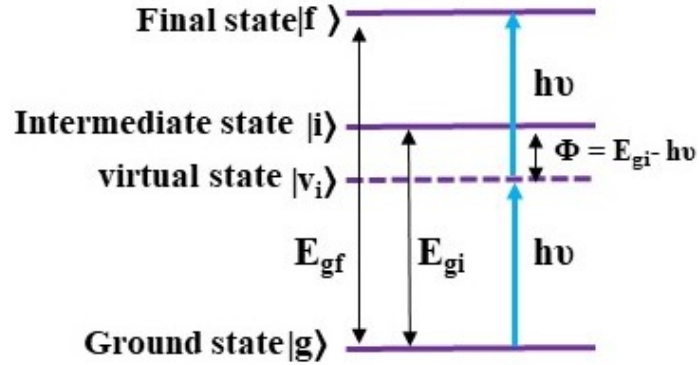
FIGURE 3.12: A schematic representation of energy levels for TPA-allowed transitions.

where ν is the laser frequency, E_{gi} is the energy gap between the ground state ($|g\rangle$) and an intermediate state ($|i\rangle$) (see Fig. 3.12), 2Γ is the full-width at half maximum of the TPA spectrum, D quantifies the enhancement of local optical field density. The factor μ_{gi} in Eq. (3.1) represents the amplitude of oscillating dipole moment induced by the laser electric field resonant with the energy difference between the ground ($|g\rangle$) and intermediate ($|i\rangle$) states. The impact of Eq. (3.1) could be explained through a schematic of energy levels shown in Fig. 3.16 where the incident photon energy $h\nu$ is *out of resonance* for $|g\rangle \rightarrow |i\rangle$ transition or $|i\rangle \rightarrow |f\rangle$ transition. In that case, the transition is achieved through a virtual state ($|v_i\rangle$) which is a superposition state for $|g\rangle$ with $|i\rangle$ or $|f\rangle$. The induced polarization in $|v_i\rangle$ is energy-detuned from the polarization in state $|i\rangle$ by a quantity Φ (= $E_{gi} - h\nu$). A smaller value of Φ, therefore, would essentially enhance β provided the amplitude of dipole oscillations (μ) remain unchanged. From the electronic bandgap estimations (see Table-3.3), the films of thickness 157 *nm*, 242 *nm* and 326 *nm* have an intermediate state $|i\rangle$ significantly below $|f\rangle$ but not resonant to the photon energy ($h\nu$). Quantitatively, $E_g - E_i$ is ≈ 0.84 *eV*, ≈ 1.08 *eV* and ≈ 0.89 *eV* for 157 *nm*, 242 *nm* and 326 *nm* *WSe₂* thin films respectively and accordingly, Φ takes respective values of 0.02 *eV*, 0.26 *eV* and 0.07 *eV* for $h\nu = 0.82$ *eV* (one photon energy). This is elucidated in Fig. 3.13 which shows that the
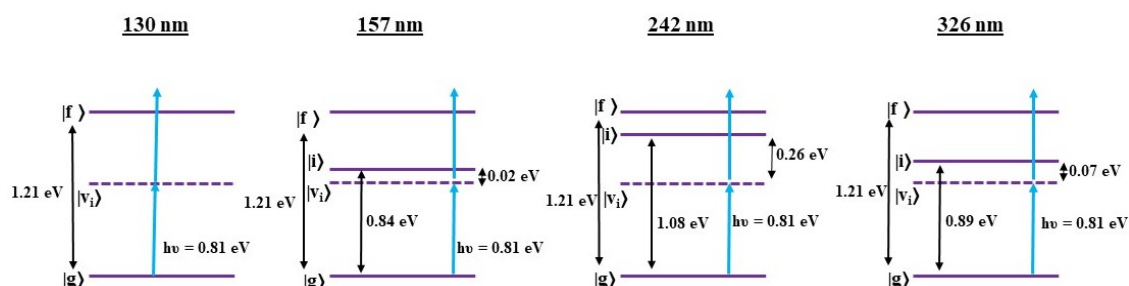
FIGURE 3.13: A schematic representation of the energy level distribution in different WSe_2 thin films. $|g\rangle$: ground-state, $|i\rangle$:intermediate-state, $|f\rangle$: final-state; dashed straight line represents a virtual state ($|v_i\rangle$).

242 *nm* thick WSe_2 film has an intermediate (defect) state that is maximally detuned with respect to one photon energy (0.82 *eV*). On the other hand, the defect state for 157 *nm* thin-film is least detuned from the one photon energy. In all the three situations, Eq. (3.1) depicts that TPA has a dominant contribution to β and the value of β is extremely sensitive to the value of Φ. As a result of this, we obtain the largest value of β for 157 *nm* thick WSe_2 film at all optical intensities (see table-3.4). This is followed by the values of β for 326 *nm* thick WSe_2 films which exhibit $\Phi \approx 0.07$ *eV*. In general, the 242 *nm* thick WSe_2 film exhibits smallest β owing to largest $\Phi \approx 0.26$ *eV*. Although Eq. (3.1) depicts that $\beta \propto \frac{1}{(E_{gi}-h\nu)^2}$, β for 130 *nm* thick WSe_2 film is higher as compared to the 242 *nm* and 326 *nm* thin films. This is in spite of the fact that a defect band or state could not be observed for 130 *nm* thin film. Nevertheless, it could be inferred that a thinner WSe_2 film (except the 130 *nm* film) exhibits a higher density of defect states as compared to the thicker films (of 242 *nm* or 326 *nm* thickness). This manifests as a strong contributor to the estimated value of β for all the films.

Impact of laser intensity on the nonlinear properties

From a design as well as application viewpoint, it is essential to ascertain whether WSe_2 films (due to the presence of defect states or bands) undergoes any alteration in β (or FOM)

when the optical intensity change during the operation. This anticipation is primarily driven by the fact that an optical absorption (linear or nonlinear) process in a semiconductor usually results in generation of 'free' charge-carriers. The excess 'free' charge carriers could modify the absorption by possible transition to higher bands thereby changing the hyperpolarizability. This process is also known as 'free' carrier absorption (FCA) [47]. In order to investigate the role of FCA on laser intensity, we plotted the variation in the estimated values of β for all the WSe_2 thin films as a function of on-axis peak intensity at the focal point (I_0) in Fig. 3.14. All the WSe_2 thin films exhibit a similar trend with maximum value of β at the smallest I_0 and a monotonic decrease as a function of intensity. Such a variation in β as a function of laser intensity (I_0) depicts discernible contribution of 'free-charge carriers' on the nonlinear optical absorption process [48]. At small I_0, the FCA process is efficient and contributes positively to the TPA process which results in a large β. At greater I_0, the higher (excited) band population is significantly large which drives the system into saturation, thereby weakening the impact of FCA. Consequently, this results in a smaller β [34, 42]. In a recent investigation, Kalanoor *et al.* have reported intensity-dependent nonlinear absorption process in perovskite thin-films at ultrashort time-scales that undergo a transition to saturation behaviour from a strong absorption at higher laser intensities which is primarily associated with FCA [47]. A similar investigation by Nagaraja *et al.* have also showed a drop in nonlinear absorption at high laser intensity in *ZnO* thin films which has been attributed to TPA induced free-charge carrier effect [49]. FCA, in general, takes place at low-to-moderate laser intensity levels and consequently, their contribution is usually overshadowed by TPA associated effects at high laser intensities in semiconducting materials [50]. WSe_2, by virtue of being a TMD (a low bandgap semiconductor), provides a conducive platform for observing an enhancement in β owing to a significant impact of FCA.
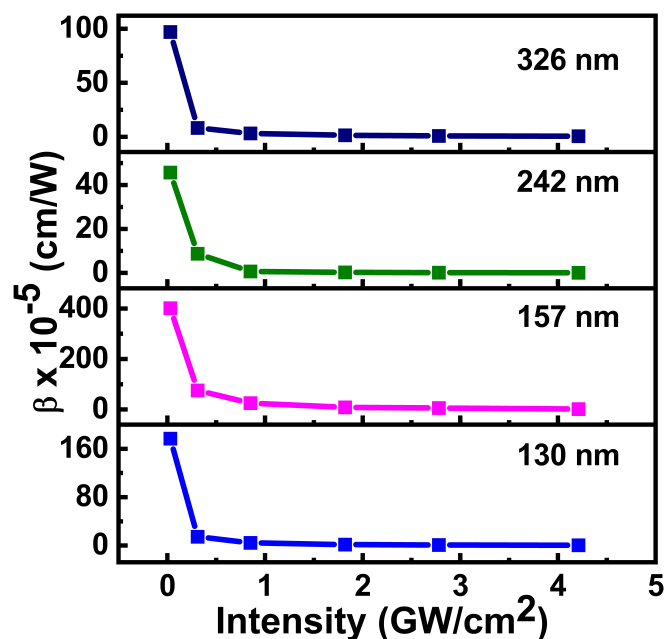
FIGURE 3.14: Variation of TPA coefficient β as a function of on-axis peak laser intensity (I_0).

It is worth noting that the NLO properties of WSe_2 thin films, in addition to pulse-shaping applications in the optical communication band, could be of immense significance in applications such as photodynamic therapy, sensor designing and optical data storage schemes [46]. Due to the fact that the monolithic integration technology as well as semiconductor laser technology in the communication wavelength band is highly matured, the deployment of WSe_2 thin-film based configurations for the aforementioned applications holds tremendous potential. It is apparent that the nonlinear absorption properties of WSe_2 thin films exhibit strong spectral sensitivity. In the near-infrared (NIR) spectral band, WSe_2 films could play a crucial role in optical power limiting applications as a consequence of prominent intensity dependent absorption characteristics. For example, an optimally thick WSe_2 film could be employed as an intensity (or amplitude) modulator in the NIR spectral band and therefore, they are highly promising candidates for developing monolithically-integrated miniaturized high-speed ($\sim GHz$ level) modulators for optical communication.

3.6 Summary

In summary, we investigated the nonlinear optical properties of WSe_2 thin films using single-beam Z-scan technique at 515 nm excitation wavelength. The WSe_2 thin films exhibits a SA behaviour and a self-focusing characteristics at 515 nm excitation wavelength. The magnitude of nonlinear absorption tends to increase for thicker WSe_2 films. The DFT based theoretical modeling provides a plausible route to obtain deeper physical insight into the underlying mechanism for change in the sign of the nonlinear absorption coefficient (β). In addition, the spectral sensitivity of β could be correlated with the electronic bandgap and therefore, it could be tailored by choosing an appropriate film thickness. The WSe_2 thin-films of optimum thickness could, therefore, find applications in realizing devices which require a varying degree of optical modulation during operation. Meanwhile, the nonlinear optical coefficients tend to increase at high repetition rate owing to thermal diffusion effect. However, the RF-sputtered WSe_2 thin films exhibited a TPA behaviour at 1520 nm excitation wavelength which varies with film thickness. It was also observed that the incident laser intensity plays a crucial role in determining the TPA coefficient for the thin films and gets modified owing to discernible contribution of 'free' carrier absorption. The variation in the nonlinear optical absorption characteristics for the WSe_2 films point towards the possibility of bandgap engineering led improvement in functionality of semiconducting thin-film based photonic limiters, sensors and data-storage devices.

Bibliography

[1] Jl A Wilson and AD Yoffe. "The transition metal dichalcogenides discussion and interpretation of the observed optical, electrical and structural properties". *Advances in Physics* 18.73 (1969), pp. 193–335.

[2] Ruben Mas-Balleste et al. "2D materials: to graphene and beyond". *Nanoscale* 3.1 (2011), pp. 20–30.

[3] Qing Hua Wang et al. "Electronics and optoelectronics of two-dimensional transition metal dichalcogenides". *Nature nanotechnology* 7.11 (2012), pp. 699–712.

[4] Sheneve Z Butler et al. "Progress, challenges, and opportunities in two-dimensional materials beyond graphene". *ACS nano* 7.4 (2013), pp. 2898–2926.

[5] Dongzhi Chi, KE Johnson Goh, and Andrew TS Wee. *2D Semiconductor Materials and Devices*. Elsevier, 2019.

[6] D Voß et al. "Atomic and electronic structure of WSe_2 from ab initio theory: Bulk crystal and thin film systems". *Phys. Rev. B* 60.20 (1999), p. 14311.

[7] Won Seok Yun et al. "Thickness and strain effects on electronic structures of transition metal dichalcogenides: $2H\text{-}MX_2$ semiconductors (M= Mo, W; X= S, Se, Te)". *Physical Review B* 85.3 (2012), p. 033305.

[8] Anton Autere et al. "Nonlinear Optics: Nonlinear Optics with 2D Layered Materials (Adv. Mater. 24/2018)". *Adv. Mater.* 30.24 (2018), p. 1870172.

[9] Chunfei Li. *Nonlinear Optics: principles and applications*. Springer, 2016.

[10] Robert W Boyd. *Nonlinear Optics*. Academic press, 2020.

[11] Linnan Jia et al. "Large third-order optical kerr nonlinearity in nanometer-thick $PdSe_2$ 2D dichalcogenide films: implications for nonlinear photonic devices". *ACS Appl. Nano Mater.* 3.7 (2020), pp. 6876–6883.

[12] Bohua Chen et al. "Q-switched fiber laser based on transition metal dichalcogenides MoS_2, $MoSe_2$, WS_2 and WSe_2". *Optics express* 23.20 (2015), pp. 26723–26737.

[13] Dong Mao et al. "WS_2 mode-locked ultrafast fiber laser". *Sci. Rep.* 5.1 (2015), pp. 1–7.

[14] Wenjun Liu et al. "Tungsten diselenide for mode-locked erbium-doped fiber lasers with short pulse duration". *Nanotechnology* 29.17 (2018), p. 174002.

[15] Yabin Shao et al. "Wavelength-dependent nonlinear absorption and ultrafast dynamics process of WS_2". *OSA Continuum* 2.9 (2019), pp. 2755–2763.

[16] Feichi Zhou et al. "2D materials based optoelectronic memory: convergence of electronic memory and optical sensor". *Research* 2019 (2019).

[17]   Kian Ping Loh et al. "Templated deposition of MoS_2 nanotubules using single source precursor and studies of their optical limiting properties". *The Journal of Physical Chemistry B* 110.3 (2006), pp. 1235–1239.

[18]   Charles W Spangler. "Recent development in the design of organic materials for optical power limiting". *Journal of Materials Chemistry* 9.9 (1999), pp. 2013–2020.

[19]   Pankaj R Patel, HS Patel, et al. "Growth, Structural and Electrical Characterization of Tungsten Diselenide crystal". *American Journal of Condensed Matter Physics* 3.1 (2013), pp. 13–20.

[20]   Weijie Zhao et al. "Lattice dynamics in mono-and few-layer sheets of WS_2 and WSe_2". *Nanoscale* 5.20 (2013), pp. 9677–9683.

[21]   Jing-Kai Huang et al. "Large-area synthesis of highly crystalline WSe_2 monolayers and device applications". *ACS nano* 8.1 (2014), pp. 923–930.

[22]   Bilu Liu et al. "Chemical vapor deposition growth of monolayer WSe_2 with tunable device characteristics and growth mechanism study". *ACS nano* 9.6 (2015), pp. 6119–6127.

[23]   Ayrton Sierra-Castillo et al. "Synthesis and Characterization of Highly Crystalline Vertically Aligned WSe_2 Nanosheets". *Applied Sciences* 10.3 (2020), p. 874.

[24]   H Sahin et al. "Anomalous Raman spectra and thickness-dependent electronic properties of WSe_2". *Physical Review B* 87.16 (2013), p. 165409.

[25]   Georg Kresse and Jürgen Furthmüller. "Efficiency of ab-initio total energy calculations for metals and semiconductors using a plane-wave basis set". *Computational materials science* 6.1 (1996), pp. 15–50.

[26]   Peter E Blöchl. "Projector augmented-wave method". *Physical review B* 50.24 (1994), p. 17953.

[27]   John P Perdew, Kieron Burke, and Matthias Ernzerhof. "Generalized gradient approximation made simple". *Physical review letters* 77.18 (1996), p. 3865.

[28]   HJ Monkshort and JD Pack. "Special points for Brillouin-zone integration". *Phys. Rev. B* 13 (1976), pp. 5188–5192.

[29]   Peter E Blöchl, Ove Jepsen, and Ole Krogh Andersen. "Improved tetrahedron method for Brillouin-zone integrations". *Physical Review B* 49.23 (1994), p. 16223.

[30] Eric W Van Stryland et al. "Two photon absorption, nonlinear refraction, and optical limiting in semiconductors". *Optical Engineering* 24.4 (1985), p. 244613.

[31] Jia Guo et al. "Two-dimensional tellurium–polymer membrane for ultrafast photonics". *Nanoscale* 11.13 (2019), pp. 6235–6242.

[32] Nannan Xu et al. "Palladium diselenide as a direct absorption saturable absorber for ultrafast mode-locked operations: from all anomalous dispersion to all normal dispersion". *Nanophotonics* 9.14 (2020), pp. 4295–4306.

[33] Km Surbhi and Ritwick Das. "Impact of Optical Fluence on Pauli Blocking Effect in WSe_2 Thin Film". In: *Photonic Networks and Devices*. Optica Publishing Group. 2022, JW3A–39.

[34] Km Surbhi and Ritwick Das. "Free-carrier assisted optical nonlinearity in WSe_2 thin films near the optical communication band". In: *Laser Science*. Optica Publishing Group. 2022, JW4A–88.

[35] Mauro Falconieri. "Thermo-optical effects in Z-scan measurements using high-repetition-rate lasers". *Journal of Optics A: Pure and Applied Optics* 1.6 (1999), p. 662.

[36] LC Gómez-Pavón et al. "Influence on the saturable absorption of the induced losses by photodeposition of zinc nanoparticles in an optical fiber". *Opt. Express* 26.2 (2018), pp. 1556–1563.

[37] Duanduan Wu et al. "Size effect of WSe_2 on red passively Q-switched fiber laser output performance". *Appl. Opt.* 57.18 (2018), pp. 4955–4959.

[38] Bohua Chen et al. "Tungsten diselenide Q-switched erbium-doped fiber laser". *Opt. Eng.* 55.8 (2016), p. 081306.

[39] Robert I Woodward and Edmund JR Kelleher. "2D saturable absorbers for fibre lasers". *Appl. Sci.* 5.4 (2015), pp. 1440–1456.

[40] Dong Mao et al. "Erbium-doped fiber laser passively mode locked with few-layer WSe_2/$MoSe_2$ nanosheets". *Scientific reports* 6.1 (2016), pp. 1–9.

[41] Jinde Yin et al. "Large-area highly crystalline WSe_2 atomic layers for ultrafast pulsed lasers". *Opt. Express* 25.24 (2017), pp. 30020–30031.

[42]   Km Surbhi et al. "Impact of defects on the $\chi^{(3)}$ optical nonlinearity of sputtered WSe_2 thin films in the optical communication band". *Journal of Applied Physics* 132.24 (2022), p. 243101.

[43]   S Bikorimana et al. "Nonlinear optical responses in two-dimensional transition metal dichalcogenide multilayer: WS_2, WSe_2, MoS_2 and $Mo_{0.5}W_{0.5}S_2$". *Opt. Express* 24.18 (2016), pp. 20685–20695.

[44]   Ningning Dong et al. "Dispersion of nonlinear refractive index in layered WS_2 and WSe_2 semiconductor films induced by two-photon absorption". *Opt. Lett.* 41.17 (2016), pp. 3936–3939.

[45]   Abhishek Mondal and Ritwick Das. "Pump-induced thermo-optic manifestation lead adiabatic ultrashort-pulse optical parametric generation in long LiNbO3 crystals". *Journal of Optics* 23.10 (2021), p. 104002.

[46]   Miłosz Pawlicki et al. "Two-photon absorption and the design of two-photon dyes". *Angewandte Chemie International Edition* 48.18 (2009), pp. 3244–3266.

[47]   Basanth S Kalanoor et al. "Third-order optical nonlinearities in organometallic methylammonium lead iodide perovskite thin films". *Acs Photonics* 3.3 (2016), pp. 361–370.

[48]   R James and D Smith. "Theory of nonlinear optical absorption associated with free carriers in semiconductors". *IEEE Journal of Quantum Electronics* 18.11 (1982), pp. 1841–1864.

[49]   KK Nagaraja et al. "Effect of annealing on the structural and nonlinear optical properties of ZnO thin films under cw regime". *Journal of Physics D: Applied Physics* 46.5 (2013), p. 055106.

[50]   Litty Irimpan et al. "Effect of annealing on the spectral and nonlinear optical characteristics of thin films of nano-ZnO". *Journal of Applied Physics* 104.3 (2008), p. 033118.

Chapter 4

Nonlinear optical response of WSe_2 thin films upon annealing

In this chapter, we have given a systematic study of structural, optical, and NLO properties of WSe_2 thin film grown by RF sputtering system. We employed a Z-scan technique to study the NLO properties such as nonlinear absorption and nonlinear refractive index and to investigate the sources of change in these parameters. Our results also show that thermal annealing at variable temperatures healing the defects which affect the NLO properties of the films. The chapter has been arranged in the following way: the sample preparation and characterization are discussed in section 4.2. This is followed by the measurements of the structural and optical response of the samples which includes the FESEM, EDS, XRD, RAMAN, and linear absorption measurements, given in section 4.3. The nonlinear optical response of the as-prepared and annealed WSe_2 thin films in the NIR spectrum is discussed in section 4.4.

4.1 Introduction

The NLO properties in TMDs could be altered by making changes in the intrinsic bandgap. In this context, TMDs with controllable thickness exhibit desired nonlinear absorption characteristics. Furthermore, the structural and optical properties of thin films are strongly influenced by the post-deposition processes, particularly annealing, since these properties are dependent on the microstructures and interfaces of the films. By the process of thermal annealing, the bandgap could be tailored and consequently, one could control the hyperpolarizability. Thus, it is important to observe the impact of annealing on the NLO properties [1–18].

4.2 Sample preparation and characterization

The WSe_2 thin films were prepared using RF magnetron sputtering system which contained 99.9% pure WSe_2 and films were sputtered at room temperature on a glass substrate of $1\ cm \times 1\ cm$ dimension. Prior to the deposition, the vacuum chamber was evacuated by a turbo molecular pump to a pressure of $3.1\times\ 10^{-6}\ mbar$. Throughout the deposition process, the argon gas pressure was maintained at 15 $sccm$ and the power was fixed at 60 W. The deposition was performed at pressure of 1×10^{-2} mbar. Post deposition, all the samples were annealed at different temperatures and duration in the presence of argon gas at a rate of 100 $sccm$. All the WSe_2 thin-films were $\approx 30\ nm$ thick. We categorized the thin-film properties based on the annealing temperature and duration of annealing. One set (containing three different films) of WSe_2 films were annealed for 15 minutes at three different temperatures as $200°C$, $400°C$ and $600°C$. In a separate set which contained four different WSe_2 thin films, we annealed them at $600°C$ for 15 minutes, 30 minutes, 45 minutes and 60 minutes respectively. The surface morphology and the elemental mapping

of as-prepared and annealed films were carried out using a field-emission scanning electron microscopy (FESEM, ZEISS Sigma, Germany) and energy dispersive X-Ray spectroscopy (EDS) respectively. The crystal structure and the phase identification was carried out through X-ray diffraction spectrum which is obtained using a X-ray diffractometer (Rigaku Smartlab) (λ = 1.5406 Å). The vibrational character for all the films were carried out using a Raman spectrometer (Jobin Yvon LabRam HR Evolution, Horiba) which uses a excitation laser emitting at 532 *nm* wavelength. The linear absorption spectrum of the WSe_2 films were measured using a absorption spectrophotometer (Cary 5000 UV-Vis-NIR, Agilent, India).

4.3 Impact of thermal annealing on the structural and optical properties of WSe_2 thin films

The surface morphology of thermally annealed WSe_2 thin films was explored using FESEM which is shown in Fig.4.1(a)-(f). Figures 4.1(a-c) shows the top-view FESEM images correspond to the films which are annealed at 200°C, 400°C, and 600°C for a fixed duration of 15 minutes. It is apparent that the thermal dewetting of WSe_2 films takes place when the annealing temperature increase which is essentially due to an enhancement in surface energy at higher temperature. It is also worth noting that there is an incommensurate enhancement of surface energy of the film in comparison with the increase in the surface energy of the substrate which manifests in agglomeration [19]. This is discernible through the clusters formed in the image shown in Fig.4.1(c). The WSe_2 thin-film which was annealed at 600°C for 15 minutes, was further annealed for longer duration. This was performed for ascertaining the changes in structural, optical (linear) as well as nonlinear optical properties in the WSe_2 films. At a fixed annealing temperature of 600°C, Figs.4.1(c)-(f) represents the
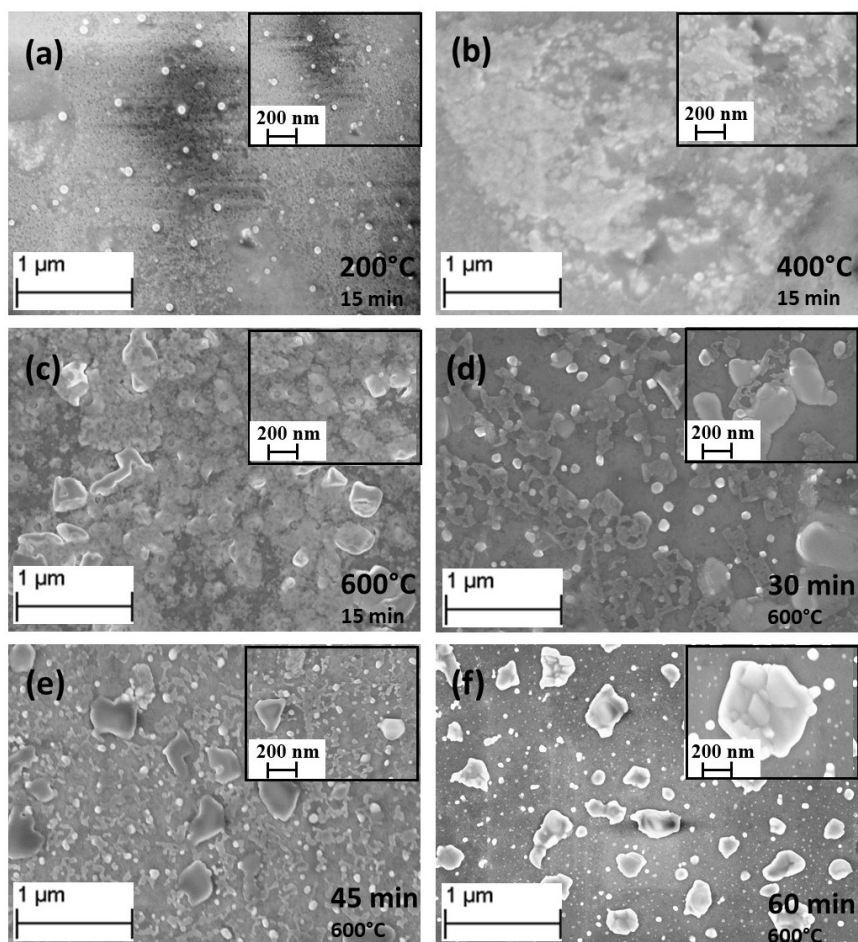
FIGURE 4.1: Field Emission Scanning Electron Microscopy. (a-f) shows top view images of annealed *WSe₂* samples at, 1(a)-(c) 200°C, 400°C, and 600°C at fixed duration for 15 min, while, 1(d)-(f) for 30 min, 45 min and 60 min at fixed temperature 600°C respectively.

FESEM images of films annealed for 15 minutes, 30 minutes, 45 minutes and 60 minutes respectively. The increase in the phenomenon of agglomeration is apparent in these images and the WSe_2 film develops distorted hexagonal islands as a consequence of this (see Fig. 4.1(f)). In order to confirm the presence of WSe_2 in the hexagonal formation, the EDX mapping of the film which is annealed at 600°C for 60 minutes is shown in Fig. 4.2(a)-(c). The distribution of W and Se within the hexagonal unit (Fig. 4.2(a)) could be observed in Fig.4.2(b) and (c) respectively. The study of crystal structure, crystallite sizes, strain,
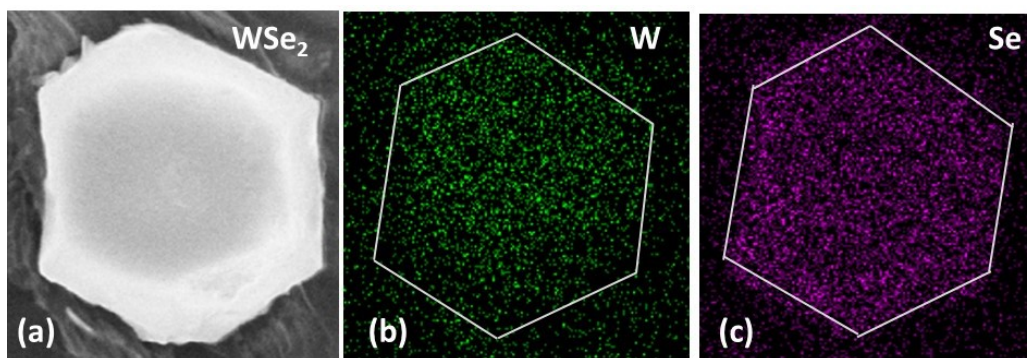
FIGURE 4.2: EDX pattern of WSe_2 sample annealed at 600°C for 60 min.

dislocation density and quantitative phase analysis is carried out using X-ray diffraction (XRD) spectrum of the as-prepared and annealed WSe_2 thin films. The XRD peaks for the as-prepared and annealed films are presented in Fig.4.3(a). The measured XRD peaks of WSe_2 films match reasonably well with JCPDS data card number 87-2418. One peak was consistently obtained at an angle 27.5° which is a consequence of (004) plane in WSe_2. The crystallite sizes were estimated through the Debye-Scherrer relation which are tabulated in Table-4.1. It is observed that the crystallite size increases with increase in annealing duration. The crystallite size for as-prepared WSe_2 film is $\approx$ 40 *nm* and increases from 45 *nm* to 51 *nm* for annealed films. The crystallite size increase could be attributed to the thermal expansion. The strain induced in the as-prepared thin-films and their dislocation density could be estimated from this information which could be found in our previous work [20]. Using an identical recipe, we present the variation of strain and dislocation density as a function of annealing duration in Fig. 4.3(b). The strain tends to reduce for longer annealing duration. In order to appreciate this point, we note that the presence of defects manifests in the form of small crystallites and more number of grain boundaries. As discussed above, thermal annealing for longer duration increases the crystallite size, thereby reducing the number of grain boundaries and defects. The drop in the value of
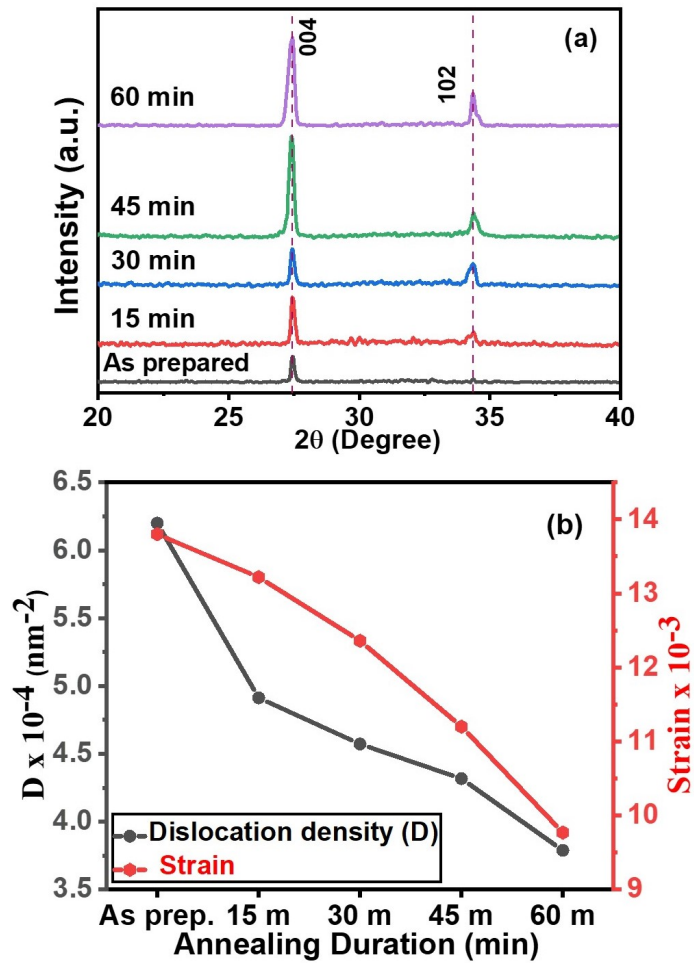
FIGURE 4.3: XRD pattern of as-prepared and annealed WSe_2 samples for fixed temperature at 600°C with variable duration.

strain is a natural consequence of this effect. From a similar argument, the dislocation density also exhibits a drop for longer annealing duration which could also be attributed to the relaxation of stress.

Raman spectroscopy was employed to determine the vibrational modes of the as-prepared and annealed WSe_2 thin films. The excitation wavelength is chosen to be 532 nm. Figure 4.4(a) shows the Raman spectrum for all the films. It could be observed that the as-prepared thin-film contain three characteristic vibrational normal modes. E_{2g}^1 mode pertains to in-

TABLE 4.1: Crystallite sizes and calculated bandgap from Tauc plot of as-prepared and annealed WSe_2 samples.

Annealing duration	Crystallite size (nm)	Bandgap (eV)
As prepared	40.14	1.32
15 min	45.12	1.30
30 min	46.77	1.28
45 min	48.13	1.27
60 min	51.38	1.24

plane vibration of W and Se atoms, A_{1g} is associated with out-of-plane vibration of Se atoms while the B_{2g}^1 mode is out-of-plane vibration of W and Se atoms [20–25]. Interestingly, all the annealed thin-films exhibit only two vibrational normal modes *e.g.* E_{2g}^1 and B_{2g}^1 as shown in Fig. 4.4(a). In other words, the normal mode A_{1g} get suppressed as a result of film annealing. In general, a strong presence of A_{1g} mode is a signature of strain in the films. Therefore, its absence signifies a reduction in strain which is brought about by the process of annealing. In addition, the variation of E_{2g}^1 and B_{2g}^1 modes with annealing duration is shown in Fig. 4.4(b). It is worth noting that the E_{2g}^1 mode is shifting slightly towards right, while, B_{2g}^1 mode is shifting slightly towards left with increase in the duration. The reason behind change in Stokes shift is usually attributed to polarizability change which could possibly result in hyperpolarizability that would have a direct impact on the nonlinear optical properties of the WSe_2 films.

The recorded linear absorption spectrum of the as-prepared and annealed WSe_2 films are shown in Fig. 4.5. It could be observed that all the films exhibit a similar variation with a monotonic drop in absorbance at longer wavelengths. In addition, the electronic bandgap of films were apparently indirect and was estimated from the Tauc plot [20, 26, 27]. The inset in Fig. 4.5 demonstrates the estimation of electronic bandgap for the as-prepared WSe_2 film. The calculated bandgap values for as-prepared and annealed samples are tabulated in Table-1. It could be noted from the table that the bandgap of as-prepared sample is
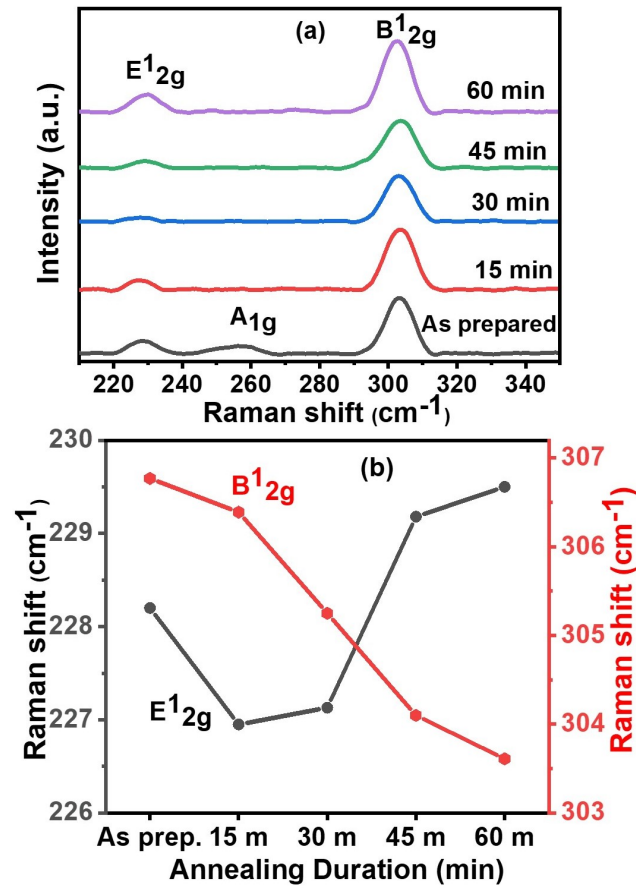
FIGURE 4.4: Raman spectrum of as-prepared and annealed WSe_2 samples with variable duration keeping the temperature fixed at 600°C.

maximum. In other words, the bandgap tends to decrease as a function of annealing duration. From a structural viewpoint, WSe_2 being a semiconductor, the bandgap tends to decrease for a bigger crystallite. When the WSe_2 films are annealed for longer duration, the crystallite size, in general, increases as a consequence of strain relaxation taking place due to excess thermal energy in the WSe_2 matrix. The reduction in electronic bandgap is usually accompanied by a stronger nonlinear optical response which is essentially a manifestation of stronger hyperpolarizability in the medium.
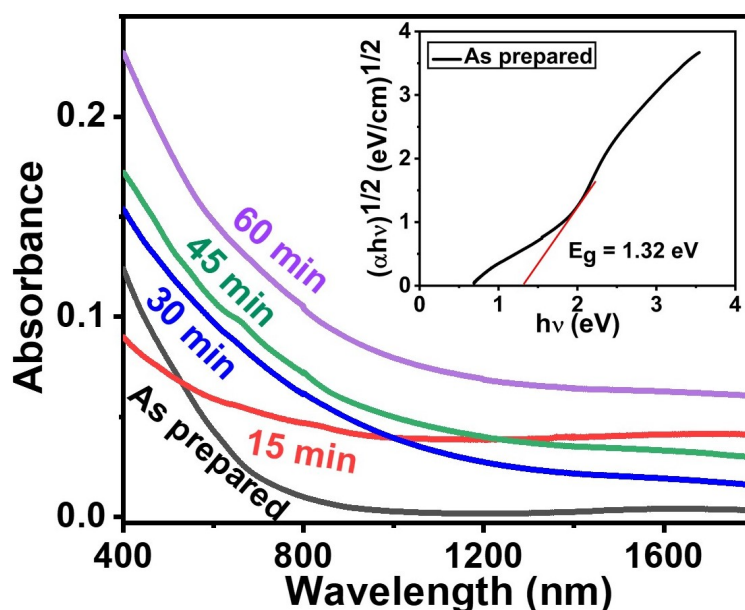
FIGURE 4.5: Uv- vis spectrum of as-prepared and annealed WSe_2 samples for fixed temperature at 600°C with variable duration. The inset shows the calculated bandgap from Tauc plot for as-prepared WSe_2 sample.

4.4 Nonlinear optical properties of annealed WSe_2 films

The aforementioned spectroscopic measurements provides strong motivation for carrying out the measurements on nonlinear optical properties of the WSe_2 thin-films. The pulsed laser beam is focused to a spot-size of $\approx$ 40 μm using a lens of focal length 150 mm. This results in a Rayleigh length of 4.8 mm which is significantly greater than the WSe_2 film thickness. In order to observe the impact of annealing duration on the nonlinear optical properties, we employed the single-beam Z-scan technique described in *Section.*2.6.1. The nonlinear absorption coefficient (β) and nonlinear refractive index (n_2) were measured simultaneously using the OA and CA configuration respectively [28–32]. Since, WSe_2 films were deposited on glass substrates, we carried out the OA and CA Z-scan measurements on bare glass substrates for identical laser intensities. The values of β and n_2 for the substrate would eventually be subtracted from the estimated values corresponding to coefficients
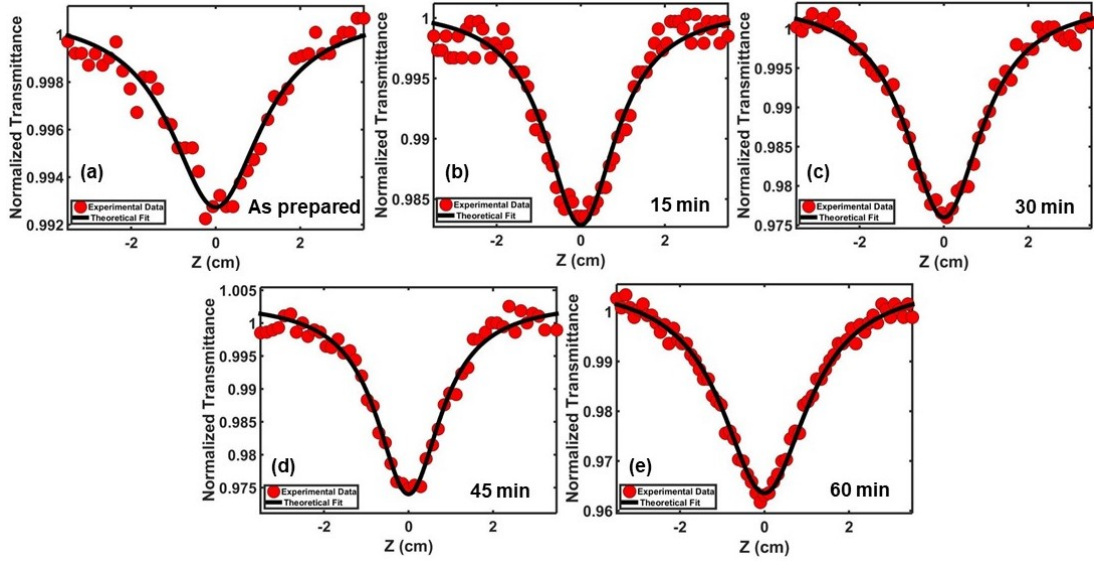
FIGURE 4.6: Open aperture *Z*-scan measurements of annealed WSe_2 samples. (a-e) shows the experimental and theoretical fitting (solid lines) results of as-prepared and annealed WSe_2 samples for fixed temperature at 600°C with variable duration.

for the films. In a general description, the third-order nonlinear susceptibility $\chi^{(3)}$ is a complex quantity (2.6), for which, $\chi_R^{(3)}$ and $\chi_{Im}^{(3)}$ are the real and imaginary components of the complex third-order nonlinear optical susceptibility ($\chi^{(3)}$) which are directly related to n_2 and β respectively [30, 31] The measured OA Z-scan normalized transmittance is plotted as a function of propagation distance (z) in Fig. 4.6(a)-(e) (red dotted curve) for the as-prepared and annealed WSe_2 films of different annealing duration. In all the measurements shown in Fig. 4.6, the on-axis peak intensity at the focal point (I_0) is fixed at 5.06×10^{11} W/cm².

It is worth noting that the laser intensity is small when film is positioned far away from the focal plane. Consequently, the normalized OA transmittance close to unity. When the film translates towards the focal plane, the intensity increases which exemplifies the nonlinear optical response. As a consequence, the normalized OA transmission would exhibit a discernible decrease (valley) or increase (peak) in the transmission near the focal plane.

TABLE 4.2: Nonlinear absorption and nonlinear refraction coefficients of the as-prepared and annealed WSe_2 samples at 1030 nm excitation wavelength.

Annealing duration	$\alpha \times 10^4$ (cm^{-1})	$\beta \times 10^{-8}$ (cm/W)	$n_2 \times 10^{-12}$ (cm^2/W)	$\chi_{Im}^{(3)} \times 10^{-11}$ (esu)	$\chi_R^{(3)} \times 10^{-14}$ (esu)	$FOM \times 10^{-16}$ (esu cm)
As prepared	10.03	1.55	1.17	1.44	8.40	1.44
15 min	8.21	3.77	1.62	3.49	11.64	4.25
30 min	6.60	5.06	3.89	4.69	27.89	7.11
45 min	5.29	5.72	5.18	5.30	37.18	10.03
60 min	3.39	8.42	5.59	7.80	40.22	23.02

The peak at the focal plane is a signature of saturable absorption (SA) behaviour and results in a negative value of β. On the other hand, the valley is the signature of reverse saturable absorption (RSA) behaviour corresponding to the positive value of β [10, 33–37]. The OA normalized transmittance shown in Fig.4.6(a)-(e) exhibit RSA signature for the WSe_2 thin films. It is apparent that the drop in normalized transmittance (see Fig.4.6(a)-(e)) tends to increase for films which have been annealed for longer duration. In order to get a deeper insight, we note that the condition for observing a two-photon absorption (TPA) process or a RSA process in a semiconductor is that the excitation photon energy should be less than the bandgap (E_g) and greater than $\frac{E_g}{2}$. The TPA process ceases to exist when the excitation energy is less than $\frac{E_g}{2}$ [38–40]. For a laser pulse centered at 1030 nm wavelength, the WSe_2 films should exhibit a TPA signature which is observed in Fig. 4.6 in accordance with the bandgap estimated in Table-4.1. The estimated values of β for as-prepared and annealed WSe_2 films are tabulated in Table-4.2 which depicts a monotonic increase in the value of β. In this work, β was found to be 1.55×10^{-8} cm/W for the as-prepared WSe_2 film and 8.42×10^8 cm/W for the film which has been annealed for longest duration (60 minutes). It is apparent that the estimated value of β increases by $\approx$ 5 times when the film is annealed for an hour duration. The development of modern optical technology requires the ability to control and manipulate the intensity of light. In this context, the optical
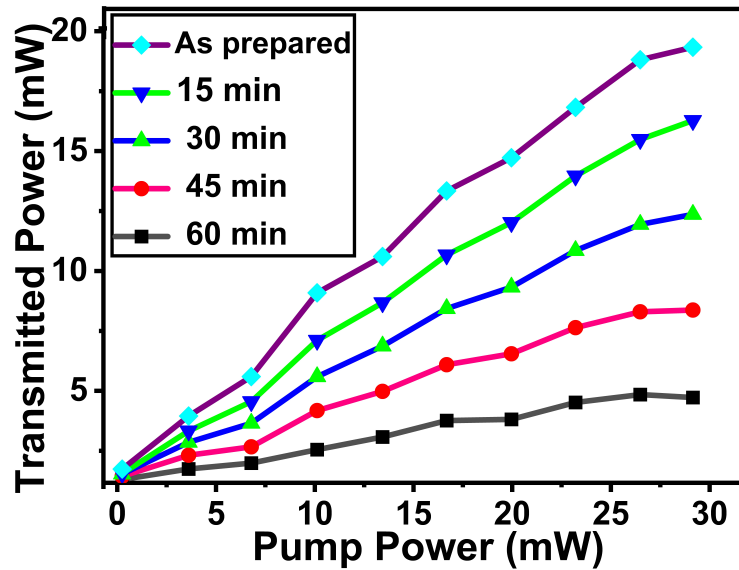
FIGURE 4.7: Optical limiting response of the WSe_2 samples.

power limiters provide a viable route to dynamically control the absorption of light. It is interesting to note that the absorption dynamics is controlled by the light itself. Optical materials with large optical nonlinearity spread over broad spectral range and exhibit high thermal and mechanical stability, are ideal candidates to serve as a good optical limiter. From the OA Z-scan measurements, it is apparent that WSe_2 films could be employed as an efficient optical power limiter in the near-infrared (NIR) spectral band. In order to explore this aspect, we measured the transmittance of WSe_2 thin films as a function of pump laser power (average) when they are placed at the focal plane of the laser beam. The transmitted power, in this case, was recorded without an aperture. It is worth pointing out that the pump laser characteristics were identical to used for OA Z-scan experiment. Fig. 4.7 shows the measured throughput power as a function of incident laser power where it is apparent that the films which have been annealed for a longer duration absorbs more and therefore, acts as more efficient limiter. In other words, the process of annealing improves the optical limiting characteristics of the WSe_2 films. A considerable drop is
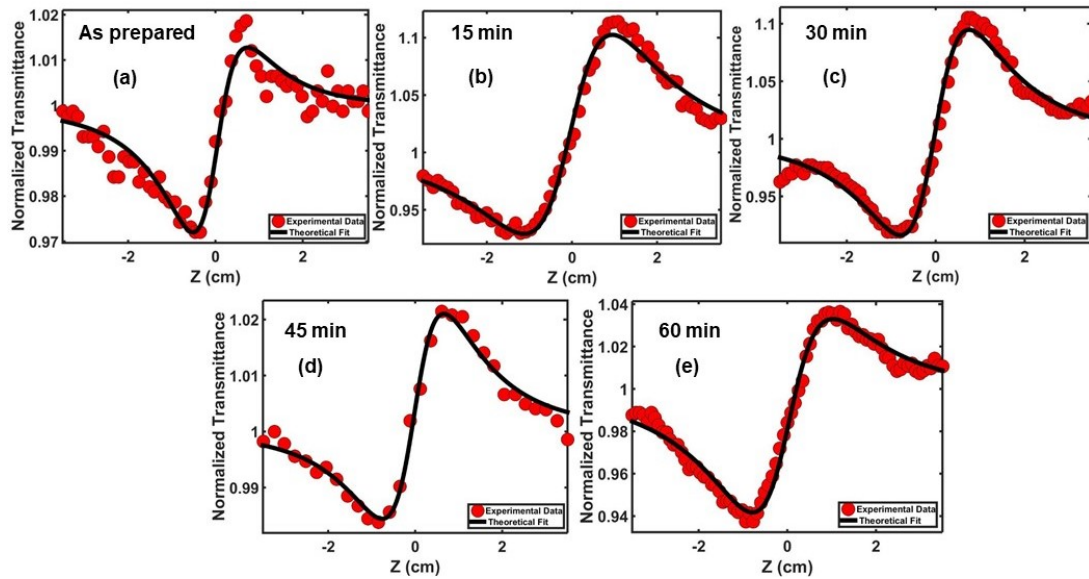
FIGURE 4.8: (a-e) shows closed aperture Z-scan normalized transmittance results of as-prepared and annealed WSe_2 samples for fixed temperature at 600°C with variable duration.

observed in the transmitted power which reveals that the increase in crystallite dimensions and annealing duration has a significant effect on optical power limiting. The optical power limiting studies reveal that with large particle size, better nonlinear absorption occurs and hence, it is considered as a good optical limiter. Thus, the annealed samples are important from the application viewpoint.

In order to determine the sign and magnitude of the nonlinear refractive index, closed aperture (CA) Z-scan measurements were carried out. The measured CA normalized transmittance for as-prepared and annealed WSe_2 thin films using 370 fs pulses center at 1030 nm wavelength is shown in Figs. 4.8(a)-(e) (red dots). The presence of an aperture before the detection of light beam makes this process highly sensitive and therefore, the measurement of n_2 through this technique, could be impacted by higher-order optical nonlinearities, thermo-optic effects, sample inhomogeneity etc. In general, the CA Z-scan measurement is impacted by the nonlinear absorption and consequently, the estimation of
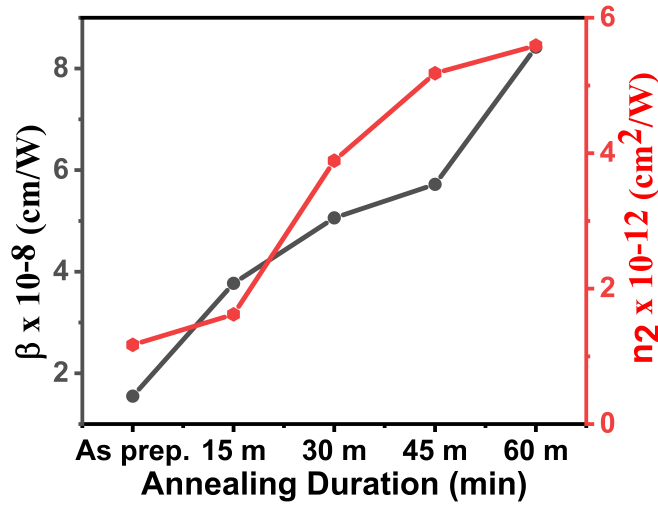
FIGURE 4.9: Variation of β and n_2 as a function of annealing duration.

nonlinear refractive index is derived after removing the contribution of nonlinear absorption obtained through OA Z-scan measurement. The CA normalized transmittance for all WSe_2 thin films exhibit a pre-focal minima followed by a post-focal maxima which is a distinct signature of positive n_2 [10]. The measured normalized CA transmittance was fitted using the relation given by [20]. The solid black curves in Figs. 4.8(a)-(e) are the theoretical fitting to the experimental measurements corresponding to as-prepared and annealed WSe_2 films. The estimated values of n_2 are also tabulated in Table-4.2 for an on-axis peak laser intensity at the focus $I_0 \approx 5 \times 10^{11} \ W/cm^2$. The n_2 was found to be $1.17 \times 10^{-12} \ cm^2/W$ for as-prepared thin-films and $\approx 5.6 \times 10^{12} \ cm^2/W$ for the WSe_2 film annealed for 60 minutes. It is apparent from Table-4.2 that n_2 follows a similar trend as that observed in case of β. In this case, n_2 for annealed film increases up to $\approx$ 4.8 times than that for the as-prepared film. These results provide a basis to argue that the process of annealing has a discernible impact on the NLO response of the WSe_2 films. It is, therefore, interesting to explore the impact of 'duration' of annealing the films on NLO properties, namely β and n_2. The variation of β and n_2 for the WSe_2 film as a function of the annealing duration is presented in Fig. 4.9

at a fixed annealing temperature of $600°C$. The variation distinctly depicts a monotonic increase in the values of β as well as n_2 when the WSe_2 film is annealed for a longer duration. This is primarily manifestation of the fact that the grain size (for the WSe_2 film) increases when the processing of annealing is carried out for longer duration. Therefore, an overall increase in crystallite size in the WSe_2 film results in a stronger third-order NLO response. In order to confirm this assertion, we determined the grain size of the as-prepared thin-film and the WSe_2 films annealed for different duration using the X-ray diffraction spectrum. The estimation of grain size reveals that it increases from ≈ 40.2 nm (for as-prepared film) to ≈ 51.4 nm (for film annealed for 60 min at $600°C$). It is worthwhile to note that the defects associated with the thin films are in the form of small crystallite sizes and more number of grain boundaries. These grain boundaries are responsible for producing strain in the films which has an adverse impact on macroscopic (average) hyperpolarizability. From the grain size estimation for the as-prepared and annealed WSe_2 films, it could be confirmed that the thermal annealing of films for a longer duration increases the crystallite size and reduce the grain boundaries. This relaxes the strain in the film via healing of defects at the grain boundaries which a favourable impact on NLO response from the films.

In order to elucidate a comparative insight, we have tabulated previously reported values of β and n_2 in Table-III for WSe_2 films of varying thicknesses. An overwhelming fraction of the existing literature depicts that WSe_2 thin films exhibit a TPA behaviour at NIR excitation wavelengths of 1040 nm and 1064 nm. The estimated values of n_2 and β are reasonably consistent with the previously reported values for WSe_2 films mentioned in Table-4.3. It is worthwhile to note that the present measurements were carried out at 1030 nm excitation wavelength and at an appreciably high on-axis peak laser intensity (> 30 GW/cm^2) which gives rise to the possibility of very high free-carrier density induced effects. This manifests through smaller values of n_2 and β by an order one or two of magnitude which could be

TABLE 4.3: A comparison depicting the values of β and n_2 for WSe_2 samples using various excitation sources with regard to previous reports and the present study. d:film thickness, $\Delta\tau$:pulse width

d/annealing duration	$\beta(cm/W)$	$n_2(cm^2/W)$	Wavelength and $\Delta\tau$	References
10 nm	7.29×10^{-6}	-1.6×10^{-10}	1064 *nm*, 25 *ps*	[4]
22 μm	1.9×10^{-9}	-2.47×10^{-9}	1064 *nm*, 25 *ps*	[5]
25.1 nm	2.14×10^{-6}	-1.71×10^{-11}	1040 *nm*, 340 *fs*	[6]
As prepared	1.55×10^{-8}	1.17×10^{-12}	1030 *nm*, 370 *fs*	This work
15 min	3.77×10^{-8}	1.62×10^{-12}	1030 *nm*, 370 *fs*	This work
30 min	5.06×10^{-8}	3.89×10^{-12}	1030 *nm*, 370 *fs*	This work
45 min	5.72×10^{-8}	5.18×10^{-12}	1030 *nm*, 370 *fs*	This work
60 min	8.42×10^{-8}	5.59×10^{-12}	1030 *nm*, 370 *fs*	This work

observed in Table-4.3.

4.5 Summary

In summary, we have investigated the nonlinear optical properties of as-prepared and annealed WSe_2 thin-films using Z-scan technique. The measurements were carried out using a ultrashort pulsed fiber laser delivering 370 *fs* pulses centered at 1030 *nm* excitation wavelength at a pulse repetition rate of 1 *kHz*. All the WSe_2 thin films exhibit a TPA behaviour with positive β value and a self-focusing characteristics with positive n_2. The annealed thin films exhibit improved optical limiting characteristics (higher β) owing to enhancement in crystallite sizes and reduction in defect sites. The impact of 'duration' of annealing as well as annealing 'temperature' has been discussed with an emphasis on comprehending the underlying mechanism through which these factors are affecting the NLO response.

Bibliography

[1]   Jl A Wilson and AD Yoffe. "The transition metal dichalcogenides discussion and interpretation of the observed optical, electrical and structural properties". *Advances in Physics* 18.73 (1969), pp. 193–335.

[2]   Ruben Mas-Balleste et al. "2D materials: to graphene and beyond". *Nanoscale* 3.1 (2011), pp. 20–30.

[3]   Qing Hua Wang et al. "Electronics and optoelectronics of two-dimensional transition metal dichalcogenides". *Nature nanotechnology* 7.11 (2012), pp. 699–712.

[4]   Sheneve Z Butler et al. "Progress, challenges, and opportunities in two-dimensional materials beyond graphene". *ACS nano* 7.4 (2013), pp. 2898–2926.

[5]   Dongzhi Chi, KE Johnson Goh, and Andrew TS Wee. *2D Semiconductor Materials and Devices*. Elsevier, 2019.

[6]   D Voß et al. "Atomic and electronic structure of WSe_2 from ab initio theory: Bulk crystal and thin film systems". *Phys. Rev. B* 60.20 (1999), p. 14311.

[7]   Won Seok Yun et al. "Thickness and strain effects on electronic structures of transition metal dichalcogenides: $2H-MX_2$ semiconductors (M= Mo, W; X= S, Se, Te)". *Physical Review B* 85.3 (2012), p. 033305.

[8]   Anton Autere et al. "Nonlinear Optics: Nonlinear Optics with 2D Layered Materials (Adv. Mater. 24/2018)". *Adv. Mater.* 30.24 (2018), p. 1870172.

[9]   Chunfei Li. *Nonlinear Optics: principles and applications*. Springer, 2016.

[10] Robert W Boyd. *Nonlinear Optics*. Academic press, 2020.

[11] Linnan Jia et al. "Large third-order optical kerr nonlinearity in nanometer-thick $PdSe_2$ 2D dichalcogenide films: implications for nonlinear photonic devices". *ACS Appl. Nano Mater.* 3.7 (2020), pp. 6876–6883.

[12] Bohua Chen et al. "Q-switched fiber laser based on transition metal dichalcogenides MoS_2, $MoSe_2$, WS_2 and WSe_2". *Optics express* 23.20 (2015), pp. 26723–26737.

[13] Dong Mao et al. "WS_2 mode-locked ultrafast fiber laser". *Sci. Rep.* 5.1 (2015), pp. 1–7.

[14]   Wenjun Liu et al. "Tungsten diselenide for mode-locked erbium-doped fiber lasers with short pulse duration". *Nanotechnology* 29.17 (2018), p. 174002.

[15]   Yabin Shao et al. "Wavelength-dependent nonlinear absorption and ultrafast dynamics process of WS$_2$". *OSA Continuum* 2.9 (2019), pp. 2755–2763.

[16]   Feichi Zhou et al. "2D materials based optoelectronic memory: convergence of electronic memory and optical sensor". *Research* 2019 (2019).

[17]   Kian Ping Loh et al. "Templated deposition of MoS$_2$ nanotubules using single source precursor and studies of their optical limiting properties". *The Journal of Physical Chemistry B* 110.3 (2006), pp. 1235–1239.

[18]   Charles W Spangler. "Recent development in the design of organic materials for optical power limiting". *Journal of Materials Chemistry* 9.9 (1999), pp. 2013–2020.

[19]   Youngjae Lee et al. "Lithography-free fabrication of large area subwavelength antireflection structures using thermally dewetted Pt/Pd alloy etch mask". *Nanoscale research letters* 4.4 (2009), pp. 364–370.

[20]   Km. Surbhi et al. "Impact of pauli-blocking effect on optical limiting properties of WSe$_2$ thin films". *Optical Materials* 129 (2022), p. 112479. ISSN: 0925-3467.

[21]   Weijie Zhao et al. "Lattice dynamics in mono-and few-layer sheets of WS$_2$ and WSe$_2$". *Nanoscale* 5.20 (2013), pp. 9677–9683.

[22]   Jing-Kai Huang et al. "Large-area synthesis of highly crystalline WSe$_2$ monolayers and device applications". *ACS nano* 8.1 (2014), pp. 923–930.

[23]   Bilu Liu et al. "Chemical vapor deposition growth of monolayer WSe$_2$ with tunable device characteristics and growth mechanism study". *ACS nano* 9.6 (2015), pp. 6119–6127.

[24]   Ayrton Sierra-Castillo et al. "Synthesis and Characterization of Highly Crystalline Vertically Aligned WSe$_2$ Nanosheets". *Applied Sciences* 10.3 (2020), p. 874.

[25]   H Sahin et al. "Anomalous Raman spectra and thickness-dependent electronic properties of WSe$_2$". *Physical Review B* 87.16 (2013), p. 165409.

[26]   J Tauc, Radu Grigorovici, and Anina Vancu. "Optical properties and electronic structure of amorphous germanium". *physica status solidi (b)* 15.2 (1966), pp. 627–637.

[27] Sehun Seo et al. "Direct in situ growth of centimeter-scale multi-heterojunction MoS$_2$/WS$_2$/WSe$_2$/ thin-film catalyst for photo-electrochemical hydrogen evolution". *Adv. Sci.* 6.13 (2019), p. 1900301.

[28] Mansoor Sheik-Bahae et al. "Sensitive measurement of optical nonlinearities using a single beam". *IEEE journal of quantum electronics* 26.4 (1990), pp. 760–769.

[29] S Bikorimana et al. "Nonlinear optical responses in two-dimensional transition metal dichalcogenide multilayer: WS$_2$, WSe$_2$, MoS$_2$ and Mo$_{0.5}$W$_{0.5}$S$_2$". *Opt. Express* 24.18 (2016), pp. 20685–20695.

[30] Kangpeng Wang et al. "Broadband ultrafast nonlinear absorption and nonlinear refraction of layered molybdenum dichalcogenide semiconductors". *Nanoscale* 6.18 (2014), pp. 10530–10535.

[31] Mansoor Sheik-Bahae, Ali A Said, and Eric W Van Stryland. "High-sensitivity, single-beam n_2 measurements". *Optics letters* 14.17 (1989), pp. 955–957.

[32] Samir Kumar et al. "Phase-dependent ultrafast third-order optical nonlinearities in metallophthalocyanine thin films". *J. Appl. Phys.* 120.12 (2016), p. 123104.

[33] R Sutherland. "Handbook of nonlinear optics Marcel Dekker Inc". *New York* (1996).

[34] Mariacristina Rumi and Joseph W Perry. "Two-photon absorption: an overview of measurements and principles". *Advances in Optics and Photonics* 2.4 (2010), pp. 451–518.

[35] Eric W Van Stryland et al. "Two photon absorption, nonlinear refraction, and optical limiting in semiconductors". *Optical Engineering* 24.4 (1985), p. 244613.

[36] Km Surbhi et al. "Impact of defects on the $\chi^{(3)}$ optical nonlinearity of sputtered *WSe$_2$* thin films in the optical communication band". *Journal of Applied Physics* 132.24 (2022), p. 243101.

[37] Km Surbhi and Ritwick Das. "Free-carrier assisted optical nonlinearity in *WSe$_2$* thin films near the optical communication band". In: *Laser Science*. Optica Publishing Group. 2022, JW4A–88.

[38] KK Nagaraja et al. "Effect of annealing on the structural and nonlinear optical properties of ZnO thin films under cw regime". *Journal of Physics D: Applied Physics* 46.5 (2013), p. 055106.

[39]   Litty Irimpan et al. "Effect of annealing on the spectral and nonlinear optical characteristics of thin films of nano-ZnO". *Journal of Applied Physics* 104.3 (2008), p. 033118.

[40]   Litty Irimpan et al. "Size-dependent enhancement of nonlinear optical properties in nanocolloids of ZnO". *Journal of applied physics* 103.3 (2008), p. 033105.

Chapter 5

Nonlinear optical response in Au nanoparticles induced WSe_2 thin films

In this chapter, we present a study to explore the impact of Au NPs on the nonlinear optical (NLO) characteristics of the WSe_2 thin films and related hybrid architectures. The WSe_2 thin film was prepared using a RF magnetron sputtering system. The characterization of the RF-sputtered WSe_2 thin-film is carried out using field-emission scanning electron microscope (FESEM), Raman spectroscopy and UV-VIS-NIR spectroscopy. The NLO response has been measured using single-beam Z-scan technique with an ultrashort pulsed pump laser centered at 1030 nm wavelength. The contents of the chapter has been presented in the following way: section 5.1 contains the introduction to the localized surface plasmon resonance and thin-film preparation and characterization are discussed in section 5.2. This is followed by the investigation on the nonlinear optical response of the samples in NIR range in section 5.3.

5.1   Introduction

Over the past two decades, plasmon resonances of metal nanoparticles have been a topic of extensive research. Localized surface plasmon resonance (LSPR) is a widely investigated sub-wavelength scale optical phenomenon that occurs when incident light interacts with plasmon-active metal nanoparticles (NPs) whose physical dimensions are less than the wavelength of the incident light [1–4]. When the frequency of the incident light is able to resonantly interact with the oscillation frequency of the conduction electrons of metal NPs, the interaction results in the collective oscillation of the surface electrons as shown in Fig.6.1. Such nanoparticle oscillations resemble could have dipolar as well as quadrupolar contribution which is essentially determined by their size and shape [5–10]. Such resonant light-matter interaction is characterized by sharp absorption lines and high scattering peaks. [1]

The metals such as gold (Au), silver (Ag), copper (Cu), nickel (Ni), and aluminum (Al) are frequently used plasmon-active metals. The optical properties of these metals essentially depend on the complex frequency-dependent dielectric constant that has a predominantly negative real part of dielectric constant in the visible and near-infrared spectral band and consequently, a complex refractive index. The nonlinear optical properties of noble metals and noble metal nanoparticle have been extensively studied [11–29]. From a different perspective, due to the superior physical and chemical properties such as high electrical conductivity, low noise, and large surface volume, two dimensional (2D) materials have been widely used in the development and research of biosensors. 2D material configurations have been used to enhance the sensitivity of SPR sensors as a single metal layer or in bimetallic architectures. However, devise stability and robustness have been critical issues. In particular, 2D transition metal dichalcogenides (TMDCs), such as WS_2, MoS_2,
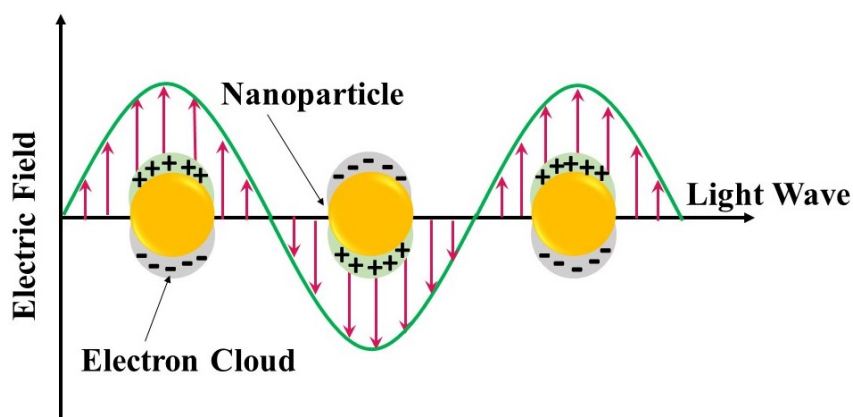
FIGURE 5.1: Schematic of localized surface plasmon resonance (LSPR), in which light incident on the metal nanoparticles and strongly couples to the free conduction electrons, causing them to oscillate.

WSe_2, and $MoSe_2$, have emerged as promising candidates in biocatalysts, biosensors, and biomedical applications [30]. The important effect of LSP is that the electric fields is strongly localized near the surface of the particle and the field drops-off rapidly from the distance. The evanescent tail could be substantially altered by bringing a TMD layer in close proximity or in contact with the metal nanoparticle. The possibility of strong field localization gives rise to a strong NLO response from metal NP-TMD heterostructures which is discussed in detail below.

5.2 Sample preparation and characterization

The sample preparation is explained using schematic diagram in Fig.5.2. The Au film is deposited onto a $1\ cm \times 1\ cm$ glass substrate using electron beam evaporation system. The Au NPs are formed after annealing the Au film at $550°\ C$ for 30 minutes. We have prepared a set of two samples. In the heterostructure sample 1 (S_1), the Au NPs formed on top of the substrate (glass). A WSe_2 thin film of certain thickness was deposited using a
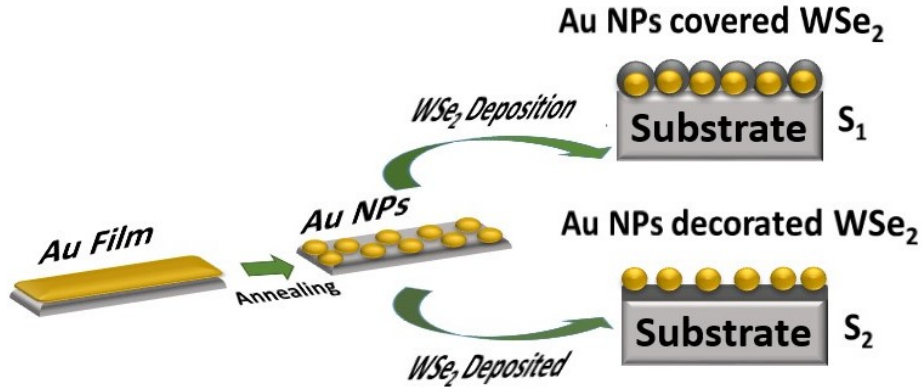
FIGURE 5.2: Schematic diagram of the samples S_1 and S_2. S_1 : Au NPs covered with WSe_2, S_2 : Au NPs decorated WSe_2.

RF magnetron sputtering system with a WSe_2 (99.9% pure) target in an argon environment at room temperature. For the sample2 (S_2), Au NPs are deposited on top of a WSe_2 thin film. The morphological features of the samples are investigated through field-emission scanning electron microscope (FESEM). The Raman spectrum were measured using a Raman spectrometer (Jobin Yvon LabRam HREvolution, Horiba) with an excitation at 532 nm wavelength. The linear absorption spectrum of the WSe_2 thin films were carried out using a UV-VIS-NIR spectrometer (Agilent carry 5000 UV-Vis-NIR).

5.3   Structural and optical properties

The surface morphology of Au NPs in WSe_2 films was explored using FESEM images which are shown in Figs. 5.3(a) and (b). These are top-view FESEM image for heterostructure samples S_1 and S_2 respectively. The spherical sub-wavelength particle formation could be observed from the images. The average particle size was obtained from these images. The calculated average particle size is 67.6 nm and 34.9 nm respectively. Raman spectroscopy was employed to determine the vibrational modes of all the samples. The excitation source
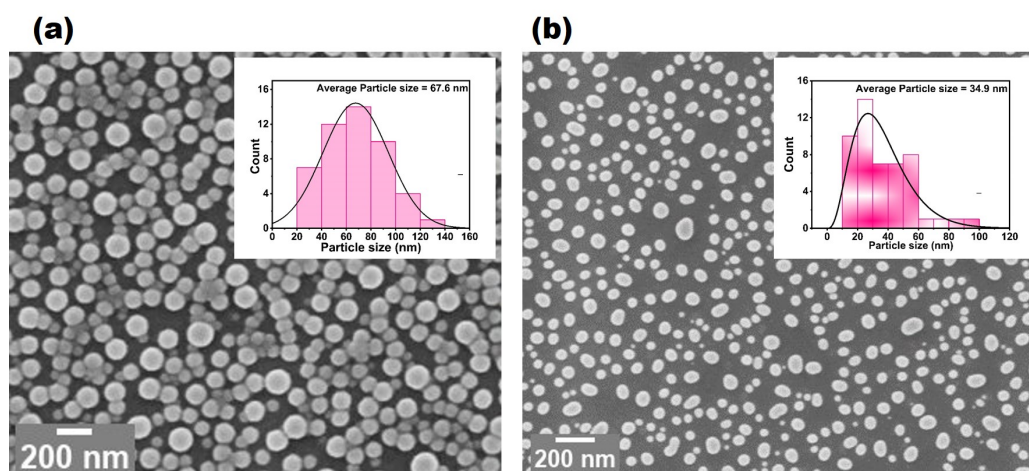
FIGURE 5.3: Field Emission Scanning Electron Microscopy. (a-b) shows top surface images of the samples S_1 and S_2 respectively. Insets show the corresponding size distribution. The average particle size is (a) 67.6 nm. (b) 34.9 nm.

is a laser emitting wavelength of 532 nm. Fig. 5.4 shows the Raman spectrum for all the films. It could be observed that both the heterostructure samples (S_1 and S_2) contain three characteristic vibrational normal modes. E_{2g}^1 mode pertains to in-plane vibration of W and Se atoms, A_{1g} is associated with out-of-plane vibration of Se atoms while the B_{2g}^1 mode is out-of-plane vibration of W and Se atoms [31–36]. It is interesting to note that the presence of Au NPs leads to significant jump in intensity of the peaks. In a previous report, Mukherjee *et al.* [37] have presented a series of experimental results which was corroborated with theoretical analysis for identifying the underlying reasons for intensity enhancement of Raman Stokes peaks. The results elucidated that the increase in intensity is due to the field enhancement in the WSe_2 layer due to the formation of LSP modes in presence of Au nanoparticles. In general, the strength of the Stokes peak is a signature of polarizability enhancement in the sample [37–40]. Therefore, in this case, it could be possible that the hyperpolarizability is significant that would could manifest through NLO investigations of S_1 and S_2.
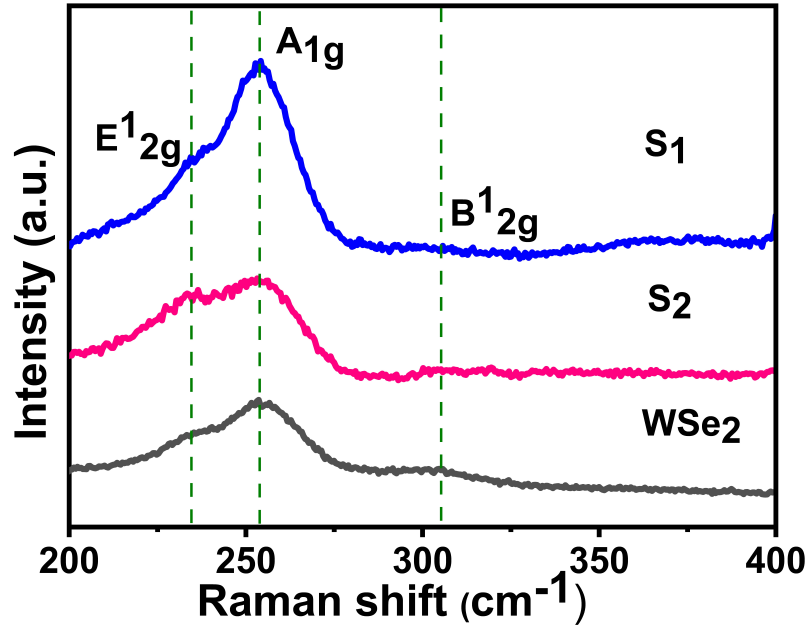
FIGURE 5.4: Raman spectra of the samples.

The linear absorption features were explored by performing UV-VIS-NIR spectroscopy and the results are shown in Fig 5.5. It is found that, in pristine WSe_2 films, the absorption spectrum exhibits an uniform variation as a function of wavelength which was presented previously in this thesis (Chapter-3). However, in presence of AuNPs, the absorption spectra gets modified significantly. There are prominent red-shifted peaks due to LSP mode excitation at the LSPR wavelength. In case of S_1, the LSP mode-excitation peak was more intense than that in case of S_2. Also, the LSPR peak in case of S_1 is more red-shifted as compared to that of S_2. Mehzar *et al.* has reported that the red-shift in LSPR peak wavelength is primarily due to increase in the particle size. Subsequently, we carried detailed measurements to ascertain the nonlinear optical properties of the heterostructure samples and compared with the pristine WSe_2 films.
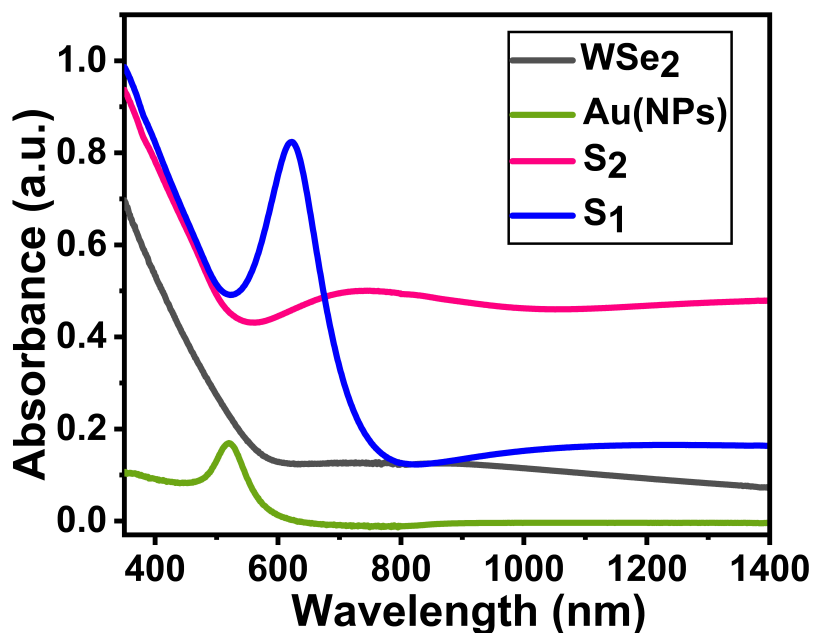
FIGURE 5.5: UV-vis spectra of the samples.

5.4 Nonlinear optical properties

The nonlinear optical absorption measurements of WSe_2 thin-film was carried out through a single-beam Z-scan technique which used a Fourier-transform limited (FTL) ultrashort pulses of temporal width of $\approx$ 370 fs at 1030 nm excitation wavelength. The pulse repetition rate was chosen to be 1 kHz. The measured OA Z-scan transmittance for pristine WSe_2 thin film and the samples S_1 and S_2 are shown in Fig. 5.6(a), (b) and (c) (red-dots) respectively. All the OA Z-scan measurements were carried out at maximum on-axis peak intensity of 2.18×10^{11} W/cm^2. The solid black curves are the theoretical fits for obtaining the value of β which is tabulated in Table-5.1. It is apparent that the WSe_2 thin film exhibits a RSA behaviour whereas the heterostructure samples show saturable absorption (SA) characteristics.

In order to estimate β, the linear absorption coefficient (α) for the as-prepared thin-film, S_1 and S_2 is given by 15.6×10^4 cm^{-1}, 7.0×10^4 cm^{-1} and 17.1×10^4 cm^{-1} respec-
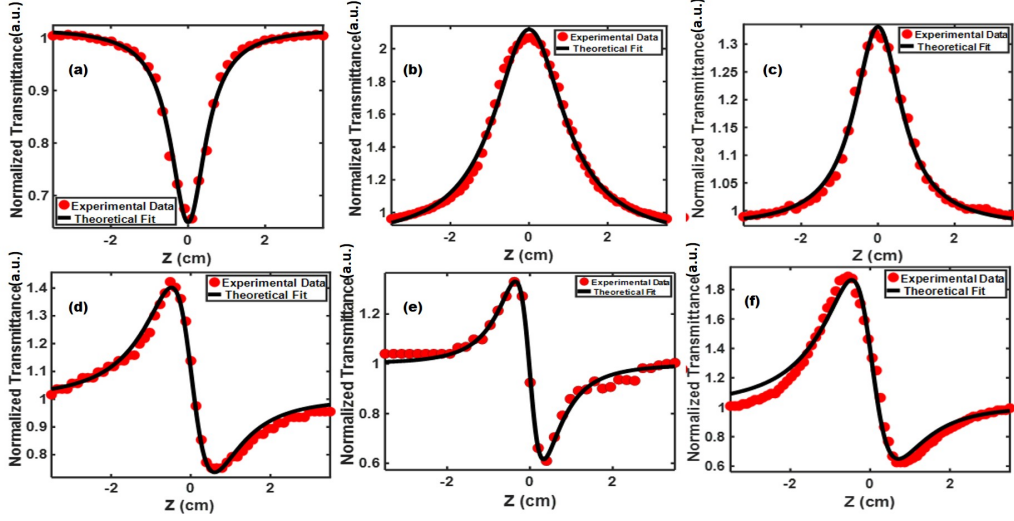
FIGURE 5.6: Open aperture (OA) and closed aperture (CA) Z-scan normalized transmittance for the samples, (a) and (d) WSe_2 thin film, (b) and (e) S_1, (c) and (f) S_2 respectively. Red dots represent the experimentally measured values and black solid curve represent the theoretical fitting (solid lines).

tively. In case of as-prepared thin-film, $\beta \approx 8.1 \times 10^{-7}\ cm/W$ whereas β takes the values $-24.7 \times 10^7\ cm/W$ and $-15.9 \times 10^7\ cm/W$ for samples S_1 and S_2 respectively.

These observations OA Z-scan signatures for S_1 and S_2 at 1030 nm wavelength (photon energy $\approx 1.2\ eV$) are unusual and non-intuitive. This is essentially due to the fact that (i) the SPR wavelength for Au-WSe_2 interface is usually in the visible spectral band ($400 - 700\ nm$) (ii) Au nano-particles exhibit SA signature only in the visible spectral band owing to interband transitions (d-valence band to $s - p$ conduction band) [41, 42] (iii) WSe_2 films (monolayer or multilayer) exhibit TPA signature in the near-infrared spectral band ($\geq\ 1\ \mu m$ wavelength) owing to an intrinsic bandgap of $\sim 1.4\ eV$. All these points essentially direct towards inferring a TPA signature for Au nanoparticles in WSe_2 background at NIR ($\geq\ 1\ \mu m$) wavelength. In order to gain a deeper insight, we note that LSPR mode excitation at 1030 nm wavelength leads to field localization at $Au - WSe_2$ interface. At sufficiently high laser intensity (close to focus $z = 0$ in OA Z-scan set-up), this strong

TABLE 5.1: Nonlinear absorption and nonlinear refraction coefficients of the samples at 1030 nm excitation wavelength.

Sample	$\alpha \times 10^4$ (cm^{-1})	$\beta \times 10^{-7}$ (cm/W)	$n_2 \times 10^{-12}$ (cm^2/W)	$\chi_{Im}^{(3)} \times 10^{-10}$ (esu)	$\chi_R^{(3)} \times 10^{-12}$ (esu)	$FOM \times 10^{-15}$ (esu cm)
WSe_2	15.6	8.14	-21.33	7.54	-1.53	4.83
S_1	7.0	-24.73	-34.91	-22.9	-2.50	32.71
S_2	17.1	-15.92	-25.83	-14.74	-1.86	8.619

field localizations results in generation of 'hot electrons' (in $s - p$ conduction band of Au) [41–43]. Further, these 'hot electrons' (high kinetic energy electrons) densely populate the lower band-edge states of WSe_2 conduction band and the Se-deficiency induced defect states in WSe_2 (see Sec. 3.5). Therefore, the TPA transition probability in WSe_2 is greatly reduced at 1030 nm excitation wavelength which manifests through a discernible SA behaviour in the OA Z-scan measurement. This argument is also justified by the observation that S_2 exhibits a weaker SA behaviour (β is less negative) in comparison with S_1. In case of S_2, the surface-to-surface contact between WSe_2 and Au-film is lesser as compared to that in S_1. Therefore, the injection of hot electrons in WSe_2 is less which manifests through a weaker SA behaviour in OA Z-scan measurement.

The measured CA normalized transmittance for as-prepared WSe_2 film, S_1 and S_2 using 370 fs pulses centered at 1030 nm excitation wavelength is shown in Figs.5.6(d)-(f) (red dots). All the measurements have been carried out at an on-axis peak intensity at the focus $I_0 \approx 2.18 \times 10^{11}$ W/cm^2 and at a pulse repetition rate of 1 kHz. The CA normalized transmittance for all the samples under investigation exhibit a pre-focal maxima followed by a post-focal minima which is a distinct signature of self-defocusing effect [44]. The estimated values of n_2 are tabulated in Table 5.1 where the magnitude of n_2 exhibits a variation in magnitude which is similar to that exhibited by β. S_1 shows strongest defocusing effect owing to strong hyperpolarizability inherited through LSPR excitation at $WSe_2 - Au$ interface.

5.5   Summary

In summary, we have investigated the nonlinear optical properties of as-prepared thin-films and heterostructures comprising Au-nanoparticles in WSe_2 host film using Z-scan technique which used a 370 fs pulses centered at 1030 nm excitation wavelength. The as-prepared WSe_2 film exhibits TPA characteristics and a self-defocusing signature. On the other hand, Au-nanoparticle based heterostructures show SA characteristics in conjunction with self-defocusing behaviour. This investigation provides a method to employed WSe_2 based thin-film architectures for mode-locking near-infrared and mid-infrared lasers.

Bibliography

[1]   Kathryn M Mayer and Jason H Hafner. "Localized surface plasmon resonance sensors". *Chemical reviews* 111.6 (2011), pp. 3828–3857.

[2]   Gustav Mie. "Beiträge zur Optik trüber Medien, speziell kolloidaler Metallösungen". *Annalen der physik* 330.3 (1908), pp. 377–445.

[3]   Lindsey JE Anderson et al. "Quantitative measurements of individual gold nanoparticle scattering cross sections". *The Journal of Physical Chemistry C* 114.25 (2010), pp. 11127–11132.

[4]   Joshua Nall, Liba Taub, and Frances Willmoth. *The Whipple Museum of the History of Science*. Cambridge University Press, 2019.

[5]   Vijender Singh and Praveen Aghamkar. "Surface plasmon enhanced third-order optical nonlinearity of Ag nanocomposite film". *Applied Physics Letters* 104.11 (2014), p. 111112.

[6]   MA Noginov, G Zhu, and VI Gavrilenko. "Sensitized nonlinear emission of gold nanoparticles". *Optics Express* 15.24 (2007), pp. 15648–15655.

[7] James Hsu et al. "Linear and nonlinear optical properties of Ag/Au bilayer thin films". *Optics Express* 20.8 (2012), pp. 8629–8640.

[8] MH Majles Ara et al. "Diffraction patterns and nonlinear optical properties of gold nanoparticles". *Journal of Quantitative Spectroscopy and Radiative Transfer* 113.5 (2012), pp. 366–372.

[9] EC Romani et al. "Gold nanoparticles on the surface of soda-lime glass: morphological, linear and nonlinear optical characterization". *Optics express* 20.5 (2012), pp. 5429–5439.

[10] DPAC Gaspar et al. "Influence of the layer thickness in plasmonic gold nanoparticles produced by thermal evaporation". *Scientific reports* 3.1 (2013), p. 1469.

[11] N Del Fatti and F Vallee. "Ultrafast optical nonlinear properties of metal nanoparticles". *Applied Physics B* 73 (2001), pp. 383–390.

[12] Shiliang Qu et al. "A theoretical and experimental study on optical limiting in platinum nanoparticles". *Optics communications* 203.3-6 (2002), pp. 283–288.

[13] Shiliang Qu et al. "Optical nonlinearities and optical limiting properties in gold nanoparticles protected by ligands". *Chemical physics letters* 356.3-4 (2002), pp. 403–408.

[14] Yachen Gao et al. "Saturable absorption and reverse saturable absorption in platinum nanoparticles". *Optics communications* 251.4-6 (2005), pp. 429–433.

[15] Shiliang Qu et al. "Optical nonlinearities of space selectively precipitated Au nanoparticles inside glasses". *Chemical physics letters* 368.3-4 (2003), pp. 352–358.

[16] Yachen Gao et al. "Size effect of optical limiting in gold nanoparticles". *Chemical Physics* 336.2-3 (2007), pp. 99–102.

[17] Fushen Lu et al. "Fullerene-functionalized gold core–shell nanoparticles: Preparation and optical limiting properties". *Inorganic Chemistry Communications* 7.8 (2004), pp. 960–962.

[18] Reji Philip et al. "Picosecond optical nonlinearity in monolayer-protected gold, silver, and gold-silver alloy nanoclusters". *Physical Review B* 62.19 (2000), p. 13160.

[19] David D Smith et al. "Cancellation of photoinduced absorption in metal nanoparticle composites through a counterintuitive consequence of local field effects". *JOSA B* 14.7 (1997), pp. 1625–1631.

[20] D Ricard, Ph Roussignol, and Chr Flytzanis. "Surface-mediated enhancement of optical phase conjugation in metal colloids". *Optics letters* 10.10 (1985), pp. 511–513.

[21] N Del Fatti et al. "Electron dynamics and surface plasmon resonance nonlinearities in metal nanoparticles". *Chemical Physics* 251.1-3 (2000), pp. 215–226.

[22] F_ Hache et al. "The optical Kerr effect in small metal particles and metal colloids: the case of gold". *Applied Physics A* 47 (1988), pp. 347–357.

[23] K Uchida et al. "Optical nonlinearities of a high concentration of small metal particles dispersed in glass: copper and silver particles". *JOSA B* 11.7 (1994), pp. 1236–1243.

[24] Li Yang et al. "Probing interface properties of nanocomposites by third-order nonlinear optics". *Applied Physics A* 62 (1996), pp. 403–415.

[25] HB Liao et al. "Origin of third-order optical nonlinearity in Au: SiO 2 composite films on femtosecond and picosecond time scales". *Optics letters* 23.5 (1998), pp. 388–390.

[26] HB Liao et al. "Large third-order nonlinear optical susceptibility of Au-Al2O3 composite films near the resonant frequency". *Applied Physics B* 65 (1997), pp. 673–676.

[27] Stephan Link and Mostafa A El-Sayed. *Spectral properties and relaxation dynamics of surface plasmon electronic oscillations in gold and silver nanodots and nanorods.* 1999.

[28] Prashant K Jain et al. "Noble metals on the nanoscale: optical and photothermal properties and some applications in imaging, sensing, biology, and medicine". *Accounts of chemical research* 41.12 (2008), pp. 1578–1586.

[29] Susie Eustis and Mostafa A El-Sayed. "Why gold nanoparticles are more precious than pretty gold: noble metal surface plasmon resonance and its enhancement of the radiative and nonradiative properties of nanocrystals of different shapes". *Chemical society reviews* 35.3 (2006), pp. 209–217.

[30] Santosh Kumar et al. "MoS 2 functionalized multicore fiber probes for selective detection of shigella bacteria based on localized plasmon". *Journal of Lightwave Technology* 39.12 (2021), pp. 4069–4081.

[31] Weijie Zhao et al. "Lattice dynamics in mono-and few-layer sheets of WS$_2$ and WSe$_2$". *Nanoscale* 5.20 (2013), pp. 9677–9683.

[32] Jing-Kai Huang et al. "Large-area synthesis of highly crystalline WSe$_2$ monolayers and device applications". *ACS nano* 8.1 (2014), pp. 923–930.

[33] Bilu Liu et al. "Chemical vapor deposition growth of monolayer WSe$_2$ with tunable device characteristics and growth mechanism study". *ACS nano* 9.6 (2015), pp. 6119–6127.

[34] Ayrton Sierra-Castillo et al. "Synthesis and Characterization of Highly Crystalline Vertically Aligned WSe$_2$ Nanosheets". *Applied Sciences* 10.3 (2020), p. 874.

[35] H Sahin et al. "Anomalous Raman spectra and thickness-dependent electronic properties of WSe$_2$". *Physical Review B* 87.16 (2013), p. 165409.

[36] Km. Surbhi et al. "Impact of pauli-blocking effect on optical limiting properties of WSe$_2$ thin films". *Optical Materials* 129 (2022), p. 112479. ISSN: 0925-3467.

[37] Bablu Mukherjee et al. "Raman analysis of gold on WSe2 single crystal film". *Materials Research Express* 2.6 (2015), p. 065009.

[38] Yumeng Shi et al. "Selective decoration of Au nanoparticles on monolayer MoS2 single crystals". *Scientific reports* 3.1 (2013), p. 1839.

[39] Shao Su et al. "Creating SERS hot spots on MoS2 nanosheets with in situ grown gold nanoparticles". *ACS applied materials & interfaces* 6.21 (2014), pp. 18735–18741.

[40] Chang-Hsiao Chen et al. "Hole mobility enhancement and p-doping in monolayer WSe2 by gold decoration". *2D Materials* 1.3 (2014), p. 034001.

[41] Shiliang Qu et al. "Nanosecond nonlinear absorption in Au and Ag nanoparticles precipitated glasses induced by a femtosecond laser". *Optical Materials* 28.3 (2006), pp. 259–265.

[42] Guang-Hua Fan et al. "Size-dependent nonlinear absorption and refraction of Ag nanoparticles excited by femtosecond lasers". *Chinese Physics B* 21.4 (2012), p. 047804.

[43] Junxiong Guo et al. "WSe2/MoS2 van der Waals Heterostructures Decorated with Au Nanoparticles for Broadband Plasmonic Photodetectors". *ACS Applied Nano Materials* 5.1 (2021), pp. 587–596.

[44] Robert W Boyd. *Nonlinear Optics*. Academic press, 2020.

Chapter 6

Conclusions and Future plan

The thesis entitled "Third order nonlinear optical properties in WSe_2 thin films" is devoted to investigate the third order optical nonlinearity of WSe_2 thin films. It also presents a detailed analysis of the impact by various factors including laser parameters (wavelength, repetition rate, intensity) and material properties (thickness, defects, heterostructures) on the third order NLO properties in RF-sputtered WSe_2 thin films. In order to achieve this goal, the thesis is planned as follows:

As-prepared WSe_2 thin films

In this study, we have carried out wavelength dependent study of NLO properties of WSe_2 films. The NLO coefficients were estimated using Z-scan experimental configuration which used ultrashort pulses centered at different central wavelengths. We found that WSe_2 thin films exhibit saturable absorption behaviour at visible spectral band (515 nm excitation wavelength). This is essentially a consequence of strong Pauli-blocking effect and

manifests as negative value of the nonlinear absorption coefficient (β). At NIR ultrashort pulses (centered at 1030 nm), WSe_2 films exhibits a reverse saturable absorption (RSA) signature which is mainly the contribution from two photon absorption (TPA) (a positive β). In addition, the closed-aperture (CA) Z-scan measurements display a variation where a pre-focal maxima is followed by a post-focal minima which is the signature of the self-defocusing effect and a negative value of nonlinear refractive index (n_2). Furthermore, from an application viewpoint, we explored the impact of laser parameters *i.e.* repetition rate, laser intensity, pulse width etc. on the NLO response of WSe_2 thin films. The high repetition rate as well as high optical intensities could substantially modify the structural features of the materials and may yield a significant variation in NLO properties. Accordingly, we have carried out the measurements at different laser intensities and found that there is a significant contribution of the thermal diffusion effects at high repetition rate. At high laser intensities, the contribution of free-charge carriers to nonlinear absorption is very strong. The investigation suggests that the electronic contribution to the NLO properties maximizes at low pulse repetition rates, preferably at time-scales lesser than the thermal lifetime.

In another work, we have observed the impact of thickness on the NLO properties of WSe_2 thin films. It is well known that TMDs possess thickness dependent bandgap and one can alter the bandgap by varying thickness. This provides a route to tailor the NLO properties for suiting a certain application. In order to understand this point, we investigated the dependence of optical nonlinear response on WSe_2 film thickness. In this study, we have prepared a set of six film with variable thickness using RF sputtering deposition method. The strain and dislocation density calculated from XRD pattern increases with increased thickness, which pointed towards the enhancement of the defects and the stress induced during film formation process. The Raman spectrum for the WSe_2 thin-films

depit the three characteristic phonon modes. E_{2g}^1 mode, which is associated with the in-plane vibration of W and Se atoms, A_{1g} mode, which is related to out-of-plane vibration of Se atoms and the B_{2g}^1 mode, which is a consequence of vibration of W and Se atoms owing to the interlayer interactions. From the bandgap estimation, it is inferred that the thicker WSe_2 film show two bandgaps which is a consequence of the defects in WSe_2 thin films. This was further confirmed using DFT simulations. In order to observe the impact of the defect states/defect bands on the NLO properties of WSe_2 films, we performed the Z-scan measurements at both visible (515 nm) and NIR (1520 nm) regime. At the visible spectrum, for the CA Z-scan measurements, all the samples consist of a pre-focal minima followed by a post-focal maxima which is the signature of the self-focusing effect and corresponds to a positive value of n_2. For the OA Z-scan measurements, all the samples exhibit SA behaviour which is attributed to the Pauli-blocking effect. In order to investigate the impact of thickness, we plotted β as a function of thickness and we observed that the NLO response is stronger for thicker WSe_2 films. The thicker film is expected to have a higher carrier density owing to denser stacking of WSe_2 monolayers. This essentially leads to high occupation probability for the states near the band-edges at high laser intensity, thereby creating a situation where the Pauli-blocking effect is dominant. Moreover, the defect states provide a more favorable situation for charge carrier accumulation near the band edges, thereby fostering the possibility of a stronger impact of Pauli-blocking effect and improved SA characteristics.

In the NIR spectral region, around the communication band, we carried out OA Z-scan measurements on the four WSe_2 thin film samples. As per the expectation, all the films exhibit TPA characteristics. In order to investigate the impact of thickness, we plotted β as a function of thickness and we observed that β exhibits a non-uniform variation as a function of thickness. This is due to the intermediate energy states. In addition, we also

observed the impact of optical fluence on the nonlinearity. In order to do that, we perform the NLO measurements for all the thin films, at different laser intensities. It is observed that β value is decreasing with increase in intensity, which is due to the free charge carrier absorption. The consistency between the variation of direct measurement of β (using OA $Z-scan$ technique) and the electronic bandstructure provides a plausible route to design NLO based absorbers and photonic switches through bandgap engineering of TMDs such as WSe_2.

Annealed WSe_2 thin films

In this work, we observed the impact of annealing on the NLO response of WSe_2 thin films. The NLO properties in TMDs could be altered by making the changes in the bandgap. In this context, TMDs with controllable thickness exhibit desired nonlinear absorption characteristics. Furthermore, the structural and optical properties of thin films are strongly influenced by the post deposition processes, in particular thermal annealing. These properties are dependent on the microstructures and interfaces present in the films. By the process of thermal annealing, the bandgap could be tailored, in this way, one can control the hyperpolarizability. Thus, it is important to investigate the impact of thermal annealing on the NLO properties of WSe_2 thin films. In this context, we deposited a set of four WSe_2 films and annealed at fixed temperature of $600°C$ with variable duration from $15-60$ minutes. From FESEM images, it is observed that thermal dewetting takes place in the films and the agglomeration of the films proceed with increased duration. As a result of this, the film is completely agglomerated in hexagonal arrangement, which is further confirmed by Energy Dispersive X-ray spectroscopy (EDS). The strain and dislocation density estimated from XRD pattern exhibits a decreasing trend as function of increased annealing duration (for a given temperature). This indicates *healing* of the defects and relaxation of the stress intro-

duced during film formation process. The lattice spacing between the planes obtained from transmission electron microscopy (TEM) corroborates this observation. The as-prepared WSe_2 film possess all three phonon modes while A_{1g} mode vanishes after annealing the films. The indirect bandgap estimated from Tauc plot using absorption spectrum tends to reduce as a function of annealing duration. After characterizing the WSe_2 films, the NLO response of the films were measured using ultrashort pulses centered at 1030 nm excitation wavelength. All the films (annealed as well as as-prepared) exhibited two-photon absorption (TPA) behaviour which is attributed to positive β value. A valley-peak signature is attributed to positive value for n_2 as a consequence of self-focusing effect. The impact of annealing on the optical limiting response was discernible in the measurements. All the annealed films exhibit improved optical limiting features. Through this, we could assert that the thermal annealing could strengthen the NLO response as well as the optical limiting response of the WSe_2 film.

Au NPs induced WSe_2 thin films

In this interesting work, we investigated the impact of gold (Au) nanoparticles (NPs) on the NLO response of WSe_2 thin films. In order to achieve this, we deposited Au films which was followed by thermal annealing. Due to this, Au NPs were formed. In one case, we transferred the Au NPs on top of a annealed WSe_2 thin film. In the second case, we deposited/sputtered WSe_2 thin film on the Au NPs. We deposited Au NPs on top and bottom of WSe_2 thin films which resembled an architecture that represented a situation where Au NPs are covered with WSe_2 film. The Au nanoparticles are spherical in shape which is confirmed from FESEM images. The Raman spectrum confirmed the presence of all three phonon modes (discussed above) in both the heterostructure. From the literature, it is confirmed that the Au NPs enhance the electric field intensity inside WSe_2 films due to which

phonon mode intensity increases. In addition to that, we carried UV-visible spectroscopy to obtain the linear absorption spectrum. The spectrum contained signature of localized surface plasmon resonance (LSPR). The impact of LSPR has also been observed in NLO response of the films. The NLO measurements have been carried out using ultrashort pulses centered at 1030 nm excitation wavelength. It is worth noting that the pristine WSe_2 film exhibits a TPA signature at 1030 nm wavelength while the heterostructure geometries show a SA signature along with strong optical nonlinearity. The measurements reveal that the presence of Au NPs in WSe_2 host matrix significantly strengthens the NLO response owing to LSPR excitation.

Future plan

The following opportunities for future work may result from the research done for this thesis:

1. The strong signature of saturable absorption (SA) observed in Au NPs induced WSe_2 films opens up the possibility of obtaining transmission enhancement at high NIR/MIR laser intensities. The nanoparticles size dependent nonlinear optical study could be explored further for practical application viewpoint and optimally tailoring the transmission/absorption characteristics. In addition, investigations of the spectral dependence of changes in nonlinear refractive index in Au nanoparticle-WSe_2 heterostructures are essential to understand its dispersion properties for practical applications.

2. The alteration in bandgap of WSe_2 thin films due to different Au- concentration doped using ion implantation method could be explored. Further, the manifestations

on the NLO response could be explored.

3. The impact of charge density waves on sufficiently thin WSe_2 films in the $TiSe_2/WSe_2$ heterostructure and its impact on the NLO response needs detailed investigations and could be explored.